Physiological Engineering Approaches for Synthetic Bone Materials

Dina Abdulaziz

Submitted in accordance with the requirements for the degree of

Doctor of Philosophy

The University of Leeds

The School of Chemical and Process Engineering

Faculty of Engineering and Physical Sciences

April 2022

The candidate confirms that the work submitted is her own and that appropriate credit has been given where reference has been made to the work of others.

This copy has been supplied on the understanding that it is copyright material and that no quotation from the thesis may be published without proper acknowledgement.

Acknowledgements

I express my sincere thanks to my supervisors Prof. Animesh Jha and Prof. Peter Giannoudis. Many thanks to Dr Antonios Anastasiou and Dr Vasiliki Panagiotopoullou for their continuous encouragement and feedback. A special thanks to Dr El Mostafa Raif and Sandeep Kumar for their invaluable advice and support during the biological experiments. Without the help of technicians, the work done so far would not be possible, for which I thank the technical support team. I would like to acknowledge in particular Mr S. Micklethwaite, Dr A. Scott, Dr B. Douglas, Dr A. Britton, Dr Z. Aslam, Dr F. Esat and Mr M. Javed for their laboratory assistance. I also would like to thank my colleagues, Dr Emaan Alsubhe, Evangelos Daskalakis, and Dr Neelam Iqbal, for sharing their knowledge and experience.

Many thanks to the Royal Commission for the Exhibition of 1851, the University of Leeds, Glass Technology Services (GTS) and Glass Sellers for the financial support.

I am incredibly thankful to my parents, sisters, and brother for their prayers and encouragement. Words cannot express the love and support of my beloved husband, Zaher. Thank you for the continuous motivation and encouragement throughout all the struggles I faced in completing my research. Finally, big thanks to my beautiful daughter Lamar; thank you for being in my life to inspire me every day to grow and be better

Abstract

The repair of large bone fractures is one of the most critical clinical challenges in orthopaedics. Even though different types of materials and designs have been investigated, most of these trials presented various deficiencies after the translation in the clinic. None of the proposed designs and materials could accurately mimic the mechanical and biological behaviour of natural bone. The "ideal" bone scaffold for treating large fractures must have collective properties to support healthy bone growth and avoid malunion or non-union. This work aims to develop a porous composite scaffold that can imitate the natural bone tissue by taking favourable characteristics of different materials to create a synthetic bone replacement that is biocompatible, appropriate for load-bearing applications, stimulates bone growth and promotes vascularisation at the defect site.

Based on the design of experiments principles (DOE), porous titanium/10 mol% Fe^{3+} doped brushite (Ti/DCPD-Fe) scaffolds were designed and fabricated. A parametric investigation was conducted to identify the appropriate fabrication conditions that result in mechanical properties similar to those of natural bone. Correlations that predict the mechanical properties of the sintered Ti/DCPD-Fe scaffolds as a function of i) sintering temperature, ii) CaP ratio and iii) extent of porosity were presented. The synthesised scaffolds were characterised in terms of crystal structure, phase constitution, microstructure and mechanical properties. Results proved the presence of calcium titanate $CaTiO_3$ on the surface of the composite scaffolds (Ti/DCPD-Fe), while titanium dioxide TiO_2 existed on the surface of pure titanium scaffolds (Ti) with a ~ 3 – 8 % increase in the atomic percent of oxygen after sintering in the inert atmosphere. Findings showed that the synthesised scaffolds had open porosity ranging between 26 – 60% with a pore size was ~ 100 – 850 μm. Also, small pores < 50 μm were observed in the structure which resulted in better interconnectivity up to ~ 95% in the scaffold with 40% space holder and 10% DCPD-Fe mineral. Finite element analysis was also conducted to investigate the stress and strain behaviour of the synthesised scaffolds. Results displayed that scaffolds with higher porosity and mineral content exhibited lower stiffness values closer to that of natural bone and exhibited flexible biomechanical behaviour at the interface bone/scaffold. The stiffness of porous composite scaffolds ranged between 3.30 – 20.50 GPa and the compressive strength was ~ 130 - 165 MPa at sintering temperature ≥1000^{o}C. *In vitro* outcomes suggested that all the synthesised scaffolds were non-toxic and biocompatible. Furthermore, cells presented excellent adhesion and growth, and their morphology shows a healthy attachment with a well-spread shape, which is indicative of high cellular interaction with all scaffolds' surfaces. Together experimental and numerical results have demonstrated that the synthesised porous composite (Ti/DCPD-Fe) scaffolds are promising to successfully support bone regeneration.

Table of Contents

List of Figures

List of Tables

Abbreviations

BBD	Box Behnken's design
CAD	Computer-aided design
CaP	Calcium phosphate
DCPD	Brushite (dicalcium phosphate dehydrate)
DCPD-Fe	Fe doped brushite
DOE	Design of experiments
DSC	Differential scanning calorimetry
DTA	Differential thermal analysis
EDX	Energy-dispersive X-ray spectroscopy
GPa	Gigapascal
h	Hour
HAP	Hydroxyapatite
He	Helium
KCl	Potassium chloride
MPa	Megapascal
SEM	Scanning electron microscopy
STA	Simultaneous thermal analysis
TCP	Tricalcium phosphate
TGA	Thermogravimetric analysis
Ti	Titanium
XPS	X-ray photoelectron spectroscopy
XRD	X-ray powder diffraction
β-CPP	β-calcium pyrophosphate

μCT	Micro-computed tomography

Samples list

(0,0)	Pure titanium with no KCl and no CaP mineral
(0,5)	Scaffold with no KCl and contains 5vol% of CaP mineral
(0,10)	Scaffold with no KCl and contains 10vol% of CaP mineral
(20,0)	Scaffold with 20vol% KCl to create porosity, no mineral
(20,5)	Scaffold with 20vol% KCl to create porosity and 5vol% of CaP mineral
(20,10)	Scaffold with 20vol% KCl to create porosity and 10vol% of CaP mineral
(40,0)	Scaffold with 40vol% KCl to create porosity, no mineral
(40,5)	Scaffold with 40vol% KCl to create porosity and 5vol% of CaP mineral
(40,10)	Scaffold with 40vol% KCl to create porosity and 10vol% of CaP mineral

List of Publications

Conference Papers

[1]. Abdulaziz D., Iqbal N., Giannoudis P.V., Jha A., September 2021. "Physiologically Engineered Scaffolds for Restoring Large Bone Defects''. *31st Annual Conference of the European Society for Biomaterials (ESB)*, Portugal.

[2]. Abdulaziz D., Iqbal N., Anastasiou A. D., Panagiotopoulou V., Raif E. M., Giannoudis P.V., Jha A., October 2020. "Novel Multilayered Scaffolds for The Treatment of Long Bone Fractures''. *1st Virtual EFORT Congress.*

[3]. Abdulaziz D., Anastasiou A. D., Panagiotopoulou V., Giannoudis P.V., Jha A., May 2020. "Parametric Study for Optimising the Mechanical Properties of Porous Titanium/Calcium Phosphate Scaffolds''. *11th World Biomaterials Congress*, Glasgow, UK.

[4]. Abdulaziz D., Anastasiou A. D., Giannoudis P.V., Jha A., September 2019. "Biocomposite Materials for Bone Tissue Engineering Scaffolds''. *European Society for Biomaterials ESB*, Dresden, Germany.

Journal Papers

The following papers are going to be submitted between August and October 2022:

[1]. Abdulaziz D., Anastasiou A. D., Panagiotopoulou V., Giannoudis P.V., Jha A., 2022. "Parametric Study for Optimising the Mechanical Properties of Porous Titanium/Calcium Phosphate Scaffolds as a Bone Substitute: An experimental and computational study''. *Mechanical Behaviour of Biomedical Materials.* (In preparation).

[2]. Abdulaziz D., Kumar S., Panagiotopoulou V., Raif E. M., Giannoudis P.V., Jha A., 2022. "Physiologically Engineered Bone: Quantifying the Mechanical Properties and Investigating Cellular Response of Novel Porous Composite Scaffolds''. *Advanced Healthcare Materials.* (In preparation).

Patent Application

Jha A., Giannoudis P.V., Jones E. A., Anastasiou A. D., Iqbal N., **Abdulaziz D**., February 2022. "Bone Repair Kit''. (Published, application No. PCT/GB2022/050670).

Chapter 1
Introduction

1.1 Introduction

The incidences of bone trauma have increased dramatically during the last few decades [1]. For example, over 65,000 cases of hip fracture, which is one of the most severe and frequent injuries for the elderly, were presented to 177 hospitals around the UK in 2016. As a result, hip fractures cost around £1 billion per year to the UK government and social care, according to the National Hip Fracture Database (NHFD) [2-6]. Fragility fractures also affect over 300,000 patients in the UK due to osteoporosis, and they are estimated to cost around £4.4 billion each year [4]. Statistical analysis of Europe's ageing population suggests that osteoporosis in men and women will increase from 27.5 million in 2010 to 33.9 million in 2025 (23% rise) [7-9]. This exponential rise in bone defects due to trauma, disease or injury has led to high demand for more advanced treatments to repair damaged tissue and promote bone healing.

Although bone tissue has remarkable regeneration properties, the healing process can be affected by the patient's characteristics or post-surgical complications [10-12]. These issues can manifest as delayed healing (delayed union), compromised union (malunion) or non-union at all. In order to treat these complications, recurrent surgical interventions are required, increasing patient discomfort and increasing overall cost [13]. These challenges are more frequent in the case of critical-size defects that would not heal spontaneously with bone during the patient's lifetime and require further surgical intervention [14, 15]. When the bone defect exceeds the critical size (large-scale), as shown in Figure 1.1, additional support and more complex surgical approaches are required, such as adding fillers made of the patient's bone (autologous) to increase the chances of recovery [16, 17]. However, this treatment is not always successful, especially in the cases of osteoporotic patients where overall bone quality and quantity are compromised [18, 19]. An alternative to the autologous graft is utilising either an allograft using cadaver bone from bone tissue banks or a xenograft using animal bone [20-22].

But these two types of procedures may cause a higher risk of infection after the surgery being a foreign body at the recipient's site [20, 23]. Therefore, there is an urgent need for an alternative synthetic substitute to promote bone healing without risks.

Figure 1.1: Large femoral shaft fracture with gap ~ 7 cm, fracture due to motorcycle accident of 16-year-old female [24].

In recent years, extensive research has been conducted to design and develop optimised bone scaffolds using different materials and technologies. In general, surgeons and medical device manufacturers favoured pure titanium (Ti) and titanium alloys due to their biocompatibility and strength-to-weight ratio closer to bone properties compared to other metallic alloys [25]. Yet, titanium scaffolds are far from being wholly optimised for bone due to the inadequate stimulation of new bone growth. The mismatch in stiffness between Ti scaffold and host tissue can cause stress shielding; since the cortical bone has Young's modulus E = 4 – 20 GPa while titanium exhibits E = 100 – 110 GPa [20, 26-28]. Ceramic materials and bioglasses have also been used widely due to their excellent biocompatibility and high corrosion resistance [29, 30]. Calcium phosphates (CaPs) have excellent osteoconductive properties due to their similar mineral component and porosity to the bone, allowing them to form a robust interfacial bond

with the host tissue and achieve bioactive interactions with osteoblasts to stimulate bone growth. But, their low fracture toughness restricts using them alone in load-bearing applications [29, 31-33]. Several studies included the usage of CaPs or bioglasses as coatings on metal scaffolds. These trials had a positive effect on bone healing, but eventually, the mechanical properties of scaffolds could not mimic those of natural bone [34, 35]. At the same time, polymeric materials have poor mechanical properties that restrict their use in non-load-bearing grafts even when integrated with bioceramics to enhance their strength. In addition, synthetic polymers have poor osteoconductivity with the risk of inducing cytotoxicity and inflammation, limiting their widespread use as bone substitutes [36].

1.2 Motivation

The regeneration and recovery of bone tissue is not an easy task since bone is a complex living tissue with magnificent mechanical properties and significant metabolic activity. So far, different types of natural and synthetic materials have been investigated, and several structures and geometries have been designed. However, after the translation in the clinic, none of the proposed designs and materials could accurately mimic the mechanical and biological behaviour of natural bone. Most of these trials presented various deficiencies leaving clinicians without a "golden route", especially when used for treating large bone defects. In reality, individual groups of materials have been unable to thoroughly consider the structure and functionalities of natural bone tissue when used alone. The "ideal" scaffold must meet several criteria; i) mechanical properties comparable to that of bone to sustain the load of the body; ii) osteoconductive properties to promote bone formation; iii) an appropriate structure to allow the circulation of nutrients; iv) and the potential to trigger vascularisation at the defect site [26, 37-40].

The challenge of this work is to cope with the apparent limitations of current scaffolds and develop a composite material by taking favourable characteristics of different materials to create a synthetic scaffold that is biocompatible, appropriate for load-bearing applications, supporting osteogenesis and providing sufficient vascularisation [40, 41]. This work aims to fabricate and characterise porous titanium/calcium phosphate (Ti/CaP) material to be used in bone substitutes. As different fabrication conditions significantly influence the mechanical properties of the scaffold, this work considers the most critical synthesis variables i) sintering temperature, ii) CaP ratio, and iii) porosity. The design of experiments principle is followed to do a parametric investigation to define the space and combination of values that result in mechanical properties similar to those of natural bone. Finite element analysis is also performed to investigate the mechanical behaviour of bone with the synthesised scaffolds. This work focuses on the stress and strain analysis of femur bone because femoral diaphysis fractures are the most common injuries required to treat [42, 43]. Moreover, viability, adhesion to the surface, and proliferation of osteoblast cells are conducted in vitro to prove the synthesised scaffolds as an appropriate medium for cell survival.

1.3 Thesis Outline

The thesis is organised as follows:

- Chapter 1: commences with a brief introduction of the project, followed by the general aim of the PhD research work.

- Chapter 2: explains in detail, giving the reader the background knowledge to understand the concept of physiological engineering, starting with the fundamentals of bone structure, bone properties and the regeneration process of natural bone. Then, the chapter discusses the development and challenges of natural and synthetic materials

used in bone repair. Later, the vital requirements to design and fabricate the ideal bone scaffold to promote bone healing have been reviewed. Finally, the objectives of the PhD research have been outlined.

- Chapter 3: begins by laying out the materials used for the research and then describing the fabrication process of the scaffolds. The methodology to accomplish the aims of the research work is explained. This chapter involves characterisation techniques, testing tools, and protocols employed to achieve the project objectives.

- Chapter 4: starts with a detailed characterisation of the synthesised mineral (10 mol% Fe^{3+} dopped brushite). Then, compositional and structural analyses for the synthesised scaffolds are conducted to investigate the interaction between the metal and mineral phases. The scaffold's porosity is also explored, considering the distribution of pores, pore size and interconnectivity to assess the validity of the synthesised structures for implantation in bone scaffolding.

- Chapter 5: starts with the mechanical testing for the synthesised scaffolds. After that, the Minitab software performs the optimisation study of fabrication parameters to get the required mechanical properties. Finally, the stress distribution and strain analysis are performed for the scaffolds to validate the results.

- Chapter 6: supports the previous results by involving all the required in vitro experiments to investigate the potential of the synthesised scaffolds to be used in contact with living tissue later. Then, characterisation of the scaffolds after cell seedings is conducted to determine the changes in the structure and composition.

Chapters 2 to 6 include an introduction to present the basic concepts and a conclusion to summarise the chapter's content.

- Chapter 7: discusses the results of this research, where all findings related to the characterisation of scaffolds, biomechanical behaviour and biological response are linked and debated.

- Chapter 8: summarises and concludes the key findings of the work. The research's limitations and suggestions for future work are also presented in this chapter.

Chapter 2

Literature Review

&

Research Objectives

2.1 Introduction

The need for synthetic bone substitutes was first realised after WWII for helping victims when stainless steel and cobalt-based alloys became popular in the early days [25, 30]. Nowadays, titanium and titanium alloys have replaced stainless steel and cobalt alloys [44, 45]. However, Ti and its alloys do not succeed entirely as bone scaffolds due to the poor integration with host tissue [28, 46, 47]. Other materials such as polymers, bio-glass and calcium phosphate minerals have also been used in orthopaedic applications. But, their use has been limited due to their inappropriate mechanical properties [30, 36].

The concept of physiological engineering is a novel approach to address all these challenges and limitations. Chapter 2 explores how this concept's employment will lead to designing and fabricating physiologically acceptable bone tissue for patients' needs in an operating theatre. This chapter starts with the fundamentals of bone structure and bone regeneration process to get the required knowledge before designing and manufacturing a scaffold for bone tissue engineering. Then, the review discusses the development of current natural grafts and synthetic biomaterials for bone repair and highlights their challenges and drawbacks. Finally, all the requirements and properties that the scaffold must meet to successfully match the biological and mechanical properties of natural bone are reviewed.

2.2 Fundamentals of Bone Regeneration

The development of an ideal bone scaffold relies on the comprehensive understanding of the bone structure, bone properties, bone mechanics, and the mechanism of bone repair. All these concepts must be considered during the design and fabrication process to successfully achieve the physiological scaffold that could imitate the unique structure and enable full functionality [48].

2.2.1 Function and Structure of Bone

The skeletal system comprises between 206 and 213 bones in adults associated with cartilages and ligaments in the joints. Each kind of bone has a specific function, while the joints provide the rigid skeleton with several types of movements at different locations. The skeleton is the internal rigid framework of the human body. The bones in conjunction with the muscular system enable the body to move as it does. Bones are vital for protecting internal organs and keeping them safe from any injury or hard impact; for example, the brain is protected by the skull. Bones store approximately 85% of the phosphorus and 99% of the calcium in the body, which can be accessed when the body needs them. Also, fatty acids are stored in the yellow bone marrow to be called upon as energy reserves when needed. While crucial growth factors are stored in a mineralised bone matrix. Bone marrow is vibrant for producing red and white blood cells in the body. Furthermore, Bone has a crucial role in hearing by conducting vibrations through three tiny bones in the middle ear [42,49,50].

Bone tissue has several shapes and configurations adapted to the role of each bone; for instance, the femur bone is a hollow and thick-walled tube, whilst the scapula is a broad and flat plate [42]. Bone is a composite material containing approximately 60 - 70% inorganic mineral (can be approximated as tiny crystals of hydroxyapatite), and 8 – 25 % water by weight and most of the rest is an organic compound (around 90% are fibrous type I collagen and the remaining 10% are non-collagenous proteins) [49, 50]. The crystalline structure of bone contributes to the

stiffness and compressive strength, whilst collagen fibres provide bone with flexibility, tensile strength and toughness [50-54]. Figure 2.1 illustrates the structure of natural bone, which is composed of a hard outer layer (cortical bone) and a spongy inner compartment (cancellous bone) [28].

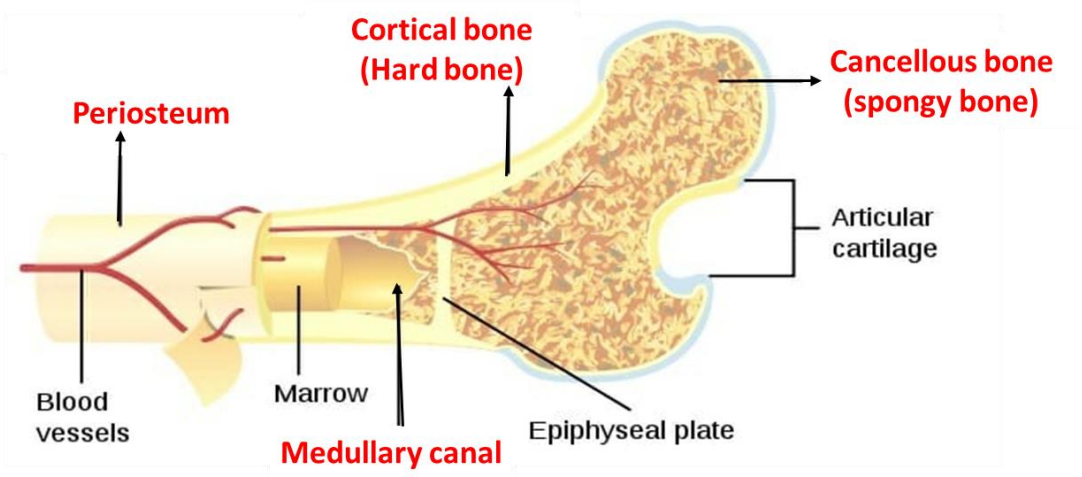

Figure 2.1: Internal structure of long bone showing the layers; the outer shell is the hard cortical bone covered by the periosteum, and the inner component is spongy tissue, adapted from [55].

Cortical (Compact) Bone

Cortical bone forms the hard external layer of bones; cortical bone tissue consists of cylindrical osteons aligned parallel to the long axis of the bone and surrounding the Haversian canal (osteonic canal), which contains the blood vessels and nerves [55, 56]. As can be observed in Figure 2.1, a dense fibrous membrane, known as the periosteum, covers the surface of cortical bone and contains blood vessels, nerves and lymphatic vessels, which nourish compact bone tissue. Cortical bone has a higher material density; therefore, it is the strongest part of the bone. It also stores calcium which it releases to the body when needed. Cortical structure and microstructure contribute to the whole bone mechanical competence since osteons are aligned in the same direction along the lines of stress-supporting bone to resist bending and fracture

[55-57]. Cortical thickness, cortical area and area moment of inertia are considered the strong predictors of bone strength and resistance to fracture [41, 51].

Trabeculae (Cancellous) Bone

Trabeculae bone forms the inner layer of bones; in the interior structure, bone tissue is arranged in a network of intersecting plates and spicules, termed trabeculae [56]. Trabeculae is highly porous, allowing nutrient diffusion and also vary in amount in different bones. Trabeculae enclose spaces filled with blood vessels and marrow; this honeycombed tissue is also called cancellous or spongy bone. In mature bone, trabeculae are arranged in an orderly pattern that provides continuous units of bony tissue aligned parallel with the significant compressive or tensile force. Thus, trabeculae provide a complex series of cross-braced interior struts that support maximal rigidity with minimal material [41, 55, 58].

Bone Cells Function

Bone cells have an essential role in bone remodelling by maintaining the balance between bone resorption and bone formation [28, 59]. Therefore, understanding the function of bone cells is quite crucial before designing the synthetic scaffold to control the scaffold-cells reaction.

Bone contains four types of cells responsible for the remodelling process: osteoblasts, osteocytes, osteoprogenitors and osteoclasts. As shown in Figure 2.3, these cells are responsible for the production, maintenance and remodelling of bone [28]. **Osteoblasts** are the cells found in the growing portions of bone (periosteum and endosteum) and are responsible for forming new bone, synthesising and secretion of the collagen matrix and calcium salts. When the team of osteoblasts has finished making new bone, some become surrounded with matrix and differentiate into osteocytes, whilst others will remain on the surface of the new bone and differentiate into lining cells. The rest undergo apoptosis (cell suicide) disintegrate [59, 60]. **Osteocytes** are the primary cells of mature bone; each osteocyte is located in a pocket called a lacunae surrounded by a bone matrix. The osteocytes' function is maintaining the

mineral concentration of the matrix via the secretion of enzymes. **Osteoprogenitors (Osteogenic cells)** are the only bone cells that divide since osteogenic cells differentiate and develop into osteoblasts. The fourth type of bone cell is called **Osteoclasts** which are responsible for the resorption and breakdown of bone; they form sealed compartments next to the bone surface and secrete acids and enzymes which degrade the bone [28, 61].

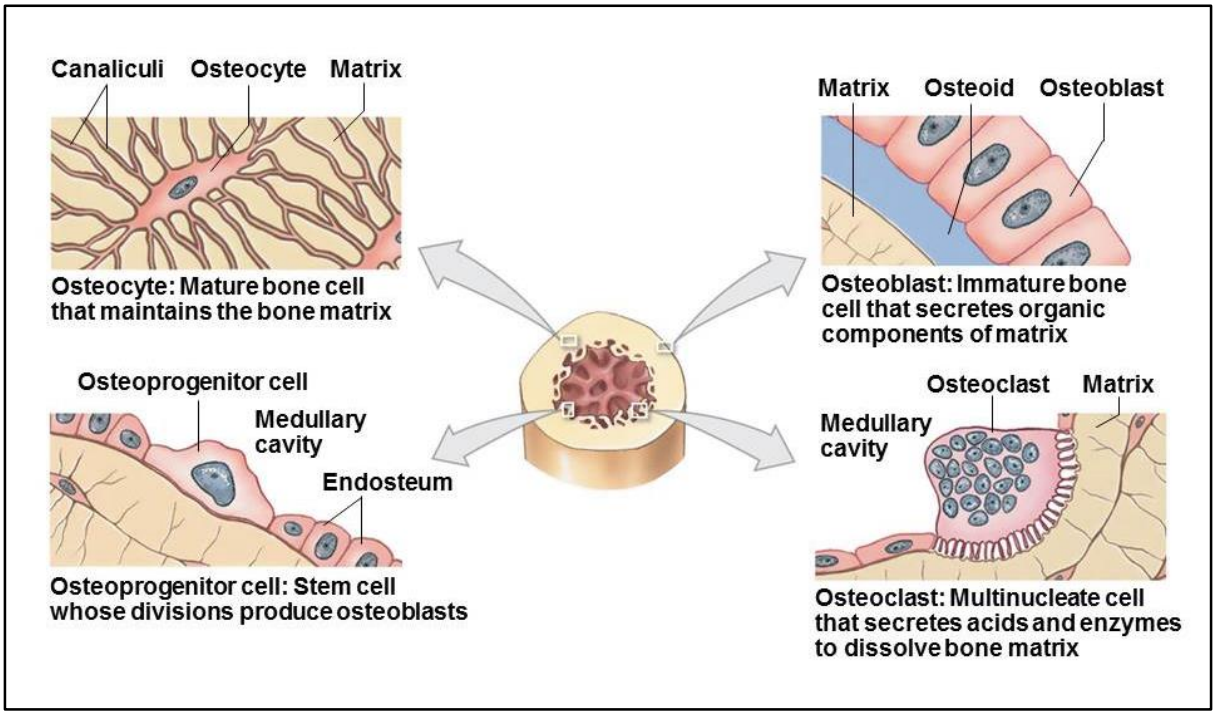

Figure 2.2: The types and functions of bone cells [62]

2.2.2 Bone Remodelling and Repair

Bone can renew itself throughout life and replace old tissue with a new matrix through bone remodelling. The bone remodelling process consists of two events; **resorption** by osteoclasts (mature bone is removed) and **formation** by osteoblasts (new bone is formed) [63, 64]. This dynamic process depends on the partnership between osteoclasts and osteoblast lineage cells to get the proper balance between resorption and formation of bone [59]. A fractured bone undergoes repair through four overlapping stages described below and shown in Figure 2.4 [65, 66].

Hematoma formation (stage 1): following fracture, disruption of blood vessels results in the formation of a hematoma, which encloses the injured area. The inflammatory process starts rapidly after trauma and lasts until the bone formation begins (1–7 days post-fracture). New bone is produced due to the transplantation of hematoma since granulation tissue forms at the ends of the bone. **Soft callus formation (stage 2):** angiogenesis occurs during this stage since new blood vessels form from pre-existing vessels. Granulation tissue is replaced gradually by hypotropic cartilage (internal callus), and the periosteum undergoes direct bone formation to create an external callus. **Hard callus formation (stage 3):** internal callus mineralises with calcium hydroxyapatite to form a hard callus of woven bone. **Bone remodelling (stage 4):** large fracture callus is replaced with secondary lamellar bone. The callus size is decreased to that of pre-existing bone at the defect location, and the vascular supply reverts to normal [65, 66].

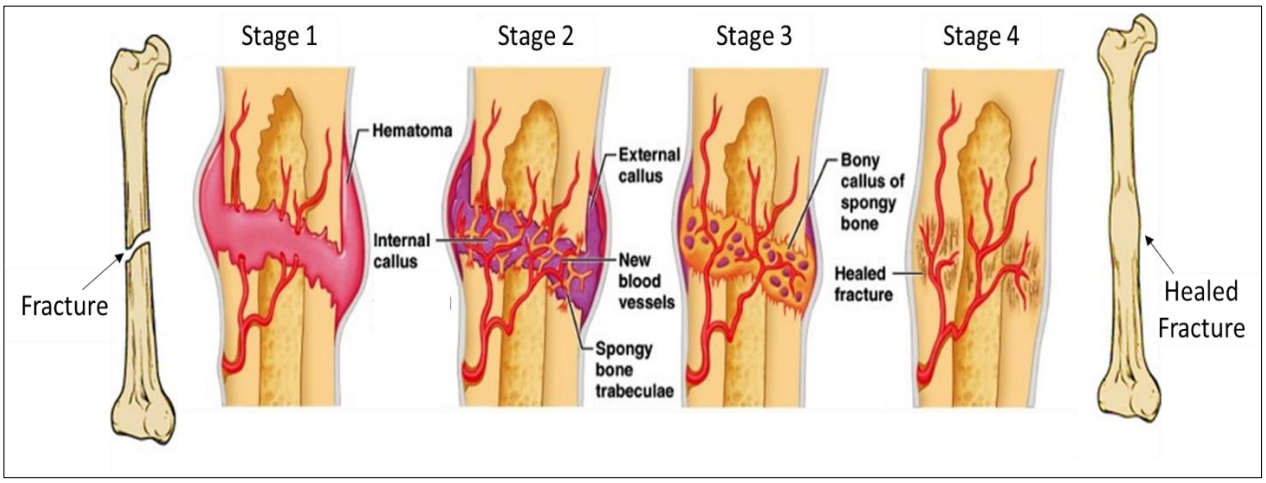

Figure 2.3: The four stages of bone repair: (stage 1): hematoma formation, (stage 2) soft callus formation, (stage 3) bony callus formation, and (stage 4) bone remodelling,.adapted from [65].

2.2.3 Bone Regeneration

Bone regeneration is a complex process in which most bone fractures can heal and regain full functionality without the formation of scars [67]. However, the regeneration of large segmental defects caused by trauma, osteoporosis, or cancer can be affected by the patient's

characteristics or post-surgical complications. Natural bone regeneration is compromised when more than a 5 cm defect exists, leading to delayed union or non-union because large quantities of bone tissue are required. The treatment of such cases is a clinical challenge; therefore, a comprehensive understanding of bone regeneration is essential for developing more advanced treatment methods [68-70]. The three critical elements in the regeneration process of bone are osteoinduction, osteoconduction and osseointegration [71]. **Osteoinduction** is the process by which new bone formation (**osteogenesis**) is induced since osteoinduction involves stimulating immature cells to develop into pre-osteoblasts. The scaffold/material itself can be osteoinductive after the insertion into injured bone [72-74]. **Osteoconduction** refers to the process by which bone is directed to grow on a scaffold's surface and conform to this surface. This surface is termed an osteoconductive element which permits bone growth on its surface or down into pores [72]. **Osseointegration** means the direct structural and functional bonding between the host bone tissue and the grafting material without any connective tissue [32, 72]. Several factors can affect the osseointegration process and determine the ability of the scaffold to integrate into the surrounding bone tissue successfully. These factors include biocompatibility, scaffold surface, loading conditions, angiogenesis, and cell adhesion [75].

2.2.4 Biomechanics of Bone

Understanding bone biomechanics will help design the ideal scaffold with mechanical properties consistent with natural tissue. Biomechanical stability is essential for the performance in vivo to support bone regeneration and avoid healing delay or non-union.

2.2.4.1 Mechanical Behaviour of Bone

During daily activities, the skeletal system is subjected to various loads in different directions (body weight, muscle forces, and external forces), producing five different types of forces: tension, shear, compression, torsion or curvature [76]. The mathematical analysis demonstrates

that each bone part has an excellent inner structure adaptation to the mechanical requirements. For example, loads on the femoral head lead to internal stresses where the inner structure is formed to supply an efficient manner for these stresses. The relation between these internal stresses and the inner structure of the femur agrees with the theoretical laws producing maximum strength with minimum material. In other words, the femur bone obeys the mechanical relations for maximum economy and efficiency [77, 78]. Figure 2.5 demonstrates the stress-strain curve of natural bone compared with ductile and fragile materials' curves. As can be observed, bone has fragile and ductile properties; thus, it is slightly deformed when a load is applied before failure. While a fragile material responds linearly and breaks without any deformation, ductile material gets into the plastic area and deforms before failure [76, 78].

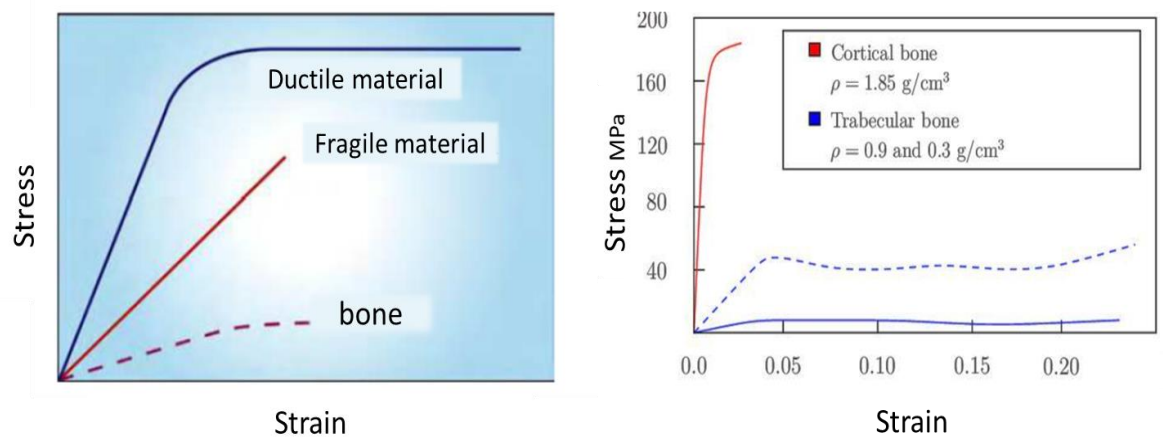

Figure 2.4: Stress-strain curves of human bone showing the general behaviour of bone and the changes of mechanical properties with the density; the stress-strain curve of bone comparing its general behaviour with ductile and fragile materials (left) and the compression stress-strain curve for the cortical and trabecular bone with different densities (right), adapted from [76, 79]

Mechanical properties of bone differ according to the anatomical location and the loading direction [41, 51]. There is wide variability in mechanical properties: Young's modulus, tensile strength and compressive strength between the longitudinal and transverse loadings, as shown

in Table 2.1; thus, bone is considered an anisotropic material. The mechanical characterisation of cancellous bone is even more complicated because the cancellous bone is extremely nonhomogeneous [41, 80]. Mechanical properties of bone are related to several variables dependent on each other such as age, gender, mineral and liquid content. For example, the strength of cancellous bone depends on bone mineral density; thus, a 25% decrease in bone mineral density (bone loss because of age) can lead to a 44% reduction in the strength of cancellous bone. However, other properties of trabecular bone, such as the ultimate strain and yield strain are almost independent of bone density [81].

Table 2.1: Structural and mechanical properties of cortical bone, adapted from [41].

Loading	**Porosity [%]**	**Density [g/cm^3]**	**Young's modulus [GPa]**	**Tensile strength [MPa]**	**Compressive strength [MPa]**
Longitudinal	5-10	1.99	17-20	79-151	131-224
Transverse	5-10	1.99	6-13	51-56	106-133

2.2.4.2 Bone Fractures and Disorders

The right balance between bone resorption and bone formation maintains the healthy condition of the bone. Any alterations or changes in this mechanism lead to several skeletal diseases, like osteoporosis, due to the massive resorption of bone. Osteoporosis weakens bone and makes it fragile due to low bone mass, making bone at greater risk for injuries and fractures, as explained in Figure 2.6 [74].

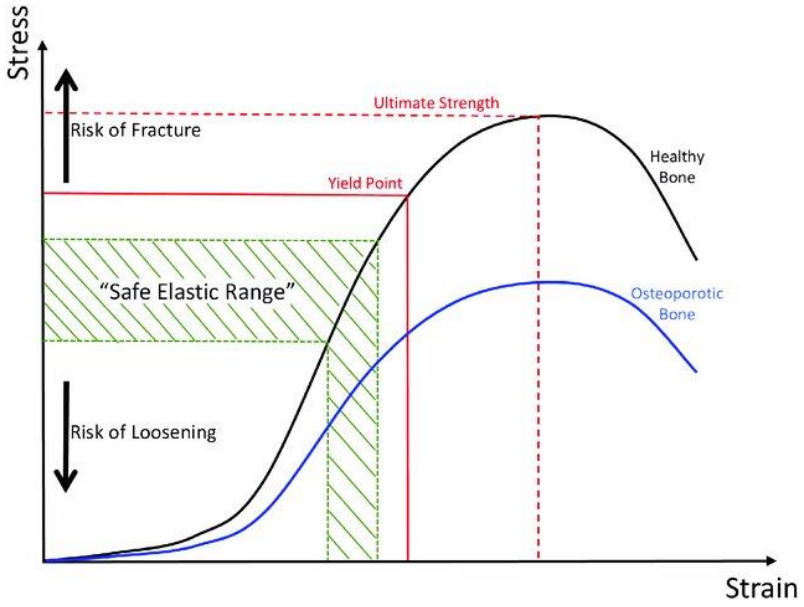

Figure 2.5: Comparison of stress-strain curves of healthy bone and osteoporotic bone; healthy bone presented (in black) and osteoporotic bone (in blue) and the "safe elastic range" area is shown in green to identify bone deformation with any potential risks of failure or loosening [82].

Bone is weaker in tension and fails mainly due to tensile forces. Even bone is more robust in compression, but compressive forces might cause fracture by shearing. The combination of compressive and bending stresses on bone results in the butterfly fracture, as shown in Figure 2.7 [80].

Fractures of the femur bone are among the most common bone injuries, especially in females and older people. The mechanism of femur fractures can be classified into high energy trauma and low energy trauma. Usually, femur fractures in young people occur because of high energy collisions such as car crashes, motorcycle crashes or falls from heights. In contrast, most femoral fractures by a lower force trauma occur in older people. On the other hand, femoral fractures may occur due to pathologic fracture, osteoporosis, or metabolic bone disease. Injuries may occur in any part of the femur bone; however, femoral shaft fractures are the most common femoral injuries; therefore, this research will focus on this kind of fracture [83, 84], as we will see in chapter 5.

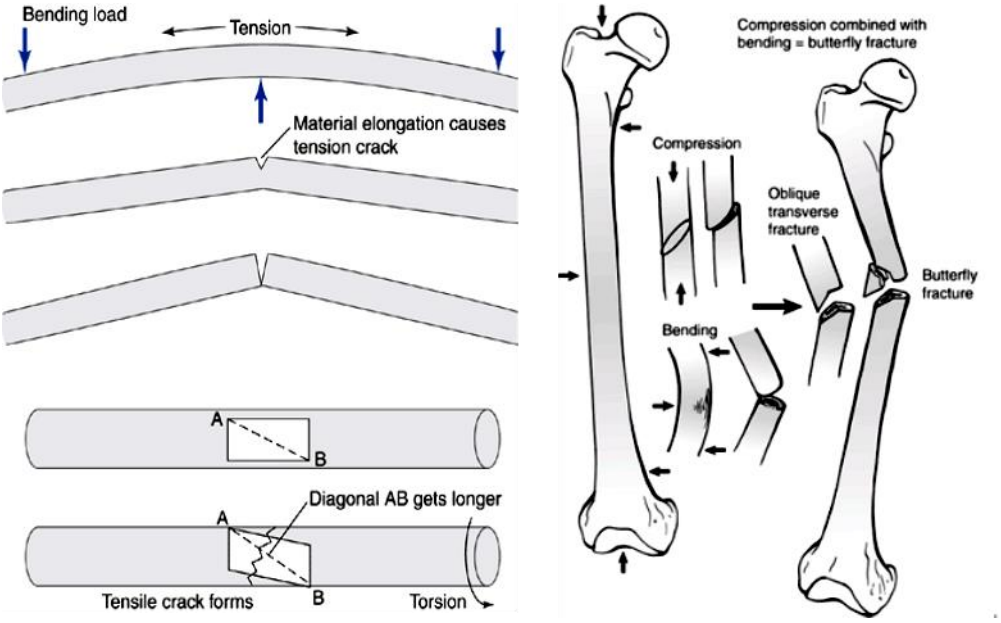

Figure 2.6: Different types of long bone fractures caused by different types of loads (tension, compression and bending), adapted from [80]

As we discussed before, not all bone fractures will heal normally; for example, about 13% of tibia fractures are associated with delayed union or non-union due to impaired bone regeneration. Bone healing rates vary with the patient's characteristics, especially the age since the repair process is slower in the elderly [84-86]. Therefore, there is a tremendous need to develop systemic therapies and novel treatments to promote bone healing and accelerate regeneration.

2.2.4.3 Biomechanical Analysis

Biomechanical analysis is essential to understand the behaviour of natural bone during the healing process. Several studies have used finite element analysis to describe bones' stress distribution and deformation and the mechanical behaviour of joints and scaffolds [43]. This study will focus on the stress analysis of femur bone because femoral diaphysis fractures are the most common injuries required to treat [42]. Surgeons use orthopaedic implantation to

replace the damaged bone in most femoral shaft fractures. Different biomaterials were investigated for fabricating femur scaffolds; Deshmukh studied the properties and biocompatibility of stainless steel, cobalt chromium, titanium alloys, and polymers. The results showed that low stiffness material is better for long bone fractures [87]. Das also examined the biomechanical feasibility of different biomaterials. The study included a simple bone plate fixed with screws across a fracture line on the femur since torsional and compressive loadings were applied along with several stages. The results found that titanium generates relatively higher stresses in the damaged area than stainless steel and cobalt chrome. These higher stresses at the callus zone provide better bone healing potential and better stability to the fracture fixation [88]. Another study compared bone plates made of other materials, including stainless steel, alumina, titanium, PMMA and Nylon [89]. A simulation of the full articulation using three-dimensional solid models involving the friction among the bodies was also done [90]. Kumar studied the stress analysis of the femur to investigate the behaviour of hip contact stresses/forces during daily activities like standing, walking, running and jumping [43]. Moreover, the influences of human weight during walking were studied by Amornsamankul; the results of this work showed that higher weight leads to a higher value of displacement [91]. Several numerical studies also were run to determine the suitability of open-porous scaffolds for healing femur fractures. Wieding et al. [92] used different titanium scaffold designs with a porosity between 64 and 80%. The defect was a large segmental distal femoral (30 mm) that stabilised with a plate and physiological hip reaction forces, as well as additional muscle forces, were implemented to the femoral bone. Uniaxial compression testing revealed young modulus of the scaffolds varied between 3.5 GPa and 19.1 GPa depending on porosity [92]. Later, Karuppudaiyan and colleages [93] designed several scaffolds with open porous structures (5% to 60% porosity) and used unit block for segmental defect of femur bone diaphysis. The maximum stress and displacement of the scaffold were studied with hydroxyapatite. The results

confirmed that the designed unit block could avoid the stress shielding effect between the scaffold and living tissue [93].

2.3 Conventional Bone Grafts

Conventional approaches are widely used to replace, restore, or promote the repair of damaged bone tissue [48]. Traditional grafts practised to treat bone defects can be divided into the following types: autografts, allografts, xenografts, and any combination thereof [19]. This review discusses the difference between the three clinical approaches and highlights the limitations and challenges of each one.

2.3.1 Autografts

Autologous bone is the harvested bone tissue from a donor site of the patient's body and then transplanted to another location of the same body [17, 71, 94, 95].

Advantages: surgeons consider autograft the golden standard of bone space-filling to a load-bearing replacement [23]. Autograft provides all the required properties of functional graft material as it is histocompatible and does not trigger an immune response. It has the essential components to promote osteoconduction, osteoinduction, and osteogenesis [17, 48, 71, 94, 95].

Disadvantages: since this approach includes harvesting bone tissue from the patient's iliac crest, a second surgery is required. Harvesting bone increases the surgical time and procedures and is usually accompanied by residual pain at the donor site and cosmetic defects. In some cases, significant complications may happen, including vascular or nerve injuries, deep infections at the donor site, neurologic injuries, or severe hematoma formation [18, 71, 96]. Furthermore, the total amount of autologous bone that can be transferred is limited, which restricts their use to treat segmental bone defects [19].

2.3.2 Allografts

Allogeneic bone grafts are tissues transferred between two unmatched genetically subjects. Allografts can be obtained from a living donor or cadaver and can be used in three ways: fresh, frozen or freeze-dried and from cortical or cancellous [21, 71]. Allografts are easily accessible through regional tissue banks and can be sent overseas because of tissue processing and sterilisation technology, which eliminates any possibility of disease transmission [19, 71]. Fresh allografts have strong osteoinductive capabilities, even though they are rarely used because of the high risk of disease transmission. Frozen and freeze-dried allografts are more osteoconductive than fresh allografts but have weaker osteoinductive properties [19, 71].

Advantages: allograft is considered the second option for surgeons to avoid the challenges associated with harvesting autologous bone, like morbidity at the donor site [23]. Allografts are available in adequate quantity, especially allogeneic bone harvested from a cadaver that can be customised in various sizes and shapes [21, 23].

Disadvantages: although the processing of allografts lowers the risk of transmission of viral diseases compared with blood products, it is still possible, especially human immunodeficiency virus (HIV) and hepatitis C virus (HCV) [23, 71]. On the other hand, the processing of allografts negatively affects the biological and mechanical properties resulting in less vascularisation and slower new bone formation [94, 95].

2.3.3 Xenografts

A xenograft is a tissue harvested from species other than humans, such as bovine bone, to promote bone reconstruction. The shortage of human grafts led to finding alternatives like xenografts to be practised after sterilisation and processing. Several xenografts have been developed to be used alone or combined with growth factors and or allografts to simulate the bone [19, 22]. During the xenograft treatment, the organic components are completely removed

to reduce the chance of rejection and avoid any transmission of diseases. But this process results in weak osteogenic capability, which restricts the wide use of xenografts in clinical practice. However, the remaining inorganic contents provide a good calcium source for bone formation [22].

2.4 Clinical Need for Bone Tissue Engineering

The rising rates of bone defects due to trauma, injury or disease have urgently required more effective treatment approaches, especially with the progressive ageing of the population where the higher potential of osteoporosis and poor physical activity exist [48, 97]. Although conventional procedures have saved lives and provided good results for bone healing, many drawbacks and challenges need to be overcome. As mentioned above, several studies have reported the challenges and complications of conventional treatments, including autografts, allografts and xenografts, especially in critical size bone defects [18, 19, 23, 48, 54, 71, 94, 95, 98]. This urgent need to create alternative therapy to conventional grafts has resulted in the development of the tissue engineering approach [48]. In 1988, Skalak and Fox defined tissue engineering to be ‘‘the application of principles and methods of engineering and life sciences towards the fundamental understanding of structure-function relationships in normal and pathological mammalian tissues and the development of biological substitutes to restore, maintain or improve tissue function’’ [9, 99]. Bone tissue engineering is a promising and fast-developing approach in bone regenerative medicine that aims to generate functional bone tissue with limitless supply and no disease transmission [48, 97]. Bone Tissue engineering is a multidisciplinary strategy combining the principles of orthopaedic surgery with the knowledge from biomaterials, cell engineering, design, growth factors, etc., to develop scaffolds to restore damaged bone tissue and recover its functions [9, 97].

2.5 Requirements of Scaffolds in Bone Tissue Engineering

Although minor bone defects with small gaps can be treated with conventional approaches, critical-size defects of more than 5 cm require more effective clinical intervention measures to heal successfully without the risk of delayed healing or non-union [100]. Over a decade ago, the 'diamond concept' proved itself to be an essential framework for understanding the vital requirements in the bone healing process [101]. Figure 2.8 illustrates the interactions between the critical parameters to generate the pathway for facilitating fracture repair. The diamond concept represents the crucial constituents of bone healing as the following: **1)** osteoinductive mediators, **2)** osteogenic cells, **3)** an osteoconductive matrix (scaffold), **4)** mechanical stability, **5)** adequate vascularity, and **6)** the host factors [11, 12, 101].

The 'diamond concept' is a conceptual framework that can be followed during the design of the advanced treatment for a successful bone repair. Unlike natural substitutes, synthetic substitutes can be almost completely controlled over the structure and properties [102]. The "ideal" scaffold must have the following five properties collectively to avoid missed union or non-union in a damaged bone: **1)** biocompatible components do not trigger an immune response; **2)** osteoconductive properties to promote bone formation; **3)** an appropriate structure for supporting the circulation of blood and nutrients; **4)** the potential to trigger vascularisation at the defect site; **5)** biomechanical compatibility comparable to that of bone to withstand the load of the body and **6)** controllable degradation rate matching the tissue growth rate [26, 37-40, 48, 98, 103].

The materials development and the requirements that should be available in the synthetic bone scaffolds are discussed in more detail below**.**

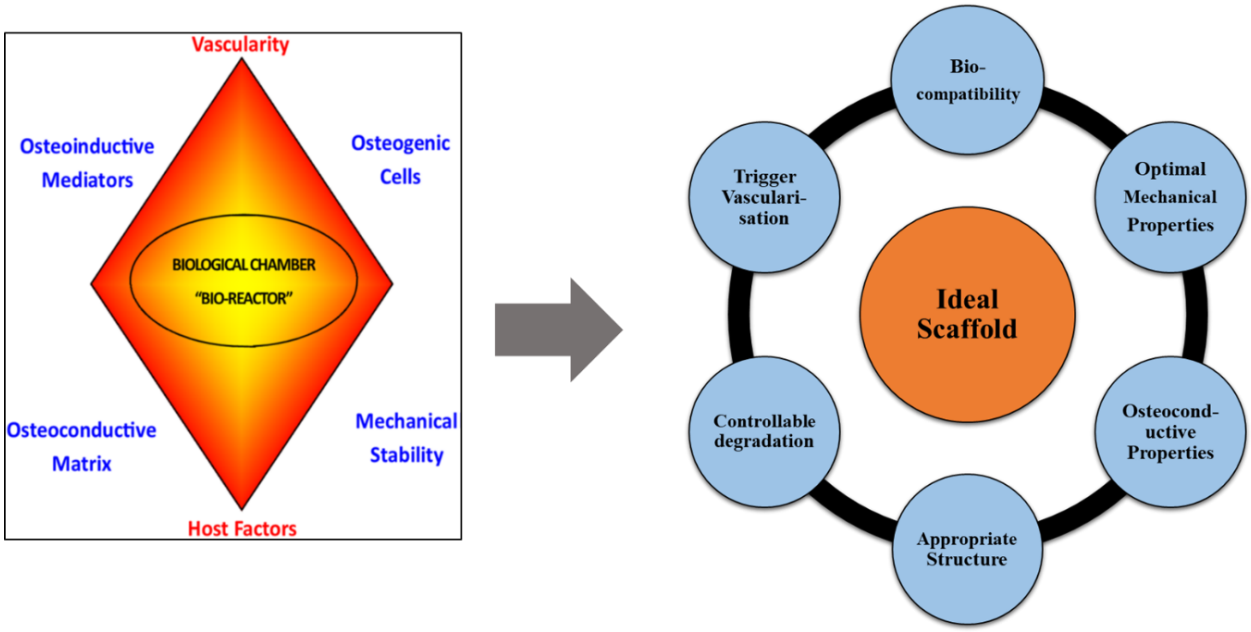

Figure 2.7: Illustration of the requirements of an 'ideal bone scaffold' based on the 'diamond concept' of bone healing, adapted from [101].

2.5.1 Biocompatibility

The synthetic scaffold will directly contact the cells and living tissue; therefore, it should be biocompatible with the host environment with no harmful effects on the patient's body. Biocompatibility is the first requirement that must be considered during the design and manufacturing of any bone scaffold. Biocompatibility of the scaffold refers to its ability to support cellular activity without any toxic effects on the host tissue [36, 104]. Thus, the materials used to fabricate the scaffold must be non-toxic, non-allergenic, and not trigger an immune response [25, 103]. Biomaterials used to manufacture bone scaffolds can be divided into metallic, ceramic, polymeric, and composite materials [105]. This review has focused on the historical development of biomaterials in the field of bone tissue engineering. Also, challenges and drawbacks have been highlighted to be considered during the design and fabrication of the ideal scaffold that aims to possess similar properties to natural tissue.

2.5.1.1 Metallic Biomaterials

For several years, metals and their alloys have been used in orthopaedic and dental applications. In general, metallic alloys are used more than pure metals in the manufacturing of implants due to their superior properties. These alloys can be categorized into four groups based on the major alloying element: stainless steels (such as 316 L), cobalt alloys, titanium alloys (such as Ti-6Al-4V) and other alloys like NiTi, Mg, and Zr alloys [25, 106, 107].

2.5.1.1.1 Stainless Steels

Stainless steels have been used widely for implants manufacturing due to their low cost and accepted biocompatibility [25, 30, 108]. Stainless steel can be categorised into four groups: martensitic, ferritic, duplex and austenitic alloys, based on the characteristic microstructure [44]. Austenitic alloys are the most popular in medical applications; for example, 316L alloy is used as short-term implants [44]. 316L Stainless steels cannot be used as long-term implant devices because of their poor resistance to corrosion in the body. The poor wear resistance may lead to inflammatory reactions in the surrounding tissues. The time of failure varies from several months to several years after implantation. Most of the failure analysis has indicated that the fracture occurs due to fatigue failure, which gets worse in poor surface finishing implants [109]. In addition to these limitations, the toxicity of released nickel and chromium restricts the use of stainless steel alloys and is replaced by other efficient materials [25, 30].

2.5.1.1.2 Cobalt-based Alloys

Cobalt-chromium-molybdenum (CoCrMo) alloys were broadly used in load-bearing sites such as hip and knee implants [44]. CoCrMo alloys experienced over 20-year service longevity in the joint bearing systems due to their excellent corrosion resistance and better wear resistance than stainless [110]. However, these alloys suffer from poor biocompatibility due to the release of Co, Cr, and Ni in the surrounding. Its little resistance to corrosion fatigue and fretting fatigue

can also lead to the implant's failure [25]. As shown in Table 2. 1, CoCrMo alloy has high stiffness, making it more likely to produce more significant stress shielding [111, 112].

2.5.1.1.3 Titanium and titanium-based alloys

Titanium and its alloys have been intensively used in orthopaedic applications for many decades due to their biocompatibility and chemical stability [25]. Hip, knee and elbow replacements are the most common applications of titanium alloys. Depending on the microstructure after processing, titanium alloys are categorised into four groups: α alloys, near-α alloys, α – β alloys, and β alloys [25]. The first generation of titanium alloys (Ti–6Al–4V alloys) has been reported to cause allergic reactions with the surrounding tissue, whilst the second generation of titanium alloys (β -titanium alloys) has been developed and improved to address this problem [113]. Titanium exhibits high specific strength and lower Young's modulus comparable with the other biocompatible metals (Table 2.2) [25, 46, 47]. Titanium is non-ferromagnetic, so patients with titanium implants can be safely examined with magnetic resonance imaging (MRI) and computed tomography scanning (CTS), which are required to assess the position and health of the scaffold and the host bone tissue [47]. However, there are many concerns regarding the long-term performance of titanium scaffolds. The inert biological behaviour of titanium is a suitable property, but that badly affects its integration with the host bone tissue [47]. Osseointegration between the artificial scaffold and the natural bone tissue is critical for successful osteogenesis [113, 114]. Surface modifications techniques such as anodic oxidation have been suggested to overcome these drawbacks and enhance titanium bioactivity [115, 116]. The surface with moderately rough topography and high surface energy influences cellular activities to promote bone formation [114, 117]. Also, highly porous Ti scaffolds have been recently produced to improve the fixation and vascularisation at the defect site to improve bone healing [35]. However, none of these trials has presented the ideal scaffold that matches the mechanical and biological properties of natural bone. In reality, Titanium scaffolds are far

from being wholly optimised for bone regeneration due to lack of osseointegration and the mismatch in mechanical properties between the scaffold and host tissue, which can cause stress shielding resulting in a decrease in density of the bone [20, 26, 47, 98, 118-120].

Table 2.2: Mechanical properties of bio-metallic alloys compared to the cortical bone, adapted from [25, 47].

Materials	Young's modulus [Gpa]	Tensile strength [Mpa]	Yield strength [Mpa]	Compresive strength [Mpa]	Fracture toughness [Mpa.m$^{0.5}$]
Cortical bone	10 - 30	50 - 170	30-70	131-219	2 – 12
Ti alloys	110 - 125	700-930	485	590-1117	55-115
Stainless steels	189-205	540 - 1350	220-1200	170-310	50-200
CoCrMo alloys	240	900 - 1840	448-1606	-	100

2.5.1.2 Bio-Ceramics

2.5.1.2.1 Calcium phosphates

Calcium phosphate materials have been widely used as bone substitutes due to their osteoinductive and osteoconductive features [29, 30, 121]. Osteoinductive and osteoconductive characteristics of Calcium phosphates (CaPs) enhance cell adhesion, proliferation, and promote bone regeneration [121]. Calcium phosphate materials have similar crystallinity to the mineral components of bone. The most common types of calcium phosphates investigated for bone tissue engineering and their properties are shown in Table 2.3 [41]. Bioactive behaviour differs between these types due to their crystal structure, Ca/P ratio, porosity, and solubility [41, 121, 122]. The solubility and well-timed degradation rate of scaffolds play a vital role in bone regeneration [123]. Solubility of CaPs phases varies with different factors: porosity, grain size, crystallinity, and sintering temperature [23, 103, 122, 124]. Table 2.3 shows that the lower the Ca/P ratio is, the more soluble the CaP phase is [125, 126]. TCP has greater solubility than HA

and rapidly resorbs due to its high porosity. HA resorbs at a slower rate which does not match the rate of bone regeneration; therefore, composite modification by mixing HA with calcium carbonate and BCP has been investigated to increase the resorption [127].

Table 2.3: Calcium phosphate materials used in bone tissue engineering applications, adapted from [126].

Name	Formula	Ca/P Molar Ratio	Density	PH Stability Range	Solubility at 37°C, _ log (Ks)
DCPA (dicalcium phosphate anhydrous, Monetite)	$CaHPO_4$	1.0	2.929	2.0 – 5.5 (>80°C)	7.02
DCPD (dibasic calcium phosphate dehydrate, Brushite)	$CaHPO_4.2H_2O$	1.0	2.319	2.0 – 6.0	6.63
α-TCP (α-tricalcium phosphate)	α-$Ca_3(PO_4)_2$	1.5	2.814	Precipitated from aqueous solutions only at T > 1125 °C	25.5
β-TCP (β-ticalcium phosphate)	β-$Ca_3(PO_4)_2$	1.5	3.067	Precipitated from aqueous solutions only at T > 800 °C	29.5
HAp, or OHAp (Hydroxyapatite)	$Ca_{10}(PO_4)_6(OH)_2$	1.67	3.155	9.5 – 12.0	117.2
TTCP, or TetCP (tetracalcium phosphate,	$Ca_4(PO_4)_2O$	2.0	3.056	Precipitated from aqueous solutions only at T > 1300 °C	37– 42

Figure 2.9 displays how certain phases of calcium phosphates are biodegradable to be resorbed in the human body and replaced by living bone tissue. These biodegradable phases are β-tricalcium phosphate, tetra-calcium phosphate, and CaO. When the material's surface is connected to water at a specific temperature, the bioactive phase (hydroxyapatite), which has

a unique molecular, micro and macrostructure to the bone, is formed. Then cells attach to the surface and start growing to promote the formation of a new bone [33].

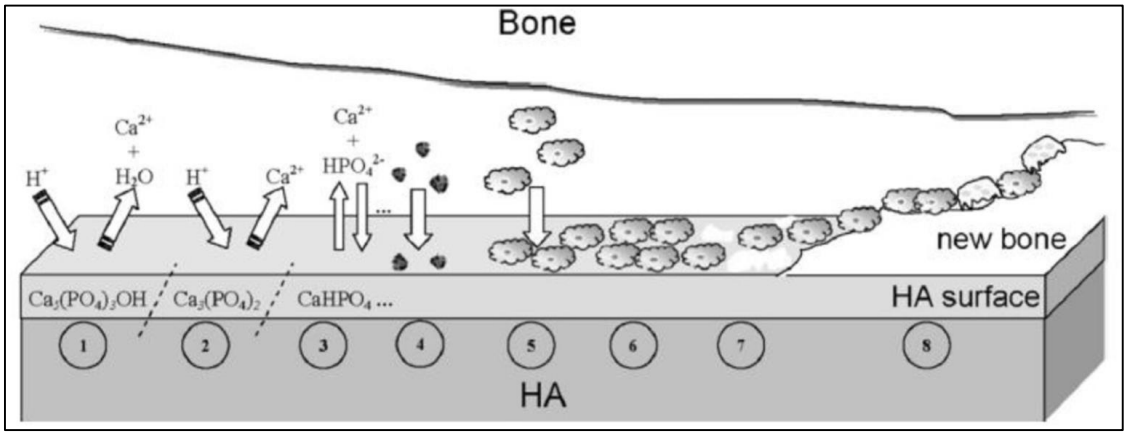

Figure 2.8: The mechanism of the bonding between bioactive material and bone showing the formation of new bone layer on HA surface; solubility of HA in physiological fluid (1 & 2), equilibrium between the HA phase and physiological fluid (3), adsorption of proteins and other bioorganic compounds (4), cell adhesion and growth (5, 6) and formation of new bone (7, 8). [30].

Recently, Beta- calcium pyrophosphate (β-CPP) has emerged as a promising material for bone tissue engineering [128]. β-CPP can be easily prepared by sintering brushite mineral, which has a fast setting reaction and good stability at room temperature [129]. Pyrophosphate is an ideal material for bone mineralisation and healing since it might work as a substrate of mineralisation enzyme [130-133]. Grove, in his study, compared the biological performance of a mixture of amorphous CPP/brushite with control brushite. It has been observed that more bone formation ~ 33% occurred in the sample containing CPP. While for the brushite control sample, only 14% of the area was replaced with new bone [131]. Naga and colleagues coated a porous alumina scaffold with brushite and then sintered it at 1100ºC - 1200ºC to be

transformed into β-CPP. Results showed that the transformed β-CPP after the sintering process promoted new bone formation around the scaffold [132].

Although CaPs materials support new bone formation and biomineralisation [103], their mechanical properties limit wider clinical applications of CaPs since they are brittle and have low fracture toughness (Table 2.4) because of the porosity that results in initiation sites for crack propagation [29, 134, 135]. Therefore, CaPs are used in non-load bearing applications such as filling of bone defects or as a coating for metallic scaffolds [126].

Table 2.4: Fracture toughness of calcium phosphate materials in comparison with cortical bone and titanium alloys, adapted from [136-139].

Material	Fracture toughness
HA	0.5 – 1 MPa $m^{1/2}$
β-TCP	0.92 MPa $m^{1/2}$
Brushite	0.1 MPa $m^{1/2}$
Cortical bone	2 – 12 MPa $m^{1/2}$
Titanium alloys	28 – 108 MPa $m^{1/2}$

2.5.1.2.2 Bioactive glasses

Bioactive glasses have been used in a particulate form for bone regeneration due to their ability to stimulate osteogenesis. Bioactive glasses consist of mixtures of oxides from SiO_2, CaO, Na_2O, K_2O, MgO, P_2O_5, and many compositions have been developed to adjust their properties for specific applications [31, 140]. Bioglasses are proper materials for bone scaffolds because of their excellent osteoconductivity and controllable degradation rate [41, 141]. The first

known bioactive glass is 45S5: 45wt.% silica (SiO_2), 24.5wt.% calcium oxide (CaO), 24.5wt.% sodium oxide (Na_2O), and 6wt.% phosphorous pentoxide (P_2O_5) [140, 142]. After implantation, such silicate-based bioactive glass has an additional advantage due to the released Si ions that enhance primary osteoblasts' growth and osteogenic differentiation [140]. 6P57 bioglass also has a promising composition: 56.5wt.% silica (SiO_2), 15wt.% calcium oxide (CaO), 11wt.% sodium oxide (Na_2O), 6wt.% phosphorous pentoxide (P_2O_5), 3wt.% Potassium oxide (K_2O), and 8.5wt.% Magnesium oxide (MgO) [143]. Popescu's study proved that primary osteoblasts grown on 6P57 bioglass surfaces displayed better viability and proliferation than other bioglasses higher in silica [144]. Proper contacts between large surfaces of the cells and the 6P57 films have proven that the structures forming in SBF represent suitable substrates for osteoblasts survival [145]. The strong bond between bioactive glasses and living tissue forms a biologically active layer of HCA that can develop only if the glass surface can create Si-OH bonds when immersed in a biological environment [140]. However, bioglass compositions based on borate and borosilicate have better controllable degradation rates than silicate bioglass [146]. Their degradation rates are closer to the bone formation rate, making them ideal for bone scaffolds [146]. The composition of bioglass affects the interfacial reactions and hence the bioactivity. For example, released calcium ions and silicon enhance bone osteogenesis. During the manufacturing process, bioactive glasses can be doped with elements such as Cu, Zn or Sr to enhance antibacterial properties and regenerative processes [104, 147]. However, the inherent brittleness and low fracture toughnes ($0.7 – 1.1$ MPa $m^{1/2}$ for 45S5 bioglass) limited the use of bioglasses as bulk material to non-loadbearing substitutes [30].

2.5.1.3 Polymers

2.5.1.3.1 Natural Polymers

Natural polymers have been suggested for bone reconstruction due to their biocompatibility and bioresorbable properties [26, 148]. Natural polymers such as collagen, fibrin, glycosaminoglycan and silk have good biocompatibility and biodegradability. Since bone contains collagen, natural polymers are ideal to substitute the collagenous structure of bone. Besides biocompatibility, natural polymers enhance cells adhesion and cell proliferation [149]. However, their low mechanical strength and lack of quantity limit their applications [104].

2.5.1.3.2 Synthetic Polymers

Synthetic polymers can be easily custom-made to fit the anatomical defects of individual patients. However, their lack of osteoconductivity has limited their widespread use [36]. Also, this type of polymer has poor mechanical properties that restrict its use to non-load-bearing grafts. Many studies have investigated the combination of polymer materials with other bone grafting materials like ceramics to get desirable properties. On the other hand, composite polymers have been designed in a chemical process called co-polymerisation to control the polymer properties, particularly the degradation rate and biological functionality to match natural bone [127, 150, 151]. The most commonly utilized copolymer for bone tissue engineering is the copolymer Polylactic-co-glycolic acid (PLGA) [103, 127, 152-155].

2.5.1.4 Composite and Coated Materials

In order to overcome the drawbacks coming from using biomaterials as single componenet, several studies have demonstrated trials of new approaches. For example, titanium scaffolds have been coated with thin layers of bioactive materials such as calcium phosphate or bio-glass to promote osteogenesis [35]. Bioactive material stimulates a specific biological response at

the interface of the scaffold leading to the formation of a natural bond and the development of new mineralised bone tissue[34]. These coatings can also protect the scaffolds from corrosion and limit the release of metallic ions into the human body [156].

On the other hand, many studied investigated the incorporation of bioceramic materials like HA particles within polymeric matrix to enhance the mechanical properties of the polymers [127, 150, 157] or mixing bioglass with natural polymer [104]. The improvement of mechanical properties strongly depends on the size, shape and distribution of the rienforced materials in the matrix [48]. Chu and colleagues mixed different ratios of HA with titanium powder to modify the mechanical properties. Their non porous composite material showed lower young modulus compared to pure titanium but still far away from the modulus of natural bone [158-160].

However, these trials could not achieve any significant success in clinical practice because they have been unable to thoroughly consider natural bone structure and properties, especially for critical-size defect at load-bearing sites.

2.5.2 Osteoconductive Properties

A perfect bone scaffold should be osteoconductive, allowing bone cells to attach and proliferate. The osteoconductive material must support bone-forming cells to migrate across the scaffold and form an extracellular matrix on its surface and inside its pores [20, 103, 161]. The osteoconductive scaffold has the ability to guide bone cells to grow on its surface to be replaced over time with new bone. In the work of Castro and collaborators, osteoconductive nanocrystalline hydroxyapatite (HA) material was produced. Their in vitro results proved that attachment, proliferation, and differentiation of bone marrow-derived MSC were significantly enhanced [85, 162-165]. In Staffa and colleagues' study, a method for making osteoconductive bioceramic porous hydroxyapatite was described. After two years of follow up, all patients’

results were clinically satisfactory, and the material with its structure promotes cell colonisation and osteointegration [85, 166]. Another study demonstrated the osteoconductive properties of a 3D printed porous scaffold of tricalcium phosphate and hydroxyapatite (TCP/HA) for vertical bone augmentation [164].

2.5.3 Optimal Architecture

According to the understanding of the mechanism of bone regeneration, bone scaffolds require a proper composition with an efficient structure to promote bone healing. Therefore, synthesised scaffolds should be porous to ensure tissue growth, vascularisation, diffusion of nutrients to cells, and waste elimination [20, 26, 48, 167]. Porosity allows cell penetration into the structure and supports cells proliferation; hence bone cells migrate into the porous avenues and then bond with the scaffold through the formation of new bone [38, 39]. However, porosity and mechanical strength are in conflict; higher porosity means lower mechanical strength [102]. This problem can be addressed by fabricating scaffolds with no more than 55% to 74% porosities to combine good mechanical strength and efficient micro-architecture [26].

Generally, the shape of pores does not influence the biological response, but the critical factor in the design of porous scaffolds is the pore size. Pore size directly affects bone regeneration since larger pores vascularise and stimulate osteogenesis faster [20, 102]. The optimal pore size should enable cell motion and ingrowth into the scaffold and, at the same time, ensure improving cell adhesion [38]. Many studies have suggested pore sizes ranging from 100 to 800 μm to be ideal for vascularisation and bone regeneration [20, 26, 85, 98, 102]. However, the optimal pore size is affected by many factors playing a prominent role in tissue formation, such as scaffold morphology, degradation rate, culture conditions, and mechanical properties of the scaffold [26, 38]. Another essential factor in ensuring proper scaffold fixation to the

surrounding tissue is the interconnectivity of the pores [168]. Interconnected micro and macro pores also provide adequate diffusion of nutrients and oxygen to cells and transport metabolic waste out of the scaffold. For successful osseointegration, pores should be open, large enough and form connected channels to each other to allow vascularisation and ease penetration of osteogenic progenitor cells into the pores [20, 40, 98, 169, 170].

2.5.4 Biodegradibility

In the treatment of large bone fractures, scaffolds made of biodegradable materials have the potential to achieve fast bridging with healthy tissue which is the first phase of the healing. Biodegradable material/scaffold can provide a crawling bridge for new bone tissue in the gap and a platform for cells to play a physiological role, which will eventually be degraded and absorbed in the body to be replaced by the new bone tissue [40]. PLGA copolymer has been used widely in bone scaffolds since the degradation rate can be controlled by modifying the ratio of its monomers [103, 127, 152-155]. Also, Brushite has been utilised as a bone-replacing material since its degradation ratio is much higher than HAp [126].

Natural bones consist of various ions such as silicon $Si^{4+,}$ sodium Na^{+}, and magnesium Mg^{2+} which play an essential role in bone formation. Using trace elements with calcium phosphate has opened a new opportunity to control the degradation ratio. Several studies have applied these ions in designing bone scaffolds to investigate their effect on bone formation and growth. [104, 147]. Also, doping with Fe ions could enhance the degradation rate of calcium phosphates by creating defects on the CaP structure. According to previous *in vitro* work, the degradation ratio of sintered brushite with concentration of Fe^{2+} / Fe^{3+} ions up to 10 mol% was higher than undoped brushite [104].

2.5.5 Angiogenic Properties

During fracture healing, bone regeneration is intimately coupled with the angiogenesis process. Angiogenesis means the formation of a new blood vessel from a pre-existing one. Bone tissue is highly vascularised; therefore, the synthesised scaffold must be able to support angiogenesis and induce the formation of new blood vessels. These new-formed blood vessels play a crucial role in fracture healing and bone regeneration [36, 171-174]. They bring nutrients and oxygen to growing cells and tissues within the scaffolds. The lack or poor vascularisation at the fracture site has been reported as one of the main reasons for delayed fracture healing or non-union [36, 171, 172]. Since the deficiency of nutrients and oxygen leads to improper cell differentiation or cell death, which eventually affects the osteogenic repair [175]. Therefore, bone scaffolds must serve as templates for establishing the vascular system and supporting bone-forming cell growth. Many studies on bioactive glasses have demonstrated their beneficial effect on angiogenesis due to the released ions during the degradation process. Other studies have proven that polymer/bioglass composites can improve angiogenesis and neo-vascularisation [146]. In addition to the scaffold's materials, its structure significantly influences vascularisation, as discussed before in (2.5.3 Appropriate Architecture). Larger pores (>100-150 μm) promote vascularisation and stimulate osteogenesis, whilst smaller pores hinder vascularisation [20, 176-179].

2.5.6 Optimal Mechanical Properties

Mechanical properties of the scaffold have a critical role in bone healing, especially at load-bearing sites [48, 180, 181]. Mechanical stability is one of the four basic principles in the diamond concept of bone healing [10], as presented above in Figure 2.7. Mechanical stability supports forming a callus that bridges the fracture, permitting loads to be transferred across the fracture site [10, 11]. From a clinical point of view, the designed scaffold should mechanically

secure and support stable fixation during the initial stages of tissue growth [103, 161]. However, to support stability and fixation of the scaffold, surgical interventions, including internal or external stabilisation systems, may be used, which eventually enhance fracture healing [10, 11].

The optimal bone scaffold must have mechanical properties closely matching the host tissue's characteristics to support its growth. For example, if the compressive strength of the bone scaffold is too low, it could not withstand the load and will be deformed, leading to improper tissue growth or preventing tissue growth at all. On the other hand, when the compressive strength of the scaffold is too high, cells will not be subjected to the required in vivo conditions to promote tissue growth [26]. Mechanical stability is more complicated in repairing large bone fractures, particularly at load-bearing sites. The healing of such cases requires a scaffold with high stiffness (elastic modulus) to maintain the applied load for the time needed without showing symptoms of fatigue or failure [182]. But, significant differences in stiffness between the scaffold and bone tissue cause different strain levels at the same stress value, leading to scaffold delamination [26]. At the same time, the higher elastic modulus of the scaffold results in a decrease in the density of the surrounding bone due to the reduced physiologic loading of the natural bone [183]. According to Wolff's Law, bone is generated and becomes stronger along the lines of the mechanical stress, so bones that are not subject to everyday stress will lose its mass [71, 184-189].

This is the major challenge of the current metallic scaffolds like titanium, where their mechanical properties exceed the surrounding bone leading to "stress shielding" [124, 190] (Figure 2.10). For example, cortical bone has Young's modulus E = 4 – 20 GPa while titanium exhibits E = 100 – 110 GPa [20, 26-28]. Thus ideal bone scaffold must have adequate

mechanical properties to minimise any risk of stress shielding and allow proper load transfer to support the regeneration of bone [48, 181, 191, 192, 193].

The material composition significantly influences the mechanical properties of the scaffold. As we explained previously in (2.5.1 Biocompatibility), several biomaterials have been investigated in the field of tissue engineering. For instance, bioceramics have elastic modulus and compressive strength very close to the human cortical bone; but they are brittle and have low fracture toughness [48]. At the same time, biodegradable polymers exhibit cancellous bone compatible mechanics. For this reason, polymer-ceramic composites were investigated to modify the mechanical properties to the required values based on the host tissue [48]. Although this strategy is valid, the mechanical properties of the synthesised scaffolds are far from those of the human cortical bone.

The tremendous variation in mechanical properties of natural bone according to location and function, as discussed before, makes it challenging to design an ideal scaffold from a single component [26, 103, 161, 182]. Therefore, most of the current scaffolds have failed clinically and caused delayed healing or non-union.

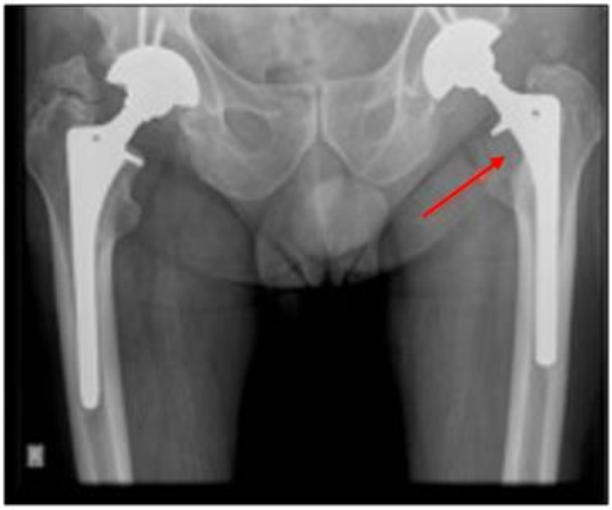

Figure 2.9: Stress shielding of the proximal femur; the red arrow refers to a local bone demineralisation due to the stress shielding around the replacement, adapted from [194].

2.6 Research Aim and Objectives

The regeneration and recovery of bone tissue is not an easy task since bone is a complex living tissue with magnificent mechanical properties and significant metabolic activity. This work aims to establish a completely new approach for the development and fabrication of bone scaffolds. Instead of focusing on a single material, a combination of different technologies, materials and fabrication techniques will be used in order to design and develop a synthetic scaffold that could imitate the unique structure and functionalities of natural bone. In order to achieve this aim,the work has included the following main objectives:

- Design and fabrication of porous titanium/10 mol% Fe^{3+} doped brushite (Ti/DCPD-Fe) scaffolds. By following the design of experiments (DOE) principles, mineral ratio, porosity and sintering parameters will be identified to get the appropriate scaffold for load-bearing applications. **(Chapter 3)**

- Characterisation of the synthesised scaffolds in terms of crystal structure, phase constitution, and microstructure using techniques such as XRD, STA, XPS, SEM and μCT. **(Chapter 4)**.

- Optimisation of mechanical properties by conducting a parametric study to identify the appropriate fabrication conditions that result in mechanical properties similar to those of natural bone. **(Chapter 5)**.

- Finite element analysis to study the stress and strain behaviour of the synthesised scaffolds. The work includes a model for a femoral fracture with the potential scaffolds

to investigate the biomechanical behaviour at the interface bone/scaffold and optimise the scaffold's design according to the needs of each patient. **(Chapter 5)**.

- *In vitro* cell compatibility and proliferation of the synthesised materials will be tested. Also, characterisation of the synthesised scaffolds after cell seeding will be conducted. **(Chapter 6)**.

Chapter 3

Materials & Methods

3.1 Introduction

This chapter discussed the materials and methods employed to synthesise porous titanium/ Fe^{3+} doped brushite scaffolds. Different characterisation techniques were used to investigate the crystal structure, composition, and porosity, including X-ray diffraction analysis (XRD), scanning electron microscopy (SEM), X-ray Photoelectron Spectroscopy (XPS) and Computed Tomography (μ-CT). Compressive testing was also conducted to calculate the mechanical properties of the synthesised scaffolds, and then numerical analysis was performed to explore the stress and strain behaviour. The protocols and procedures followed to examine the influence of the porous composite scaffolds on biological response were also described.

3.2 Materials Preparation

Commercial pure titanium powder Ti (99.7% purity, provided by Sigma Aldrich ® 268496) was used to prepare the scaffolds. The irregular shape and average size of the titanium powder are shown in Figure 3.1. Spherical potassium chloride powder KCl (99.1% purity, provided by Fisher Chemical) with a particle size range of 100 - 400 μm was used as the space holder. The particle size of the space holder (KCl) was chosen according to the literature review [38, 47, 194-196] to get a pore size larger than 100 μm to facilitate cell migration and ensure the growth of bone into the scaffold. On the other hand, using a space holder with larger particles than titanium powder would give better distribution and, eventually, better interconnectivity [197]. Figure 3.1 shows the average size and morphology of starting powders of titanium (Ti) and space holder (KCl).

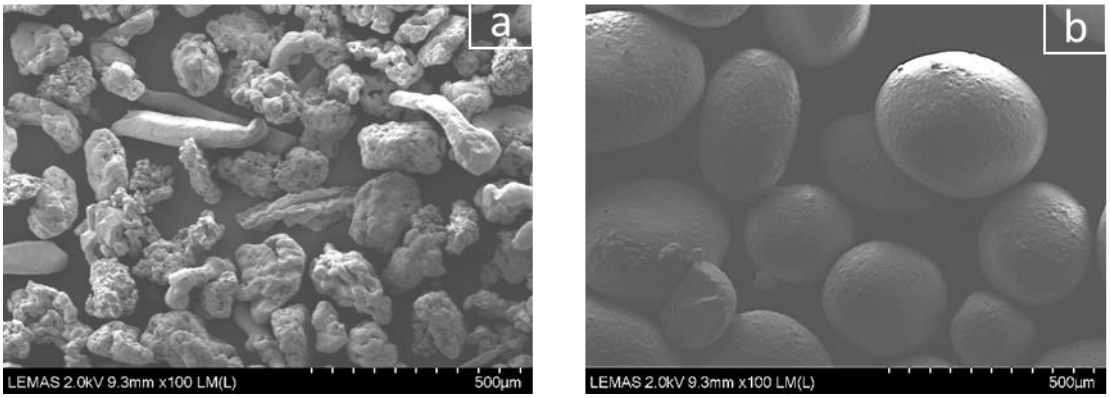

Figure 3.1: SEM images showing the particles' shape and size of titanium and potassium chloride; titanium powder with a particle size (45 - 180 µm) (a) and KCl powder with a particle size (100 - 400 µm) (b).

The Brushite powder $CaHPO_4 \cdot 2H_2O$ (Ca:P ratio 1:1) used in the fabrication of scaffolds was synthesised by the precipitation method following the procedures explained by Anastasiou, Alsubhe and Elmadani [128, 130, 198-200]. 200 mL of a 0.1M calcium solution $Ca(NO_3)_2 \cdot 4H_2O$ (Fisher Chemicals, CAS:13477- 34-4) was heated to 37˚C (solution A). Then 200 ml of a 0.1M phosphate solution $HPO_4(NH_4)_2$ (Acros Organics, CAS:7783-28-0) (solution B) was added drop by drop into solution A. The equation representing the reaction is described below [200, 201].

$$Ca(NO_3)_2 \cdot 4H_2O + HPO_4(NH_4)_2 \Longrightarrow CaHPO_4 \cdot 2H_2O + 2NH_4NO_3 + 2H_2O \qquad (3.1)$$

The A and B solutions mixture was continuously stirred at 37˚C for 2 hours. Then the mixture was covered with foil to exclude the CO_2 ingress into the solution and left without heating to stand for a further 1 hour to allow precipitation. The resultant brushite crystals were collected on a filter paper (Whatman grade 44 with 3µm pores), washed several times with distilled water and dried in an air furnace for 24 hours at 80˚C. Synthesis of the Fe^{3+} doped brushite (DCPD-

Fe) followed a similar method, but before the addition of the phosphate solution $HPO_4(NH_4)_2$, 10% mole $Fe(NO_3)_3 \cdot 9H_2O$ (VWR Chemicals, CAS: 7782-61-8) was added into the calcium nitrate solution. Figure 3.2 shows the preparation steps of preparing 10% mole Fe^{3+} doped brushite (DCPD-Fe) powder. PH was measured using a pH meter (HI991001, Hanna) during the synthesis process.

Figure 3.2: Experimental steps of preparing 10% mole Fe^{3+} doped brushite (DCPD-Fe) powder; (a): stirring process, (b): filtration process and (c): resultant powder after drying process.

3.3 Scaffolds Fabrication

Titanium powder (Ti) was the primary component for all the fabricated scaffolds. Fe^{3+} doped brushite (DCPD-Fe) mineral was added to adjust and improve the mechanical and biological properties of titanium. Potassium chloride (KCl) was mixed in different volume ratios to control the porosity of scaffolds. In order to optimise the properties of the fabricated scaffolds to imitate natural bone, the Design of Experiments (DOE) was followed as described below before starting the synthesis process.

3.3.1 Design of Experiments (DOE)

DOE is a powerful statistical method to determine the individual and interactive effects of synthesis variables (input) on mechanical properties of scaffolds (output) to develop an accurate input-output relationship [202-205]. The design included three independent variables (sintering temperature, porosity and CaP ratio) and ranges of their change by considering three levels for each, as shown in Table 3.1. The three levels of the variables (temperature, porosity and CaP ratio) were determined based on information available in the literature. Minitab software was used to create three factors Box-Behnken Design (BBD), to identify the fabrication conditions for each sample (Table 3.2). Table 3.2 displays the arrangement for 15 experimental points with 12 factorial design runs (in black) and three replicates at the centre point (in blue). Based on the design matrix, 15 samples had to be fabricated with different combinations of KCl and CaP ratios, then sintered at various temperatures.

Table 3.1: The values of the levels for the variables (sintering temperature, porosity and CaP ratio).

Factor/Variable	**Level**		
	Low (-1)	**Medium (0)**	**High (+1)**
Sintering Temperature (^{o}C)	850	1000	1150
Porosity (vol%)	0	20	40
CaP ratio (vol%)	0	5	10

Table 3.2: Box-Behnken Design matrix showing the arrangement of the required samples, including coded and real values.

Runs	Factors (Coded values)			Factors (Real values)		
	Sintering Temperature (ºC)	**Porosity (vol%)**	**CaP ratio (vol%)**	**Sintering Temperature (ºC)**	**Porosity (vol%)**	**CaP ratio (vol%)**
1	-1	-1	0	850	0	5
2	1	-1	0	1150	0	5
3	-1	1	0	850	40	5
4	1	1	0	1150	40	5
5	-1	0	-1	850	20	0
6	1	0	-1	1150	20	0
7	-1	0	1	850	20	10
8	1	0	1	1150	20	10
9	0	-1	-1	1000	0	0
10	0	1	-1	1000	40	0
11	0	-1	1	1000	0	10
12	0	1	1	1000	40	10
13	0	0	0	1000	20	5
14	0	0	0	1000	20	5
15	0	0	0	1000	20	5

3.3.2 Synthesis Process

Porous titanium/10% mole Fe^{+3} dopped brushite scaffolds were fabricated using the powder metallurgy with the space holder process. Titanium powder was mixed in different ratios (0, 5, 10 vol%) with 10% mole Fe^{+3} dopped brushite powder. The porosity was controlled by adjusting the volume ratio of potassium chloride (0, 20, 40 vol%) to titanium and brushite mixtures. Two drops of Ethanol were added to ensure proper mixing and distribution of the components. The different combinations of powders were uniaxially pressed at 250 MPa at room temperature using a manual hydraulic press with closed stainless steel die [197, 206, 207] to obtain cylindrical samples of 10 mm in diameter. Two different heights of samples were fabricated 2mm for cell work and 10mm for mechanical testing. Five minutes were given for each sample to settle in the die before taking out to avoid breakage or crumbling. Later, samples

were immersed in heated water at 80˚C for 3 hours to extract the space holder and then samples were washed and cleaned with isopropanol using an ultrasonic bath for 1 hour to get rid of the oxygen [208]. Afterwards, the samples were dried in the furnace at 90˚C for 3 hours and then thermal sintering took place [209]. Sintering process was conducted in an inert atmosphere at a flow rate of 3 L/min of Argon. Three temperatures (850, 1000, 1150 ˚C) were used for sintering with a constant time of 2 hours and a heating/cooling rate constant at 15˚C /min. Argon was on during the cooling cycle until the temperature dropped to below 400˚C to avoid oxidation.

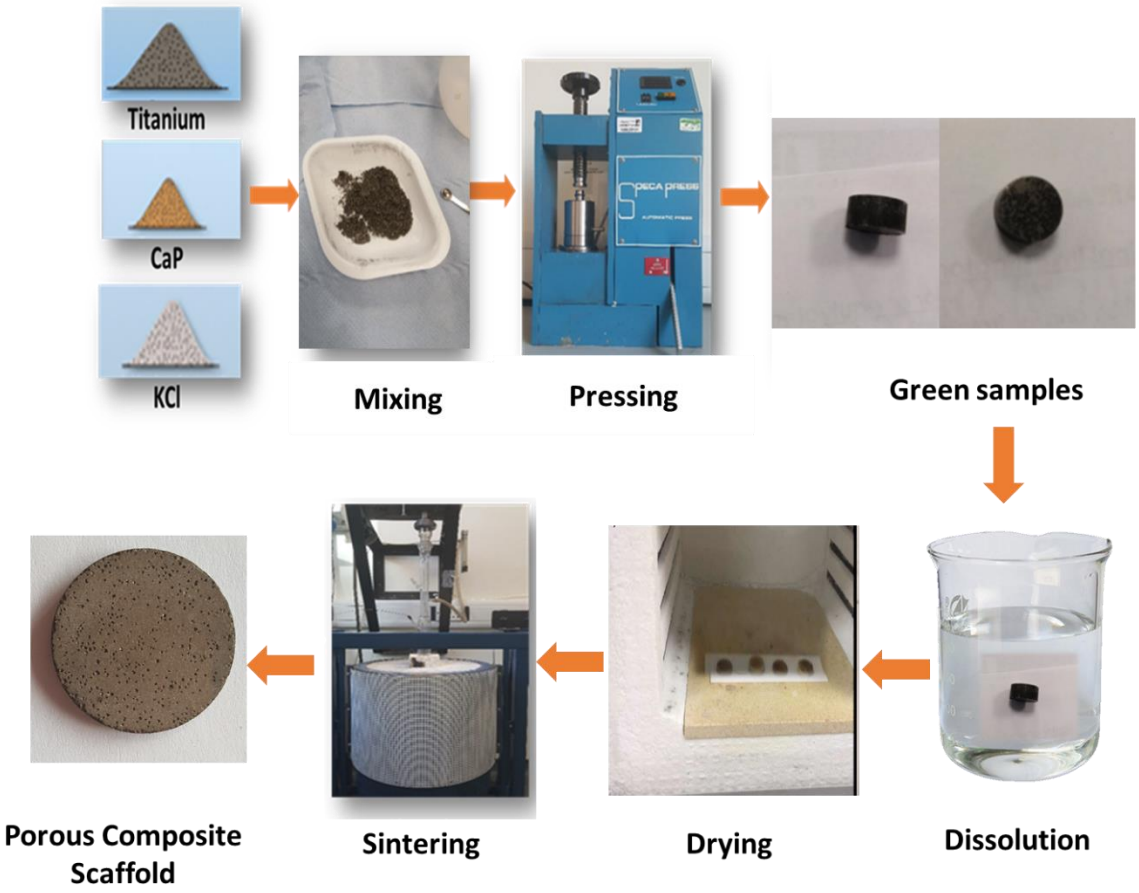

Figure 3.3: The main steps of the synthesis process of the porous Ti/ DCPD-Fe scaffolds.

Table 3.3: List of the codes of the fabricated samples referring to the KCl and CaP ratios used for the synthesis.

Code*	Designed scaffold	
	KCl (vol%)	**CaP (vol%)**
(0,0)	0	0
(0,5)	0	5
(0,10)	0	10
(20,0)	20	0
(20,5)	20	5
(20,10)	20	10
(40,0)	40	0
(40,5)	40	5
(40,10)	40	10

*Samples were coded as follows (A, B);

A = KCl (vol%)

B = CaP (vol%)

For example: (20,10) is a scaffold fabricated using 20vol% KCl to create porosity and contains 10vol% of CaP mineral.

Samples were coded as described above to make the presentation and discussion of the results easier in the following chapters.

3.4 Characterisation Techniques

3.4.1 X-Ray Diffraction (XRD)

3.4.1.1 Principle

X-ray diffraction (XRD) is a non-destructive technique utilised to study the material's crystal structure and atomic spacing. A standard XRD equipment consists of three main parts as illustrated in Figure 3.4a: i) X-ray cathode tube, which generates X-rays by heating the filament inside it to produce electrons, ii) the sample holder to place the target material and iii) X-ray

detector which rotates around the sample and its position is recorded as the angle 2θ. After generating electrons in the x-ray tube, they accelerate and hit the target material. When electrons have sufficient energy to eject the inner shell electrons, characteristic X-ray spectra are produced. The detector records the intensity of the diffracted X-rays; since the X-ray intensity is typically recorded as counts or counts per second. The detector records the number of X-rays observed at each angle 2θ. Then the material structure is identified by analysing the location, angle, and intensity of peaks [210-212]. The interaction of the incident rays with the sample produces constructive interference and a diffracted ray when conditions satisfy Bragg's Law. Bragg's law relates the wavelength to the diffraction angle and d spacing by the formula [210-212].

$$n\,\lambda = 2d_{hkl}\,sin\,\theta$$

Where:

n is an integer (order of reflection)

λ is the X-ray beam wavelength

θ is the diffraction angle (degree)

d is the distances between planes of atoms

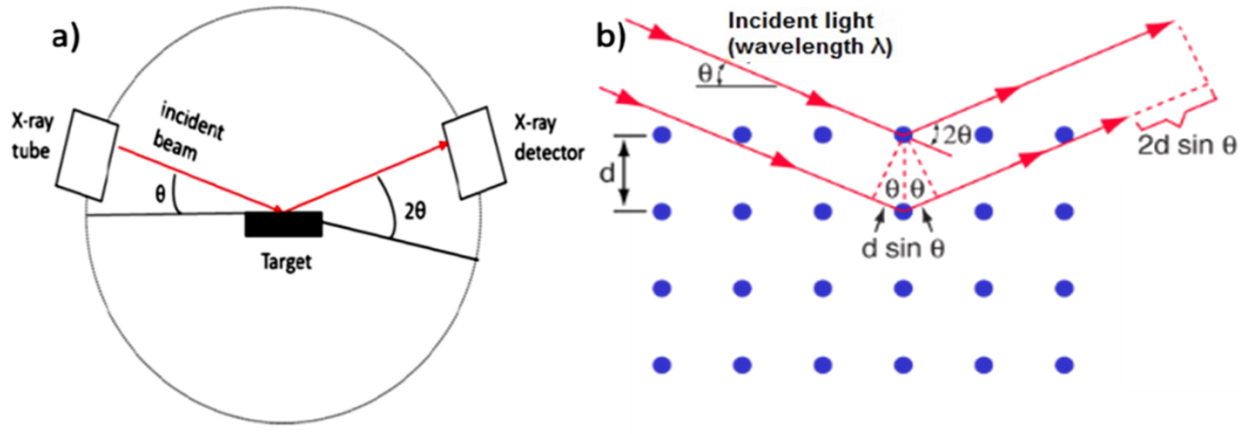

Figure 3.4: Schematic diagram of X-ray diffraction equipment consisting of an X-ray tube, a target holder, and an X-ray detector (a) and an illustration of Bragg's law (b), adapted from [210, 213, 214].

3.4.1.2 Sample Analysis

The crystalline phases of synthesised samples were determined by XRD Bruker D8 equipped with a monochromatic Cu Kα radiation source (λ= 1.54Å) generated at a voltage of 40 kV. The diffractometer step size was 0.065°, and the 2θ scanning range was from 5° to 80° with a scan speed of 1^{o} s^{-1}. Both powders and sintered pellets were analysed by X-ray diffraction using these settings. Highscore plus software (Malvern Analytical) was used to analyse the obtained XRD patterns and identify the phases.

3.4.2 Scanning Electron Microscopy (SEM)

3.4.2.1 Principle

Scanning electron microscopy (SEM) is used to study topography and composition of materials with a high resolution of ~ 1 - 20 nm [215, 216]. Features such as the size and shape of crystals or pores can be viewed by SEM [217-220]. The scanning electron microscopy (SEM) construction is illustrated in Figure 3.5a. SEM microscope consists mainly of i) an electron gun, ii) an electron optical system, and iii) an electron detection system. The system works under a vacuum to prevent electron scattering with the gas molecules. When the electron beam scans the sample's surface, electrons are emitted and penetrate the surface. As shown in Figure 3.5b, the beam interacts with the material, and then secondary and backscattered electrons are generated. The secondary electrons are caused by inelastic collisions resulting in electrons emission close to the material's surface. These electrons give the topographical contrast with high-resolution images. The backscattered electrons are higher energy and are emitted from deeper within the interaction volume. Different phases and grain boundaries of a material can be detected because of the higher backscatter coefficient of larger atomic weight materials [221].

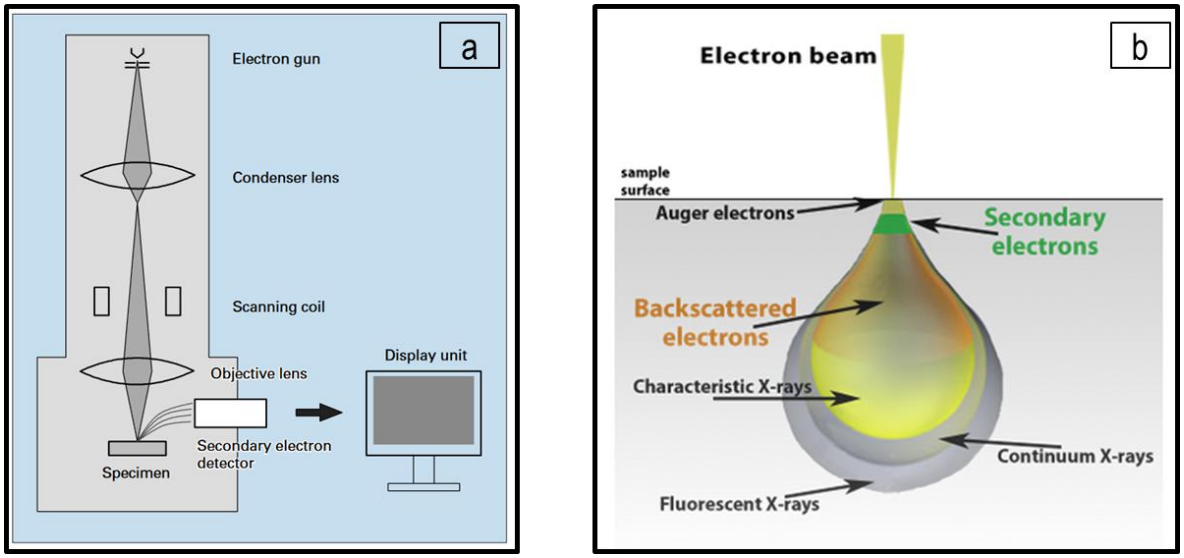

Figure 3.5: Schematic diagram showing the basic construction of scanning electron microscopy (SEM) (a) and the electron beam interaction with the target material (b) [216, 222].

Energy Dispersive X-ray Spectroscopy (EDX)

Energy-dispersive X-ray spectroscopy (EDX) is an analytical technique utilised for the elemental identification and quantitative compositional data [223]. EDX detects the energy of x-rays that are emitted from the sample. These x-ray energies correspond to specific elements. As illustrated in Figure 3.6, X-rays emitted from the material's surface enter the semiconductor detector; eventually, electron-hole pairs are produced with quantities (electric current) equal to the X-ray energy. By measuring these quantities, we can get the values of X-ray energy. Peltier cooler is used to cool down the detector to reduce the electric noise [222].

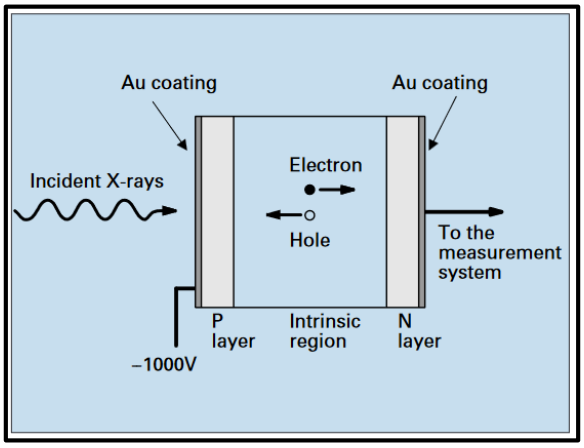

Figure 3.6: Construction of the detector for the energy-dispersive X-ray spectroscopy [222].

3.4.2.2 Sample Analysis

SEM, Hitachi SU8230 1–30 kV fitted with a cold field emission gun was used to investigate the size and morphology of powders used in the fabrication process. The microstructure and porosity distribution of the scaffolds' surfaces were also examined. Energy-dispersive X-ray spectroscopy (EDX) with Aztec processing software was used to identify the elemental composition of the synthesised materials and scaffolds.

3.4.3 X-ray Photoelectron Spectroscopy (XPS)

3.4.3.1 Principle

X-ray photoelectron spectroscopy (XPS) is a surface characterisation technique, also known as electron spectroscopy for chemical analysis (ESCA). XPS can determine the elemental composition of the surface and measure the electronic and chemical state of the material's atoms. XPS instrument consists of an X-ray source, a specimen stage, a lens, an analyser and a detector, as seen in Figure 3.7a [224]. The examination is conducted in an ultra-high vacuum ~ 10^{-8} Pa to avoid surface contamination or electrons collision with the residual molecules [221, 224]. XPS spectra are acquired by exposing a solid surface to a beam of X-rays and measuring the electrons' kinetic energy. X-rays target the electrons from the top 1-10 nm of the surface (the ultra-thin film as shown in Figure 3.7b). These ejected electrons are counted over a range of kinetic energies to obtain the photoelectron spectrum. Intensities and energies of the photoelectron peaks permit the identification and quantification of the elements [225].

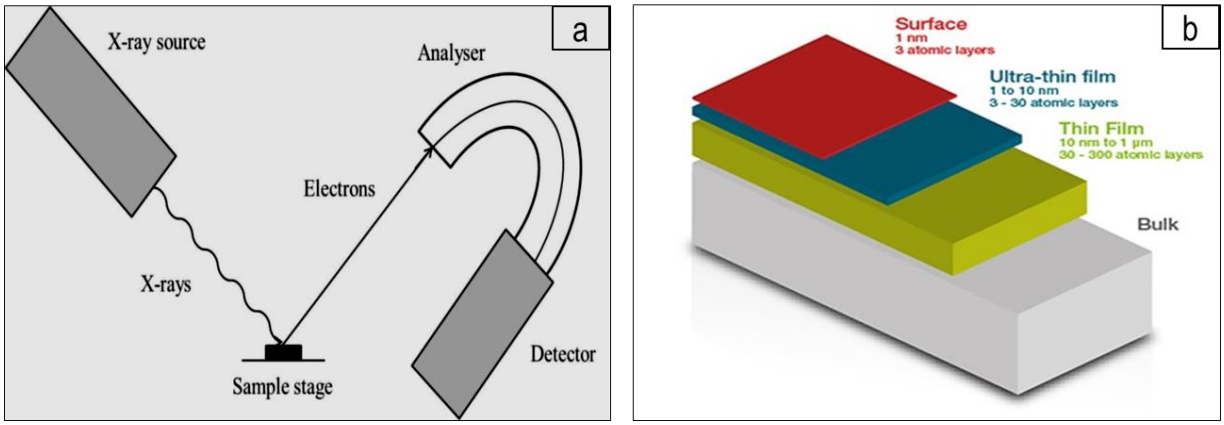

Figure 3.7: Schematic diagram showing the XPS instrument principle (a), and the surface layers identifying the depth that can be penetrated by the XPS source (the ultra-thin film in blue) (b) [221, 225, 226].

3.4.3.2 Sample Analysis

Samples were examined using a UHV XPS machine with a SPECS Phoibos 150 analyser and a SPECS XR50-M monochromated x-ray Al anode (1486.7eV) with 400W of power and 15kV anode. It was unfocussed with a spot size of 1mm x 3.5mm. The samples were charge neutralised with an electron flood gun 3eV at 25mA. The samples were measured in Medium Area mode with the surveys taken at pass energy of 50eV, and the High-Resolution scans were taken at 30eV. The software on the machine is SPECs Prodigy, and the analysis of obtained spectra was done with CasaXPS.

3.4.4 Simultaneous Thermal Analysis (STA)

3.4.4.1 Principle

STA is a simultaneous thermal technique that can be used to investigate the reactions and phase transformations which take place during the heating process of materials. In this work, STA instrument (PerkinElmer®, STA 8000), with the capability of acquiring the differential analysis feature (DTA, DSC) with the thermogravimetric analysis (TGA) was used [227, 228].

Thermo Gravimetric Analysis (TGA) is carried out to determine the weight change during material heating as a function of temperature. The holders in the STA furnace are linked to a balance which measures both the reference and sample mass [227, 229]. **Differential Thermal Analysis (DTA)** measures the change in temperature between the sample and the reference as a function of temperature. **Differential Scanning Calorimetry (DSC)** measures the amount of heat flow (energy absorbed or released) by a material during heating/cooling at a constant temperature [227, 230].

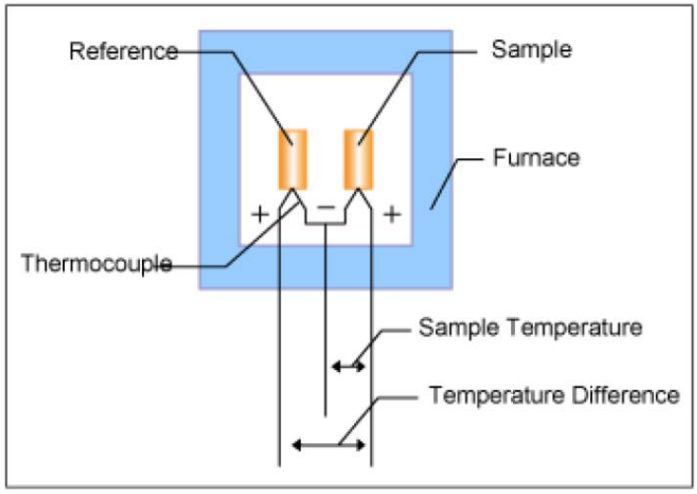

Figure 3.8: Schematic diagram showing the furnace of DTA [231].

3.4.4.2 Sample Analysis

STA technique (PerkinElmer®, STA 8000) was used to investigate the effect of heating on the phase transformation of the Fe^{+3} doped brushite powder. All thermal experiments were carried out in a nitrogen atmosphere where alumina powder (Al_2O_3) was used as a reference and ~ 8-10 mg of tested powder. The temperature range of the instrument was from ambient to 1450°C; at the beginning, the sample was held at 30°C for 1 min and then heated up to 1450°C at a heating rate of 20°C/min. Then, the sample was kept at 1450°C for 1min before cooling down to 30°C temperature at a cooling rate of 20°C/min.

3.4.5 Helium Pycnometer

3.4.5.1 Principle

Helium pycnometer is a method to measure the skeletal volume of a pre-weighed sample by gas displacement (helium displacement). Helium (with 0.260 nm dynamic diameter) has excellent permeability and can penetrate even the most minor voids or pores in the sample; therefore, more accurate results can be obtained. Also, this method is entirely automatic, starting from calibration and ending by calculating the results, which avoids human errors [232, 233]. This method employs Boyle's law (volume-pressure relationship) and gives the most accurate estimation of open porosity since helium has a high diffusivity and can penetrate even the most refined pores in the structure. However, the helium pycnometer technique can quantify only the open porosity accessible to the helium. The schematic diagram of the helium pycnometer is shown in Figure 3.9. The pycnometer consists of two interconnected chambers: a sample chamber and an expansion chamber equipped with three valves: fill valve, expansion valve and vent valve to control helium flow in the system and connected with temperature and pressure sensors. At the beginning of the test, the dry sample is placed inside the sample cell and then loaded in the sample chamber (of known volume $V_{sample\ chamber}$), and the whole system is flushed with helium several times to get rid of any gases. Helium is introduced and fills the sample chamber penetrating all accessible pores in the sample. The helium pressure is measured as (P_1) and then released to the expansion chamber, decreasing to a new stable level (P_2). The sample volume can be calculated using the gas law from the following equation [232, 234, 235].

$$V_{sample} = V_{sample\ chamber} - V_{He} \qquad (3.2)$$

$$V_{sample} = V_{sample\ chamber} - \frac{V_{expansion\ chamber}}{\frac{P_1}{P_2} - 1} \qquad (3.3)$$

The skeletal density of scaffolds ρ is defined as the ratio of mass (M) to the solid volume ($V_{pycnometric}$), which is the volume of the solid material with the closed pores (inaccessible to the helium), as shown in Figure 3.10.

$$\rho = \frac{M}{V\ \text{pycnometric}} \qquad (3.4)$$

The volume of the pores that are accessible to helium gas (open pores) can be calculated from:

$$V_{pores} = V_{total} - V_{pycnometric} \qquad (3.5)$$

The open porosity (P_{open}) is defined as the ratio of the volume of open pores (V_{pores}) to the total volume (V_{total}).

$$P_{open}\,(\%) = \frac{V\ \text{pores}}{V\ \text{total}} \qquad (3.6)$$

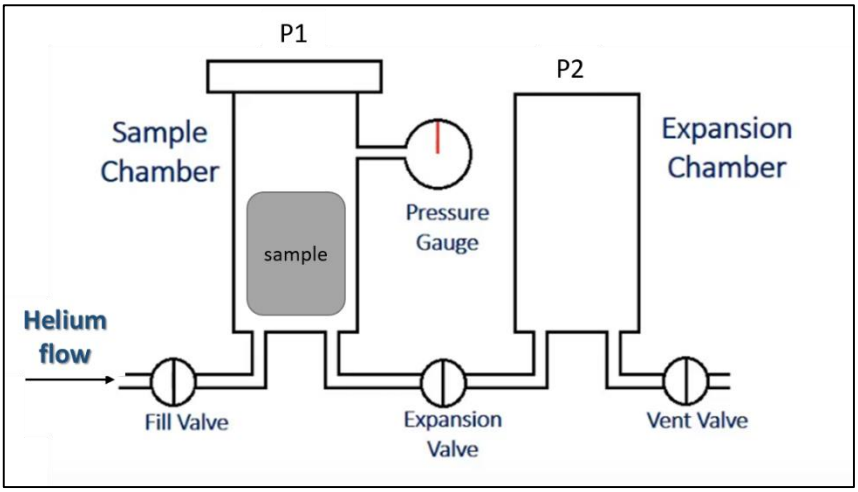

Figure 3.9: Schematic diagram of the basic construction of helium pycnometer [232].

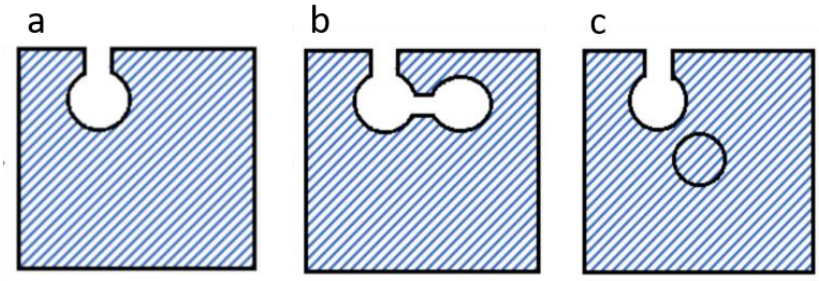

Figure 3.10: Blue shaded areas refer to the measured volumes by a helium pycnometer; (a) with an open pore; (b) with open and interconnected pores; (c) with an open pore and closed pore, adapted from [234].

3.4.5.2 Sample Analysis

The skeletal density and open porosity of the scaffolds were measured using the helium pycnometer (Pycnomatic ATC, Thermofisher Scientific). The helium pycnometer method offers excellent temperature control to avoid volume changes during the measurement. The procedure was set up to take repeat measurements for each sample until three density values were obtained with a standard deviation < 0.5 %. Triple samples for each composition were used, and then an average of those values was calculated.

3.4.6 Micro Computed Tomography (µ-CT)

3.4.6.1 Principle

Micro-CT is a 3D imaging technique that uses X-rays to visualize and map the internal structure of an object with resolutions ranging between 1 and 100 µm [236-238]. This characterisation technique is used to study biological samples or composite materials to check the morphology and identify features such as density, porosity, particle size, etc. [239]. The target is rotated between a fixed X-ray source and a fixed X-ray detector in a micro-CT scanner, as shown in Figure 3.11. The source generates X-rays that pass through the specimen and are then recorded by the detector as 2D projections. The sample keeps rotating on the stage with a specific increment to get a series of X-ray projection images through a 180 degrees turn (or 360 degrees). These 2D images show the cross-section planes of the sample geometry, which are then reconstructed to create a 3D model. The generated X-ray intensity is dependent on the acquisition parameters, including the current, the voltage and the use of a filter [237, 240].

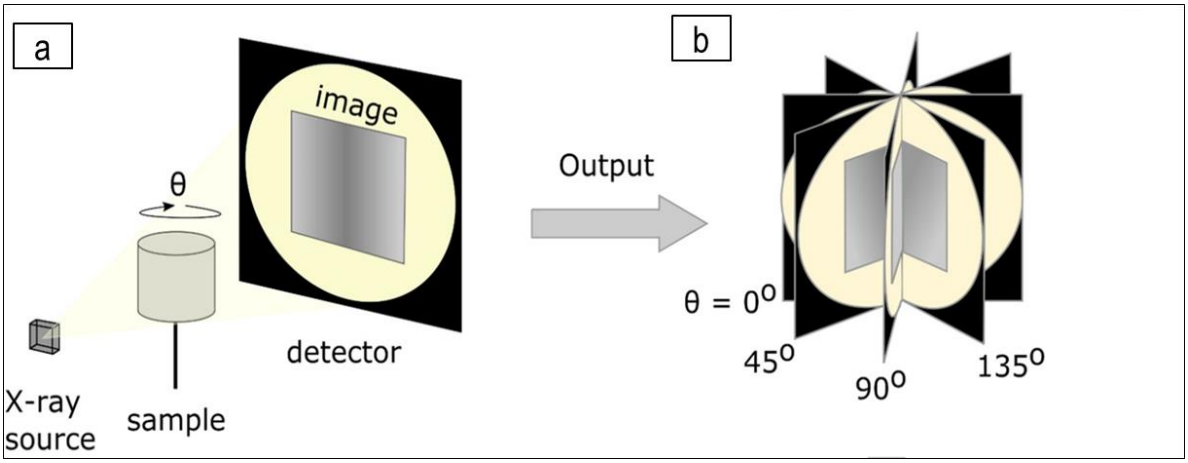

Figure 3.11: Schematic diagram of the basic construction of micro-CT scanner; the X-ray source, the sample on the rotating holder, and the detector (a) and the raw output as a series of 2D projection images of the sample recorded at different angles (b), adapted from [236].

3.4.6.2 Sample Analysis

The porous scaffolds were examined using three-dimensional Micro-CT (Skyscan 1172, Bruker, Belgium). The X-ray source was kept constant at 100 kV and 100 μA using two filters of 0.5 mm Aluminum. Fourteen hundred 2D slices were recorded with a rotational step of 0.4 degrees. The total scanning time was 80 min with an image resolution of 10μm. The 3D scaffold structure was reconstructed from the 2D projection images using (Nrecon, SkyScan) software. Then, Dragon Fly (2020.2.0.941) software was used for the analysis.

3.5 Mechanical Testing

3.5.1 Optimisation of Mechanical Properties

A parametric study was conducted to optimise the mechanical properties of porous titanium/ Fe^{3+} doped brushite (Ti/DCPD-Fe) scaffolds. Synthesis parameters that significantly influence the development of mechanical properties were considered in the research. The fabrication parameters involved: sintering temperature, porosity and CaP ratio, which were the study's

input (variables). The modelling and analysis aimed to investigate the influence of every single factor of the synthesis parameters and their interactions on the mechanical properties of the scaffolds [204, 241]. The work started by following the design of experiments (DOE) principles [242] for manufacturing 13 different scaffolds as described in Chapter 3 (section 3.3). Then data were collected from the compressive test, including Young's modulus, ultimate compressive strength and yield strength, which were the output (responses). Finally, the analysis was performed using Minitab 21.2 software to get the theoretical models which can be used to design a scaffold with mechanical properties matching the bone properties to decrease the risk of stress shielding.

Eq (3.7) presents the second-order polynomial regression model used to fit the experimental data considering the number of factors and levels.

$$Y = a_0 + \sum_{i=1}^{3} a_i X_i + \sum_{i=1}^{3} a_{ii} {X_i}^2 + \sum_{i=1}^{2} \sum_{j>1}^{3} a_{ij} X_i X_j \qquad (3.7)$$

Where; Y represents the response (Young's modulus, compressive strength or yield stress); a_0, a_i, a_{ii}, and a_{ij} are the regression coefficients for intercept, linear, quadratic and interaction terms, respectively. X_i and X_j are the independent factors.

3.5.2 Experimental Work (Data Collection)

Mechanical properties of the synthesised scaffolds were calculated by conducting compression testing. The compressive test was done using INSTRON 5569 test machine (load cell capacity = 100 kN) to quantify the stiffness of the scaffolds and the ultimate load to failure. Cylindrical samples with a diameter of 10 mm and a height of 10 mm were prepared. The samples were compressed at a crosshead speed of 0.001 mm/s according to the standard ASTM E9-89a. The compression testing was carried out in the longitudinal direction at room temperature, and the

test was performed three times (n = 3). Following the arrangments in Table 3.2, (45 samples) were fabricated for the compression test (15x3) in order to investigate the influence of the synthesis parameters on the mechanical properties of the scaffolds. In the beginning, calibration for the machine was done by doing a compression test for a commercial pure titanium rod with known mechanical properties. The mechanical properties were derived from the stress-strain curves. Based on the dimensions of the cylindrical samples, length (L=10mm) and diameter (D=10mm), stress and strain were calculated by applying the following formulas.

$$\sigma = \frac{F}{A} \qquad (3.8)$$

$$\varepsilon = \frac{\Delta L}{L} \qquad (3.9)$$

Compressive Elastic modulus (Young's modulus) was calculated from the slope of the elastic region of the stress-strain curve [243].

$$E = \frac{\Delta \sigma}{\Delta \varepsilon} \qquad (3.10)$$

Yield stress was determined using the 0.2% offset method to identify the beginning of plastic deformation [244, 245]. Ultimate compressive strength was defined as the maximum stress before scaffold failure [243].

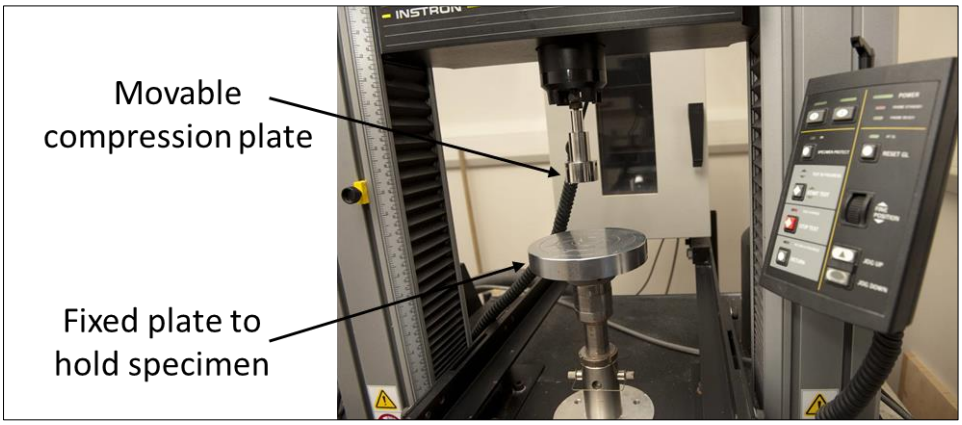

Figure 3.12: INSTRON 5569 Universal testing machine.

3.6 Numerical Work

Numerical analysis was vital to accomplish a comprehensive understanding of the mechanical behaviour of the synthesised scaffolds. Finite element analysis using ANSYS WORKBENCH 2020 R1 was done to investigate the mechanical behaviour of damaged human femur bone with the synthesised scaffolds during standing up. Finite element analysis using ANSYS WORKBENCH software was done to investigate the mechanical behaviour of damaged human femur bone with the synthesised scaffolds during standing up. The femur bone sustains the largest percentage of body mass during daily activities providing support to the human body, and injuries may occur in any part of it [42, 43, 246]. In this analysis, we considered femoral shaft fracture, one of the most common femur injuries requiring special care being a load-bearing site [42, 83, 84]. The model consisted of a femur bone with a segmental defect of 50mm that was filled with the designed cylindrical scaffold. All the models were subjected to a compressive load on the femoral head equal to the body weight and fixed support at the distal end.

3.6.1 CAD Geometry

The femur bone has a very complex geometry, so a pre-existing model was used in this study. The pre-existing model helped save time, simplify the procedures and get the best results. The CAD was for human femur bone prepared by Digital Imaging and CT Scan (Figure 3.13a) [247]. The femur was for the left leg of a male (age 44, weight 85 kg and height 185 cm [247]. Then, a segmental defect of 50mm was modelled as shown in Figure 3.13b. The created defect in the femoral shaft was filled with a cylindrical scaffold (Figure 3.13c). The design aimed to mimic the most common femoral shafts fractures caused by high energy trauma, as illustrated in Figure 3.14.

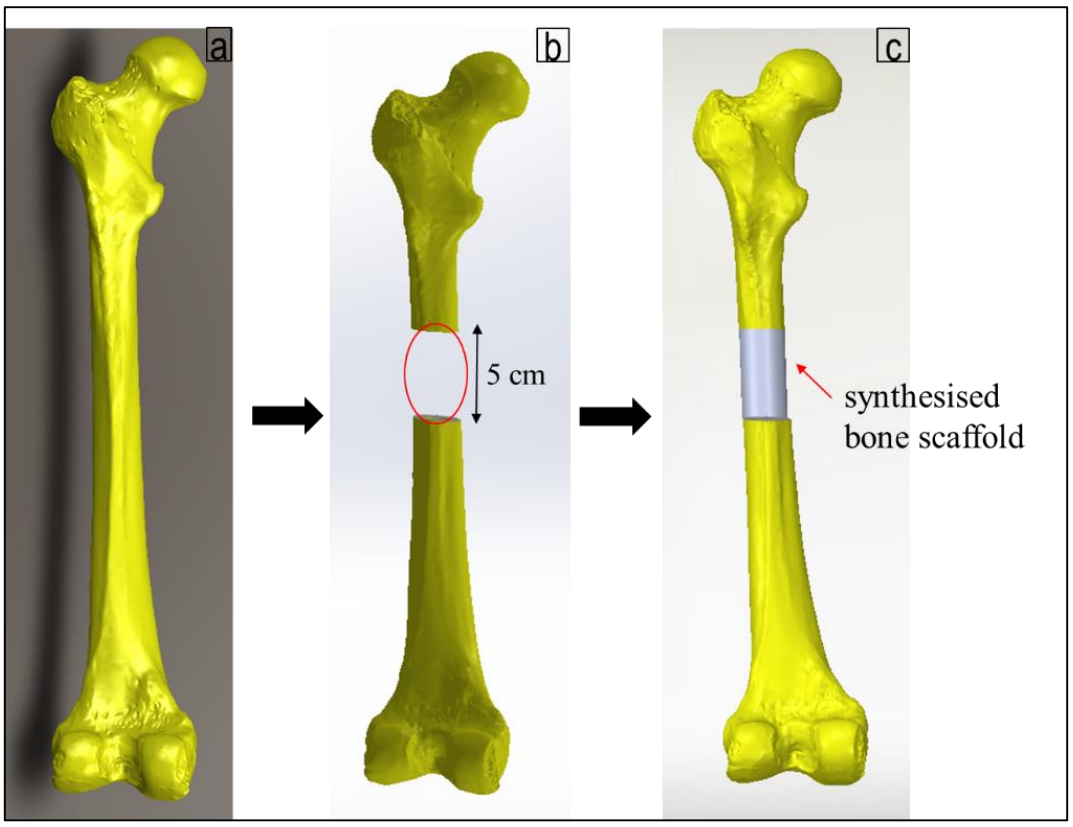

Figure 3.13: The CAD used in the numerical work; a) femur bone of a male with original dimensions, b) femur bone with 5cm segmental defect in the shaft, and c) the femoral defect was replaced and filled with the designed scaffold.

Figure 3.14: Femoral shaft fracture after high energy trauma (right side, 29 years old man).

3.6.2 Materials Properties and Meshing

Mechanical properties of natural bone vary according to the location and function, as mentioned in the literature review in Chapter 2. Therefore in this study, mechanical properties of cortical femur bone were assigned, as shown in Table 3.4. The study assumed that bone is a homogeneous, isotropic and linearly elastic material [42]. For the synthesised scaffolds, experimental density and mechanical properties were employed in the numerical work. The structure of femur bone is irregular; therefore, our designs were meshed using tetrahedral meshing [42, 248]. In order to get independent results of the number of elements, the solution was done three times by increasing the number of elements to get better results. Proper settings and values were executed to use more minor elements on proximities and curvatures for the model [249].

Table 3.4: The physical and mechanical properties of cortical femur bone used in this study [42, 244].

Property	Cortical Bone
Density [Kg/m^3]	2000
Young's Modulus [Gpa]	12
Poisson's ratio	0.33

3.6.3 Boundary Conditions

The boundary conditions included applying a load equivalent to the patient's body weight on the femoral head (B), and the distal end of the femur was fixed support (A) [249, 250]. By considering a healthy male with an average body mass of 85 kg, the equivalent load for the standing of his body was applied, as shown in Figure 3.15.

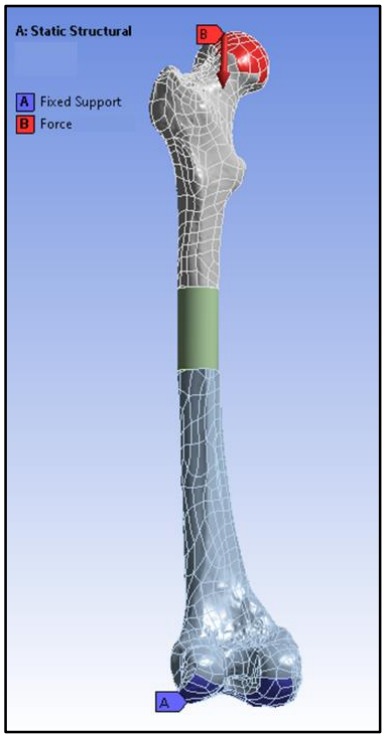

Figure 3.15: The Boundary conditions applied to the models; force on the femoral head in red and fixed support at the distal part in purple.

3.7 *In Vitro* Cell Experiments

3.7.1 Cell Culture

Before cell experiments, all the tools, including forceps, moulds and scissors, were autoclaved on moist heat at 120^{o}C for 2hr. Samples were cleaned three times with 70% ethanol, dried in air for 30 minutes, and then sterilised with UV light for 1 hr. G292 cells (Provided from tissue bank, division of Oral Biology, School of Dentistry, University of Leeds) were maintained with high glucose Dulbecco's Modified Eagle's Medium (DMEM) (SIGMA-ALDRICH, Life Science) at 37 °C and 5% CO_2. G292 cell line is a cell line that has fibroblast morphology and was isolated from the bone of Human Caucasian osteosarcoma derived from a primary osteosarcoma of a 9 year old Caucasian female. G292 cell line is immortalised, continuous cell line and therefore proliferate indefinitely. G292 cell line is widely used in bone related research, in particular for cell proliferation and cytotoxicity assay, as it is a more stable cell line and less aggressive (proliferates slowly) [251].

The medium was supplemented with 10% Fetal Bovine Serum (FBS), 1% PenStrep and 1% L-Glutamine. Cells were washed with phosphate-buffered saline (PBS) (137 mM NaCl, 2.7 mM KCl, 10 mM Na_2HPO_4, and 1.8 mM KH_2PO_4; pH 7.4.) and supplied with fresh medium every 2-3 days. When cells reached 80% confluence, they were rinsed with PBS and then detached with trypsin (5 ml for 175 cm^2 flask) for 5min at 37°C and 5% CO_2. The detached cells were concentrated by centrifugation at 1200 rpm for 5min at room temperature. The supernatant (liquid solution) was then taken out, and the pellet of cells was diluted and counted to get the required number of cells per ml. Cells were seeded onto the scaffolds and incubated at 37°C and 5% CO_2.

3.7.2 Biocompatibility Analysis

Biocompatibility of the synthesised scaffolds was investigated using the contact and extract cytotoxicity tests.

3.7.2.1 Contact Cytotoxicity Assay

Samples (n = 3 per group) were fixed to the centre of six-well plates using steir-stripe (3M Health Care). 40% anhydrous Dimethyl sulfoxide (DMSO) and steir-stripe were prepared in triplicate as positive and negative controls, respectively. 2ml of culture medium containing G292 cells at a density of 1×10^4 was added to each well and incubated at 37°C in 5% (v/v) CO_2 for 72 hours. Following this, the medium was gently aspirated, and the wells were washed with PBS and fixed with 10% (v/v) neutral-buffered formalin (NBF) (Cellpath) for 10 minutes. After discarding the formalin, the wells were washed with PBS and stained with enough Giemsa solution (4mg in 4ml ethanol) (technical grade, SIGMA) for 10 minutes. The wells were rinsed with water until the water ran clear, then dried in air for 24 hours. The stained samples and controls were examined to observe cell viability, morphology, and confluency using Leica DMI6000 B inverted microscope under bright field illumination. All the images were captured digitally using the LEICA DFC295 camera.

3.7.2.2 Extract Cytotoxicity Assay

Alamar Blue is a sensitive and accurate test known as resazurin reduction applied to measure cell viability. In this work, samples (n=3 per group) were incubated in pure DMEM medium (ratio of $3cm^2$/mL ISO10993-12) for 72 hours at 37°C in 5% (v/v) CO_2. The extract supernatant was then collected and used for the extract cytotoxicity experiment. G292 cells at a density of 1×10^4 cell/200µL were seeded on 96-well plates and incubated for 24 hours. Then, the culture medium was removed and replaced with 178µL of the extract supernatant mixed with 20µL

FBS and 2µL LG and incubated for 24 hours. For controls, we used cells cultured in DMEM medium as negative control and cells cultured in 40% Dimethyl sulfoxide (DMSO) as a positive control (in triplicate). After incubation, the compounds were aspirated carefully, and a fresh culture medium with 10% Alamar Blue (Invitrogen by Thermo Fisher Scientific) was prepared. 200µL of the medium mixture (180µL DMEM + 20µL Alamar Blue) was added to each well and incubated in the dark at 37°C for 4 hours. Eventually, the fluorescence was measured with excitation wavelength at 530-560nm and emission wavelength at 590nm using the plate reader (Varioskan Flash, Thermo Scientific).

3.7.3 Cell Attachment and Proliferation

Agarose wells were used to restrict cells to stay on the surface of pellets during cell seeding. Therefore, 10mm diameter 316L stainless steel moulds were fabricated, as shown in Figure 3.16a. The fabricated moulds were suspended 2mm above the bottom of the 12-well plates, as displayed in Figure 3.16b. Then, 5 ml of 4% agarose gel (prepared using PBS and autoclaved for 3 hours) was poured into the 12-well plates. After the gel had cooled and set, the sterilised pellets were placed into the agarose wells (n=3 per group). 1 ml of cell suspension with a density of 1×10^4 cells was seeded onto the top of each pellet, and then the well plates were incubated. Cell attachment and proliferation were investigated using fluorescence imaging and PicoGreen DNA assay.

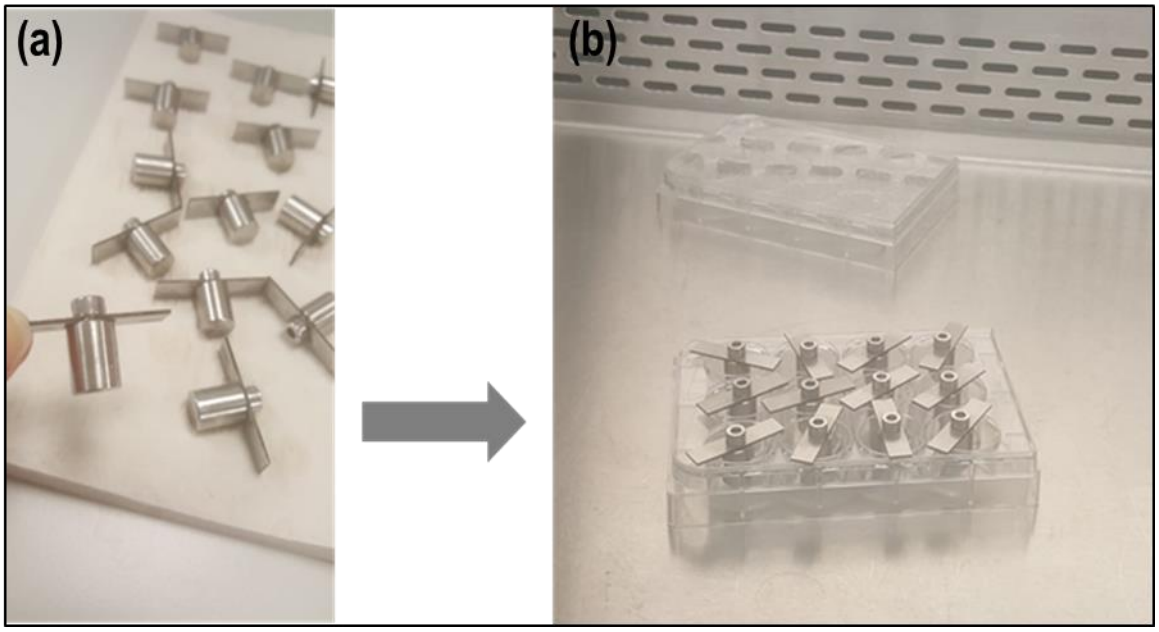

Figure 3.16: Stainless steel moulds were fabricated for preparing agarose wells to restrict cells from staying on the surface of the scaffolds.

3.7.3.1 Fluorescence Imaging

Preparation

Fluorescence imaging using confocal microscopy was done to examine the adhesion of cells on the scaffolds' surface. After three days of incubation, pellets were washed with PBS, and cells were fixed with 4% (v/v) neutral-buffered formalin (NBF) for 15 minutes at room temperature. Cells on the top of pellets were washed gently with PBS and permeabilised using 0.1% Triton X-100 (Alfa Aesar) in PBS for 15 minutes and then washed twice with PBS. For staining actin of cells: Alexa Fluor 488-phalloidin solution (Invitrogen by Thermo Fisher Scientific) was added to each sample and incubated for 60 minutes in the dark at room temperature, then washed twice with PBS. For staining nuclei of cells: 4',6-diamidino-2-phenylindole DAPi dye (Sigma-Aldrich) was added and incubated for 30 minutes in the dark at room temperature, then washed twice with PBS. Finally, confocal fluorescence microscopy

(Leica DM6 CS) was used to observe the actin and nuclei of cells attached to the scaffolds' surface.

Confocal Fluorescence Microscopy

Confocal microscopy is widely used in biological science disciplines to observe the detailed structure of cells and tissues. Confocal microscopy is an optical imaging technique giving high clarity and contrast images with more excellent vertical and horizontal resolution. A series of thin slices of the sample can be reconstructed into a 3D structure. The principle of confocal laser microscopy is illustrated in Figure 3.17. Laser light transmits through a very small area (pinhole 1) and illuminates a defined spot at a specific depth within the specimen, resulting in fluorescent light emission at this point. A dichroic mirror reflects the light to the sample, and the microscope objective will focus the light in a specific spot. The same dichroic mirror transmits the fluorescence from sample fluorophores to the detector. Pinhole 2 cuts off signals out of focus and allows the fluorescence signals from the illuminated spot to enter the detector. By scanning the specimen in a raster pattern, images of one single optical plane are created. 3D objects can be visualised by scanning several optical planes and stacking them using a suitable microscopy deconvolution software (z-stack). It is also possible to analyse multicolour immunofluorescence stainings using state-of-the-art confocal microscopes, including several lasers and emission/excitation filters [252-254].

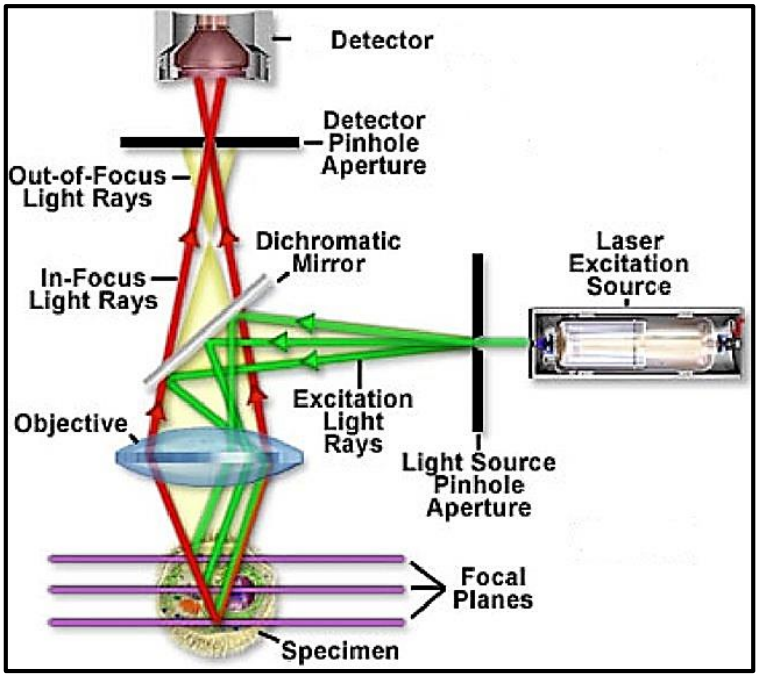

Figure 3.17: Schematic diagram illustrating the principle of the confocal fluorescence microscope [252, 253].

3.7.3.2 PicoGreen dsDNA Assay

PicoGreen dsDNA quantitation assay was used according to the manufacturer's instructions. G292 (1×10^4 cells/well) were cultured on the samples, and their proliferation was quantified at four different periods (4 hours, 1 day, 3 days and 7 days) using Quant-iT PicoGreen dsDNA assay (Invitrogen by Thermo Fisher Scientific). The protocol followed to prepare samples for DNA quantitation was described in detail in **Appendix B**. The plate reader (Varioskan Flash plate reader, Thermo Scientific) was used for fluorescence examination for DNA evaluation at excitation wavelength 480 nm and emission of 520 nm. Then data were calibrated using a DNA standard curve.

3.7.4 Statistical Analysis

The data were expressed as means ± standard deviation (SD) and then analysed using one-way analysis of variance ANOVA. The statistical analysis was carried out using MS Excel Software, and P-value < 0.05 was considered a statistically significant difference [255].

3.8 Conclusion

The materials preparation and fabrication process of the scaffolds were described in this chapter. The principles and methods of characterisation techniques used to achieve the project objectives were explained. Parameters acquisition for machines, standards and protocols for tests were also defined. This chapter presented all the required information to prepare for the upcoming chapters 4, 5, and 6, where all the results will be presented and discussed.

Chapter 4

Characterisation of Synthesised Materials and Scaffolds

4.1 Introduction

This chapter started with a detailed characterisation of the synthesised mineral (10 mol% Fe^{3+} dopped brushite; DCPD-Fe) to observe phase stability, phase transformations, and morphology. Then, the titanium (Ti) and composite scaffolds (Ti with DCPD-Fe) were characterised to investigate the phase constitution and crystal structure. The scaffolds' porosity was also characterised, considering the distribution of pores, pore size and interconnectivity to assess the validity of the synthesised structures for implantation in bone tissue engineering.

4.2 Mineral Characterisation

4.2.1 pH Values during the Synthesis Process

The synthesis of calcium phosphate minerals is highly dependent on the pH, which significantly affects the phase stability and the supersaturation condition [199, 256, 257]. Therefore, pH values were recorded during the synthesis of 10 mol% Fe^{3+} doped brushite (DCPD-Fe). During mixing the solutions as described in chapter 3 (section 3.2, Materials Preparation), pH variation over time was monitored at a constant temperature of 37ºC (Figure 4.1).

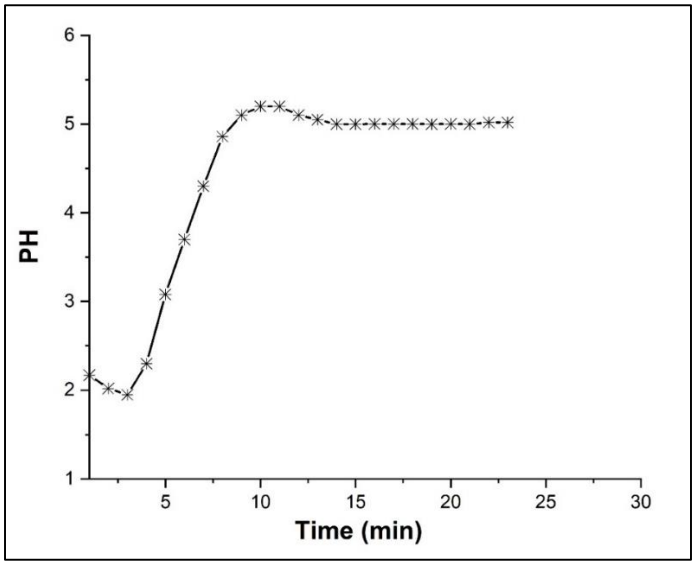

Figure 4.1: pH changes over time during the synthesis of 10 mol% Fe^{3+} doped brushite (DCPD-Fe). Measurements were carried out at a constant temperature of 37ºC and under continuous stirring.

The iron nitrate doped into the calcium solution resulted in an initial drop of pH to ~ 1.95. The addition of phosphate solution initiated the reaction and increased pH that reaching a steady value of ~ 5.0 at the end of the synthesis process. According to the literature review, pH within the range of 3.5 – 6.5 with a low solution Ca/P ratio would produce brushite minerals (CaHPO4•2H2O) at a constant temperature of ~ 37ºC [200, 258, 259].

4.2.2 Phase Transformation

The phase transformation after heat treatment for the synthesised mineral was analysed by X-ray powder diffraction. Figure 4.2a presents a comparison of diffraction patterns of the Fe^{3+} doped brushite (DCPD-Fe) powders before and after heating in an inert atmosphere at 1000º C for two hours. Figure 4.2b shows XRD analysis of the initial mineral since all the significant peaks associated with 2θº ~ 11.65°, 20.95°, 23.47°, 29.25°, 30.54° were linked with brushite phase with reference pattern (JCPDS-01-074-6549 card). Therefore, the synthesised mineral can be considered as brushite ($CaHPO_4.2H_2O$) with minor quantities of monetite ($CaHPO_4$)

(JCPDS-04-011-3070 card), evident by the peak (*) at $2\theta^{o} \sim 26.58°$. As shown in Figure 4.2c, the XRD pattern of the synthesised mineral dramatically changed after sintering at 1000 ^{o}C and transformed into β-pyrophosphate (β-$Ca_2P_2O_7$) since the majority of the peaks coincide with the peaks of the reference pattern (JCPDS-00-017-0499) [128, 130, 200].

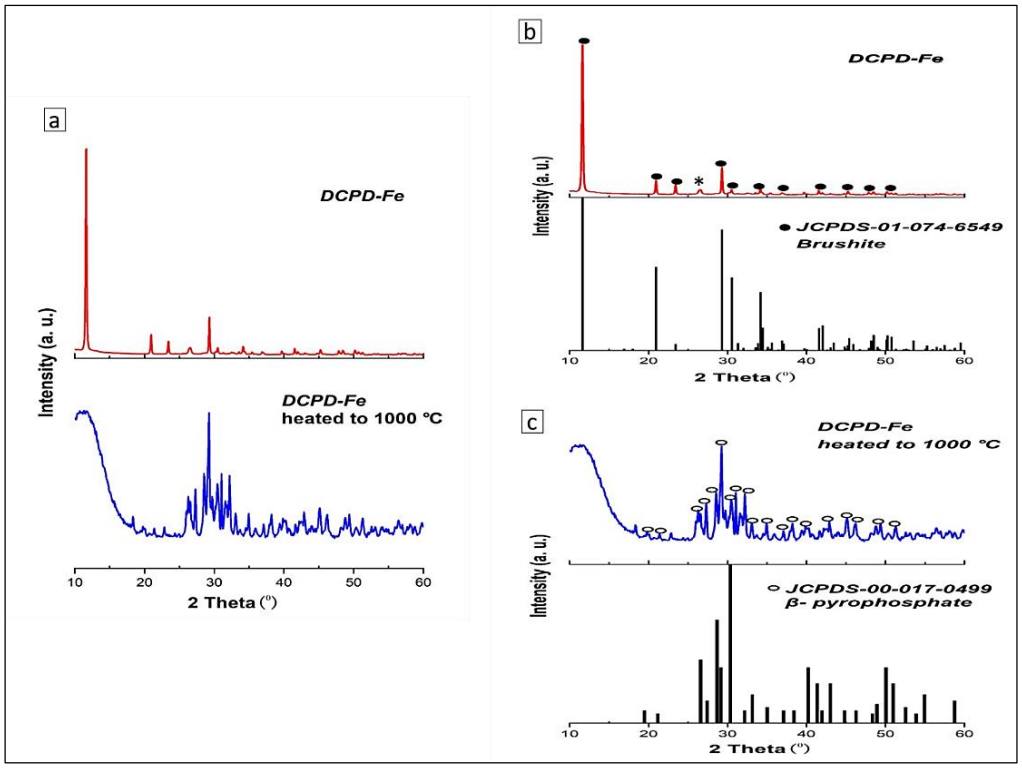

Figure 4.2: A comparison of X-ray diffraction patterns of the initial and heated 10 mol% Fe^{+3} doped brushite (DCPD-Fe) (a); mineral before heating (b) and after heating in argon at 1000^{o}C for 2h (c), with indexing to the JCPDS reference files of brushite (•), monetite (*) in (b) and β-pyrophosphate (o) in (c).

4.2.3 Simultaneous Thermal Analysis

Differential scanning calorimetry (DSC) and thermogravimetry analysis (TGA) were carried out to investigate the phase transformation temperatures of the Fe^{+3} doped brushite powder during heating. The synthesised powder was heated at a constant rate of 20 ^{o}C/min with a

temperature range of 30 °C -1450 °C [260]. The changes in weight and enthalpy were recorded during heating, as depicted in Figure 4.3. As can be observed, there were five stages of decomposition during the heating process. The first transformation occurs at ~ 204 °C when DCPD-Fe powder loses two water molecules and transforms into monetite ($CaHPO_4$) (Eq. 4.1). A second transformation happened upon heating to ~ 470 °C, leading to the formation of γ-pyrophosphate (γ-$Ca_2P_2O_7$) following the reaction in (Eq. 4.2). This reaction was accompanied by a reduction in weight due to the loss of ½ H_2O. The exothermic peak at ~ 715 °C was linked to β-pyrophosphate (β - $Ca_2P_2O_7$), which eventually changed at 1050°C to α-pyrophosphate (α-$Ca_2P_2O_7$). However, numerous studies have found that the α phase has converted back to the β phase during cooling due to the unstable nature of α- $Ca_2P_2O_7$ [130, 261, 262]. Thus, XRD data (Figure 4.2) showed the presence of β-pyrophosphate within the structure after heating. The melting point was identified at ~1294 °C. Changes in mineral weight were observed during the thermal process since ~ 27% reduction in mass occurred compared to the starting value. Obviously, ~ 21% of the weight drop was due to the water loss during the transformation of brushite to monetite, and another ~ 6% reduction took place during the formation of γ-pyrophosphate (γ-$Ca_2P_2O_7$).

$$2CaHPO_4 \bullet 2H_2O \xrightarrow{204°C} 2CaHPO_4 + 4H_2O \qquad (4.1)$$

$$2CaHPO_4 \xrightarrow{470°C} Ca_2P_2O_7 + H_2O \qquad (4.2)$$

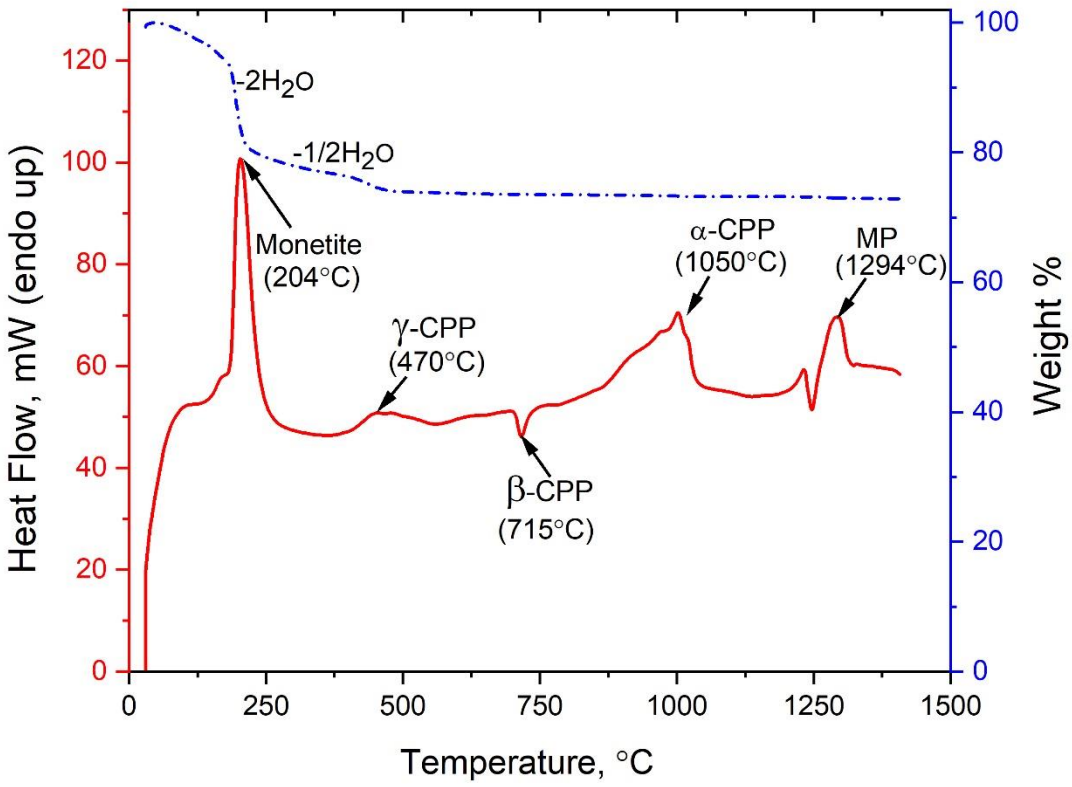

Figure 4.3: Thermal analysis of the Fe^{3+} doped brushite (DCPD-Fe) powder, identifying the phase transformation during heating up to 1450°C with a constant rate of 20 °C/m. The DSC curve is shown in red (values reported on the LH y-axis), and the TGA curve is shown in dash blue (values reported on the RH y-axis).

4.2.4 Morphology and Chemical Composition

SEM images of the initial and heated Fe^{3+} doped brushite mineral are compared in Figure 4.4. As depicted in Figure 4.4a, a plate-like structure appeared in the unheated powder, the known structure of brushite mineral as reported in the literature [199]. The plate-like particles in the initial DCPD-Fe powder have nearly parallelogram shapes with sizes ranging from a few micrometres to <50 μm, which is close to the extent reported in a previous study [199]. From Figure 4.4b, it is evident that the morphology of DCPD-Fe mineral has transformed after heating at 1000°C in an inert atmosphere. The heated mineral has transformed into β-calcium

pyrophosphate (β-$Ca_2P_2O_7$) and exhibited some densification. This finding has confirmed the XRD data reported previously in Figure 4.2.

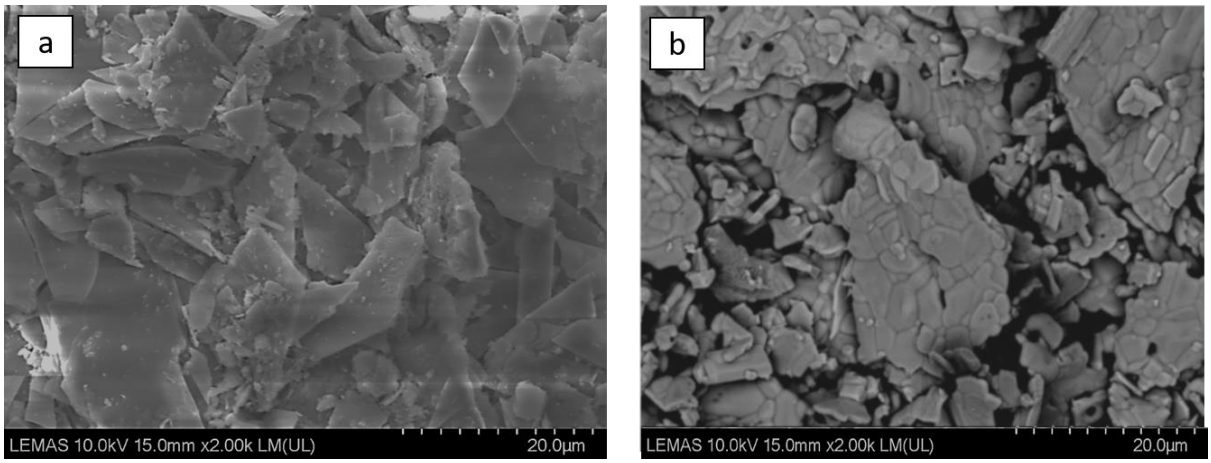

Figure 4.4: SEM images of unheated Fe^{+3} doped brushite powder (DCPD-Fe) (a) and the heated Fe^{+3} doped brushite powder (DCPD-Fe) at 1000^{o}C in the presence of argon for 2h (b).

4.3 Scaffolds Characterisation

The contribution between the scaffolds' composition (titanium with DCPD-Fe mineral) and the created porous structure is suggested to realise an optimum cortical scaffold, which manifests mechanical and biological properties comparable with natural bone. The following paragraphs will present and discuss the characterisation results of the designed scaffolds and investigate the features of the created porous structure.

4.3.1 Phase Composition and Crystal Structure

4.3.1.1 Analysis of Oxygen Content in the Metallic Titanium Scaffolds

Titanium used in the fabrication process is 99.7% purity, as mentioned in Chapter 3 (section 3.2 Materials Preparation). X-ray diffraction was used to analyse the crystal structure of titanium samples before and after heating. Figure 4.5a presents the experimental XRD patterns for the titanium pellets sintered in argon at temperatures ranging from 850 to 1150 ^{o}C for two hours. The titanium sample without sintering was examined at room temperature (25 ^{o}C) to use as reference. XRD patterns of all Ti pellets conform to the hcp structure of α-Ti according to the information reported in the database card (JCPDS 04-006-2824). This finding indicates no change in the crystal structure of titanium after the sintering process. The main 2θ^{o} are 35.22^{o}, 38.55^{o} and 40.29^{o}, corresponding to (1 0 0), (0 0 2) and (1 0 1) peaks, respectively. After heating, peaks were shifted to lower 2θ^{o} positions than the unheated sample (Table 4.1). For instance, the major peak (1 0 1) at 2θ^{o} ~ 40.29^{o} was shifted to 2θ^{o} ~ 40.05^{o}, 40.06^{o}, 40.08^{o} at 850, 1000 and 1150^{o}C, respectively (Figure 4.5b).

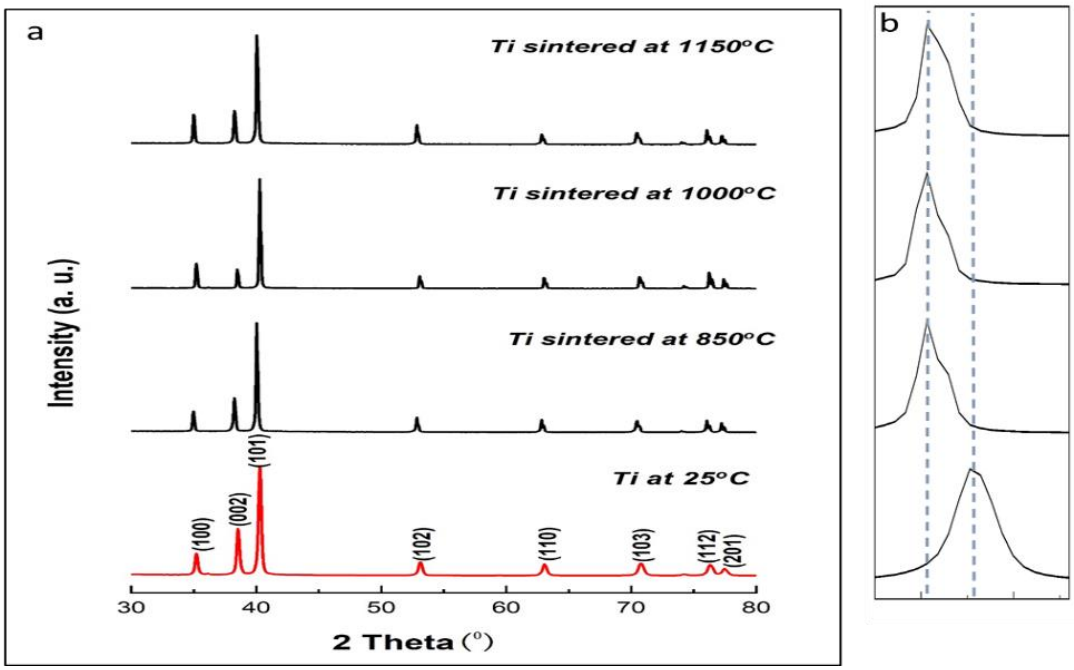

Figure 4.5: Normalised X-ray diffraction patterns for Ti pellets pre and post sintering in argon at various temperatures for 2h (a), the shifts in position of the prominent (1 0 1) peak after sintering at various temperatures at a constant time 2h (b).

The Bragg angles (2θ) and interplanar spacing (d) for pure titanium pellets sintered in argon at various temperatures for a constant time of two hours are given in Table 4.1. Interplanar distance (d) of Ti samples was calculated using the following formula of Bragg's law [263].

$$\lambda = 2\, d_{hkl}\, sin\, \theta \qquad (4.3)$$

$$d_{hkl} = \frac{\lambda}{2\, sin\, \theta} \qquad (4.4)$$

Where: λ is the X-ray beam wavelength (CuK_{α} = 1.5406 Å)

θ is the diffraction angle (degree)

d is the interplanar spacing (Å)

Table 4.1: Interplanar distance (d) with Brag angle (2θ) for pure titanium pellets pre and post sintering in argon at various temperatures for 2h.

Pure Ti 25 °C		Pure Ti 850 °C		Pure Ti 1000 °C		Pure Ti 1150 °C	
2θ°	d A°	2θ°	d A°	2θ°	d A°	2θ°	d A°
35.22	2.546	34.98	2.563	34.98	2.563	35.01	2.561
38.55	2.334	38.25	2.351	38.27	2.350	38.26	2.350
40.29	2.237	40.05	2.249	40.06	2.249	40.08	2.248
53.13	1.722	52.86	1.730	52.87	1.730	52.87	1.730
63.08	1.473	62.86	1.477	62.86	1.477	62.89	1.477
70.80	1.330	70.49	1.335	70.51	1.334	70.50	1.335
76.33	1.247	76.10	1.279	76.10	1.250	76.11	1.250
77.48	1.231	77.26	1.250	77.27	1.234	77.29	1.234

The changes in the lattice parameters of titanium pellets after the sintering process were investigated, as shown in Table 4.2. Lattice parameters of initial and heated Ti samples were calculated using the procedures given for the hexagonal structure [264].

$$\frac{1}{{d_{hkl}}^2} = \frac{4}{3}\left(\frac{h^2 + hk + k^2}{a^2}\right) + \frac{l^2}{c^2} \qquad (4.5)$$

Table 4.2: Lattice parameters and unit cell volume of Ti samples at various temperatures.

Sample	**a A°**	**c A°**	**Unit cell volume Vc A°³**
Pure Ti 25 °C	2.940	4.667	34.9342
Pure Ti 850 °C	2.959	4.700	35.6374
Pure Ti 1000 °C	2.959	4.701	35.6450
Pure Ti 1150 °C	2.959	4.702	35.6525

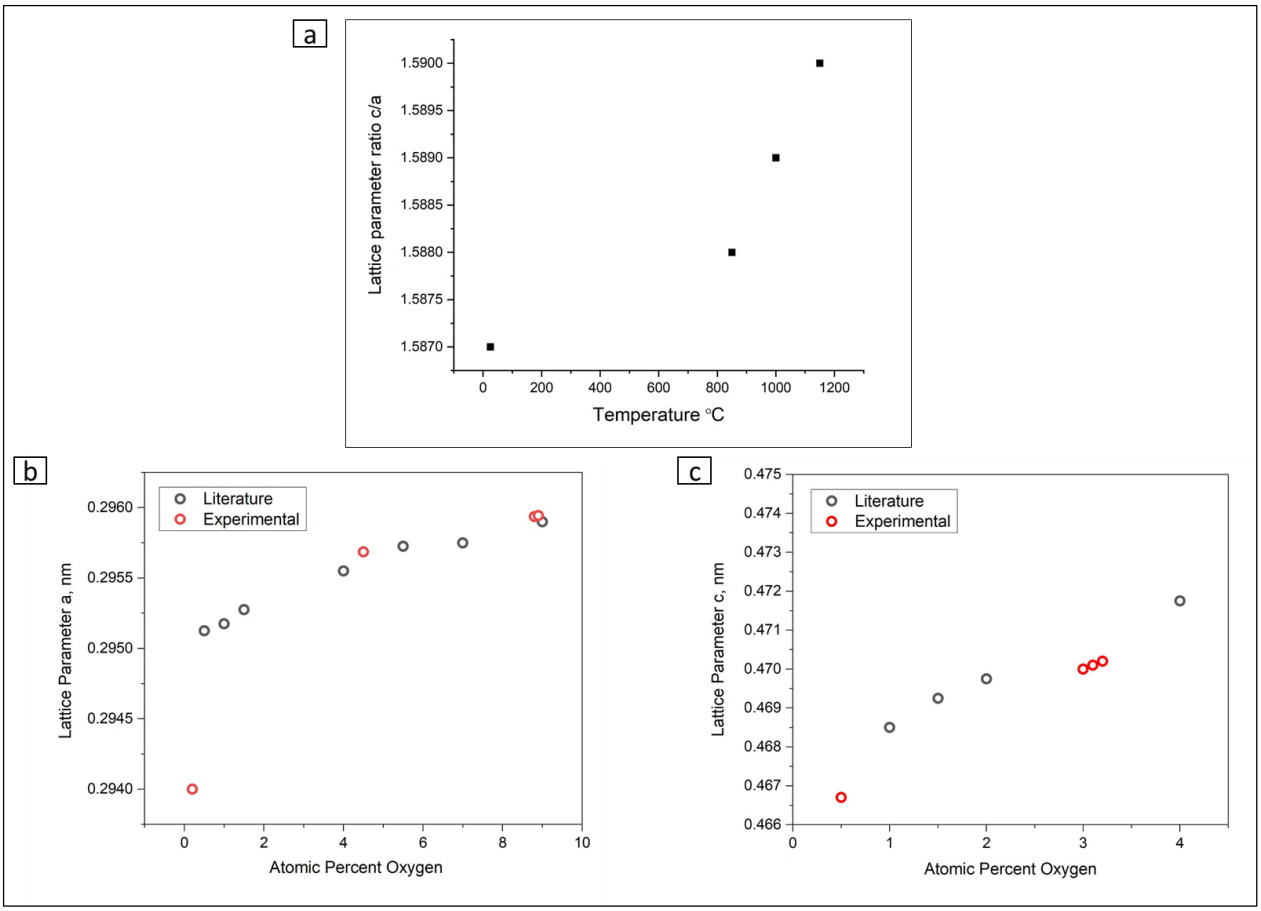

Figure 4.6: Lattice parameter ratio c/a as a function of sintering temperature of Ti samples (a), calculated lattice parameters a and c of Ti samples as a function of the atomic percent of oxygen (b & c); respectively.

By increasing temperature, 2θ peaks were shifted to lower values for all heated samples (Table 4.1). The lower 2θ was accompanied by an increase in the interplanar distance (d) for all Ti samples. For instance, after heating Ti to 1150 ^{o}C, 2θ of the prominent peak (1 0 1) shifted to a lower value from 40.29^{o} to 40.08^{o} with an increase in d spacing from 2.237 A^{o} to 2.248 A^{o}. The lattice parameters and unit cell volume of Ti samples before and after sintering were calculated as shown in Table 4.2. Then c/a ratio of Ti samples as a function of temperature ranging from 25 to 1150^{o}C was plotted in Figure 4.6a. The lattice parameter ratio c/a increased significantly after the sintering of titanium samples. Also, the unit-cell volume Vc increased with a higher temperature to become 35.6525 A^{o3} at 1150^{o}C compared to 34.9342 A^{o3} for the

initial Ti sample. The rise in the c/a ratio for all heated Ti samples is potentially due to the increase in the solid solution caused by the oxygen atoms in the structure of α-titanium [265]. The higher oxygen concentration after heating resulted in lattice stretching due to the existence of oxygen atoms as interstitial elements between the Ti lattices [266-269]. Figures 4.6b,c show the lattice parameters a and c of Ti samples as a function of the oxygen concentration based on our experimental values and literature data reported in [268, 270, 271] studies. An increase in the atomic percentage of oxygen from 0.5% to ~ 3 - 8% has been noticed, indicating the titanium structure has stored oxygen after sintering in the inert atmosphere.

4.3.1.2 Analysis of the Composite Material (Ti / 10%vol DCPD-Fe)

XRD diffraction pattern of the composite material (titanium with 10% vol Fe^{3+} dopped brushite) sintered in argon at 1000 ^{o}C for two hours is plotted in Figure 4.7a. The sample with a higher ratio of Cap (; 10% vol) is considered in order to investigate the influence of mineral addition to titanium more clearly. The dominant phase is hexagonal α-titanium (JCPDS 04-006-2824 card), which refers to no change in the crystal structure of titanium after reaction with the mineral. It can be seen that there is no shift in the Ti peaks of the composite material compared to pure heated Ti (Figure 4.5), indicating that there is no new solid solution or a significant amount of impurities in the titanium structure. The peaks associated with $2\theta^{o}$ ~ 37.09°, 41.36°, 44.55°, 46.30° are linked with β-pyrophosphate (β - $Ca_2P_2O_7$) (Figure 4.7b) with reference pattern (JCPDS-00-017-0499 card). This finding is consistent with the phase transformation curve in Figure 4.3; after heating Ti/DCPD-Fe sample at 1000˚C, γ to β transformation of DCPD-Fe is supposed to take place at 715˚C [128]. XRD pattern of the heated Ti/DCPD-Fe sample showed only peaks associated with the α-titanium phase and β-pyrophosphate phase. However, other secondary phases might be predictable based on the expected chemical reaction between titanium and iron-doped brushite, such as calcium titanate $CaTiO_3$ and iron-titanium alloy Fe-Ti [54]. These phases were not identified in XRD analysis,

which might be due to the lower temperature and duration time of sintering or the small amount of the DCPD-Fe mineral since 90%vol of the sample was titanium [272-277].

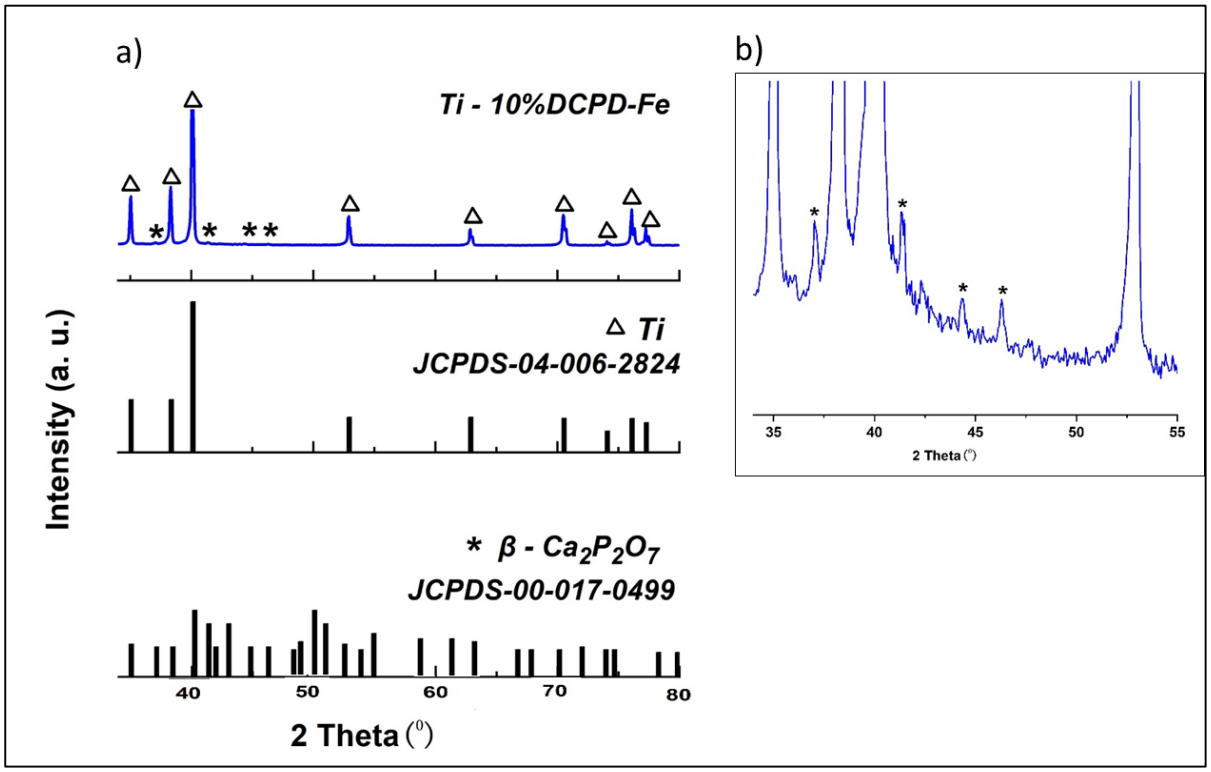

Figure 4.7: X-ray diffraction pattern of the composite material (Ti with 10% vol DCPD-Fe) after sintering in argon at 1000°C for 2h, with indexing to the JCPDS reference files of titanium Ti (Δ) and β-pyrophosphate β - $Ca_2P_2O_7$ (*) (a), magnified X-ray pattern showing the peaks linked to β-pyrophosphate phase (b).

4.3.2 Morphology and Chemical Composition of the Synthesised Scaffolds

SEM was utilised to examine the morphology of the synthesised scaffolds, and then the chemical composition was determined by EDX analysis. Figure 4.8 displays the morphology and phases distribution in the composite scaffolds after sintering in the inert atmosphere at 1000°C for 2h. Titanium with 5mol% and 10mol% Fe^{+3} doped brushite scaffolds are compared. Overall, the microstructure of the scaffolds was not well sintered with clear grain boundaries

[278]. The microstructure was dominated by titanium, and DCPD-Fe mineral was distributed between Ti grains with a higher quantity in a 10mol% scaffold.

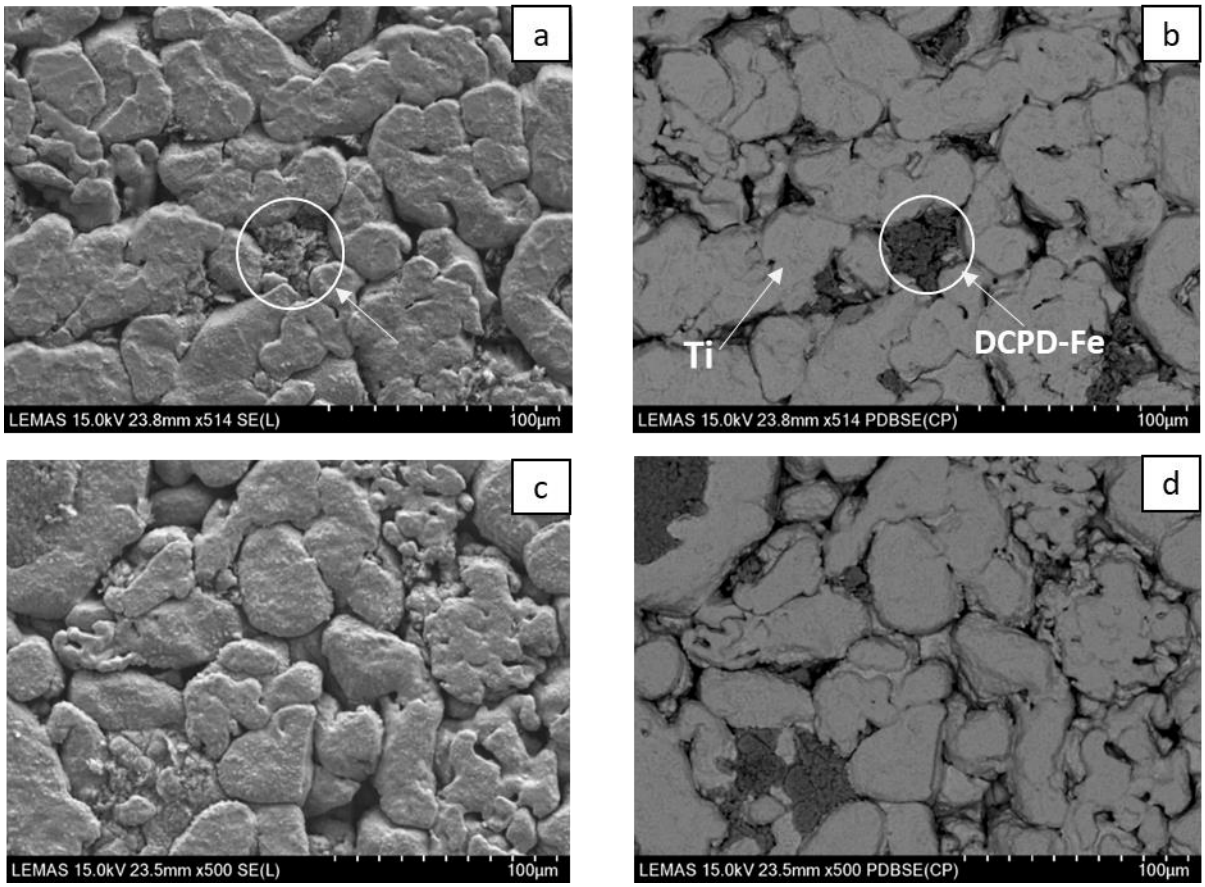

Figure 4.8: SEM micrographs of the composite scaffolds; titanium with 5mol% Fe^{+3} doped brushite (a & b), titanium with 10mol% Fe^{+3} doped brushite (c & d).

The SEM-EDX investigated the composition of the synthesised scaffolds. The elemental mapping of pure titanium samples sintered in argon (as shown in Figure 4.9) confirmed the XRD data and showed that the oxygen atoms distributed through the structure. In contrast, most titanium was oxidised in titanium samples sintered in the air, as displayed in (Appendix A). Figure 4.10 presents the elemental mapping of the composite scaffold (Ti/10 DCPD-Fe) that assured the distribution of DCPD-Fe mineral between titanium grains. The EDX analysis

of composite scaffolds was carried out at different locations. The overall EDX mapping demonstrates that the composite scaffold contains Titanium (Ti), Oxygen (O), Calcium (Ca), Phosphorus (P) and a minor amount of Iron (Fe). The oxygen was higher in the scaffold with 10vol% DCPD-Fe than the scaffold with only 5vol% DCPD-Fe. EDX confirmed the XRD analysis; there is no significant oxidation for titanium in the scaffold. EDX images presented the uniform distribution of Fe over the structure. In the interface area, Ti and P were detected, as shown in Figure 4.11. This finding suggests that phosphor diffusion into titanium particles occurred during the sintering process; this analysis was justified by Balbinotti study [279].

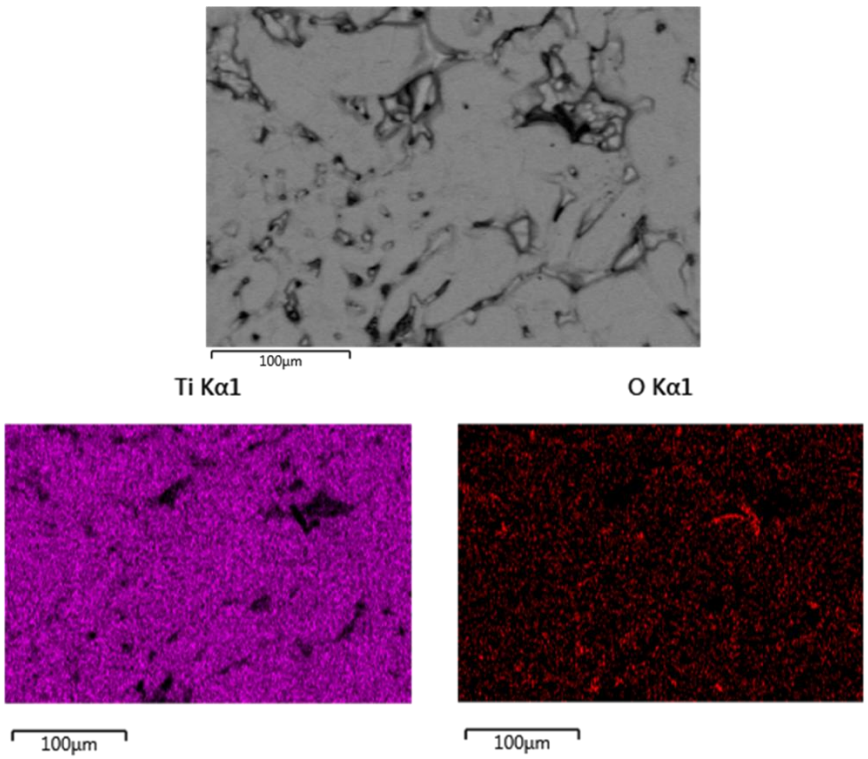

Figure 4.9: EDX mapping of pure titanium sample sintered in an inert atmosphere at 1000 ^{o}C for 2h.

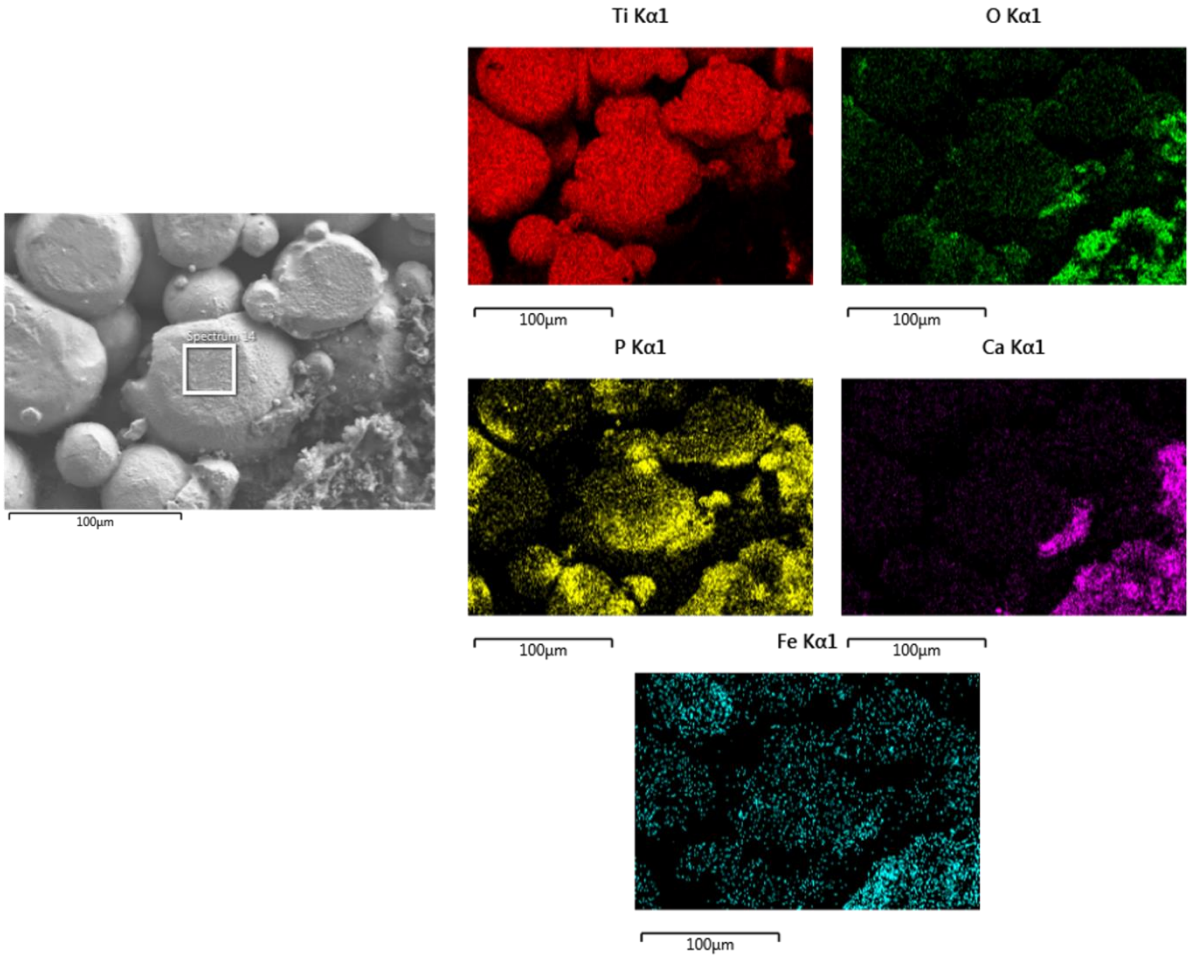

Figure 4.10: EDX mapping of titanium with 10mol% Fe^{+3} doped brushite illustrating the scaffold composition

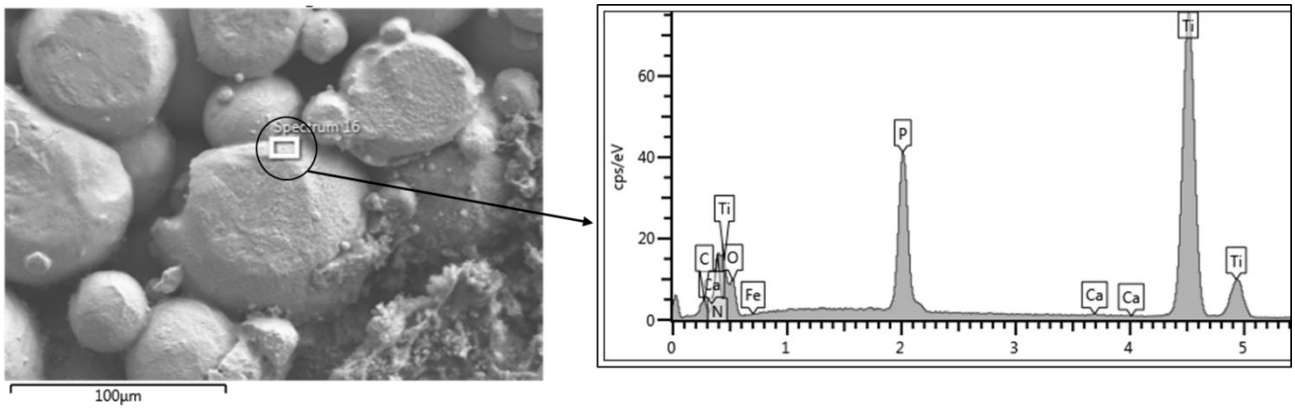

Figure 4.11: EDX analysis of the interface region containing phosphorus (P) in the composite scaffold (Ti/10 DCPD-Fe).

4.3.3 Surface Analysis

Surface analysis is essential to understand the interaction between the scaffold and the surrounding environment. The scaffold surface has a massive influence on cells response and activity due to the direct connection. X-ray photoelectron spectroscopy (XPS) was utilised to analyse the surface chemistry of the synthesised scaffolds, providing information about the elemental composition and chemical state. Binding Energy was calculated using the photoelectric effect equation (4.6).

$$E_b = hv - E_k \qquad (4.6)$$

Hence E_b is binding energy, hv is the X-ray photon energy (for Al Kα =1486.7eV), and E_k is kinetic energy.

Figure 4.12a is the XPS survey spectrum of the pure Ti sample, which shows strong peaks of titanium (Ti2p) and oxygen (O1s). According to the XPS Database, the high resolution fitting for the Ti 2p peak is presented in Figure 4.12b [280]. The Ti 2p spectrum shows symmetrically and splitting two peaks, Ti $2p_{3/2}$ and Ti $2p_{1/2}$. As can be seen, the Ti $2p_{1/2}$ peak at a binding energy of 464.2 eV is much broader and shorter than the Ti $2p_{3/2}$ peak at a binding energy of 458.5 eV. The two components at these binding energies are assigned to TiO_2 with a chemical state Ti (4+). This finding implies that titanium dioxide (TiO_2 rutile) existed on the top 5-10 nm layer of the surface of the Ti scaffold [221]. However, no peaks were associated with TiO_2 rutile in the XRD diffraction pattern, which means the oxide was present only on the surface of the scaffolds.

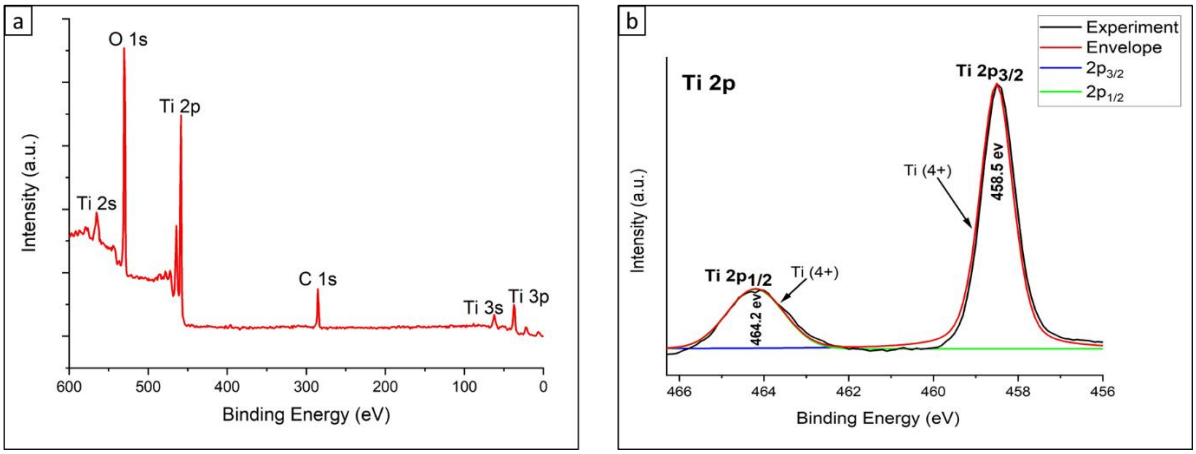

Figure 4.12: XPS survey spectrum for the surface of pure Ti sample (D=10mm) sintered in argon at 1000ºC for 2h (a), fitting for the titanium 2p peak after calibration via the carbon peak C1s at 285 eV (b), (n=3).

Figure 4.13a displays the XPS survey spectrum of the composite material Ti/10 DCPD-Fe. The constituents on the surface of the composite material are oxygen (O1s), titanium (Ti2p), calcium (Ca2p), phosphorus (P2s), carbon (C1s), and nitrogen (N1s). The relatively strong carbon peak (C1s) appeared due to surface contamination. A lower Ti 2p peak was on the composite material's surface compared to the pure Ti sample. The higher resolution spectrum of the Ti 2p (Figure 4.13b) was similar to that of pure Ti [281]. But, the two-component peaks of Ti 2p were located at a bit higher binding energies. The $2p_{1/2}$ and $2p_{3/2}$ peaks were located at binding energies of 464.5 eV and 458.8 eV, respectively. The high resolution fitting for the Ca 2p spectrum is relatively consistent (Figure 4.13c). The binding energy difference between Ca $2p_{1/2}$ and Ca $2p_{3/2}$ is 3.4 eV, and both 2p bands are symmetrical. Binding energy (347 eV) and width of the peak at half maximum (1.67) of $Ca2p_{3/2}$ indicate that the Ca2p peak is possibly linked to $CaTiO_3$ oxide [282]. Figure 4.14 presents the shift to the higher binding energy of Ti2p peaks in the composite material Ti/10DCPD-Fe compared to pure Ti. Also, the peaks became broader since the full width at half maximum FWHM of $Ti2p_{3/2}$ was ~ 1.21 compared

to ~ 0.94 in the pure Ti surface. These findings are inherent in calcium titanate $CaTiO_3$. Calcium titanate $CaTiO_3$ was used in previous works as a coating for titanium scaffolds because of its biocompatibility, improvement of apatite bonding, as well as enhancement of cell attachment and proliferation [283-288]. $CaTiO_3$ demonstrated the ability to provide the opposite surface charges with phosphate ions in a simulated body fluid (SBF), supporting growing bone-like apatite [289].

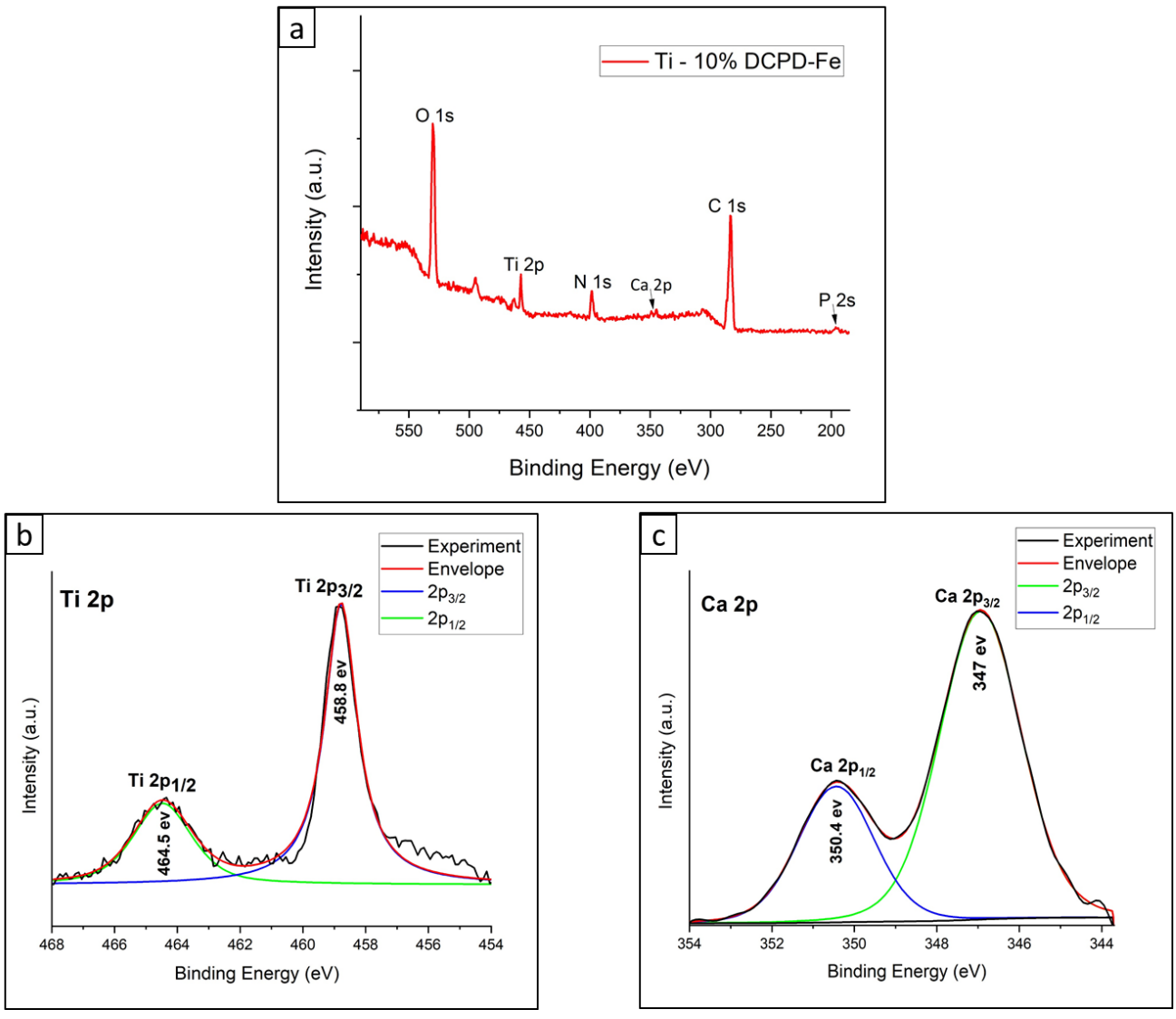

Figure 4.13: XPS spectrum for the surface of the composite material Ti-10 DCPD-Fe sintered in argon at 1000°C for 2h (a), fitting for the titanium 2p peak (b) and fitting for the calcium 2p peak (c), after calibration via the carbon peak C1s at 285 eV, (n=3).

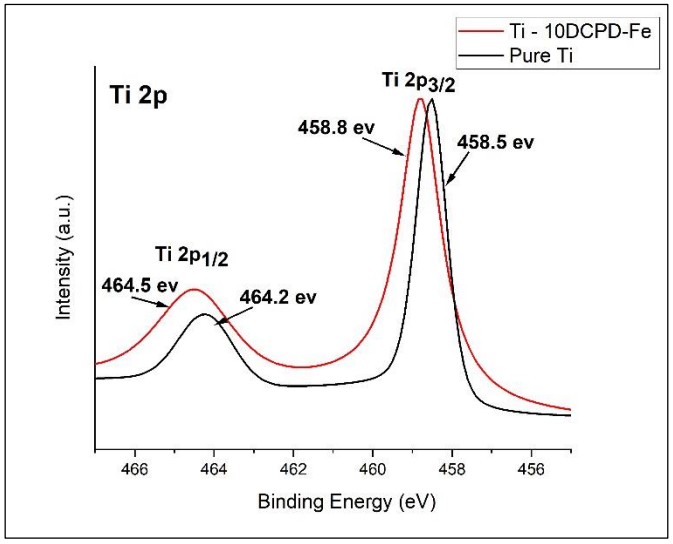

Figure 4.14: High-resolution spectra of Ti 2p on the surfaces of the pure Ti sample (in black) and the composite material Ti/10 DCPD-Fe (in red) after sintering in argon at 1000°C for 2h.

Table 4.3 presents the values of the binding energy BE and full width half maximum FWHM of O1s, C1s, $Ti2p_{3/2}$, $Ca2p_{3/2}$ and P2s for investigated pure Ti and composite material Ti/10 DCPD-Fe.

Table 4.3: The mean values of XPS fitting parameters for the prominent peaks of pure Ti and composite material Ti/10 DCPD-Fe, (n=3).

Element	Pure Ti		Ti/10 DCPD-Fe	
	BE [eV]	**FWHM [eV]**	**BE [eV]**	**FWHM [eV]**
O 1s	529.70	1.09	531.40	2.93
C 1s	285.00	1.15	285.00	2.95
$Ti2p_{3/2}$	458.50	0.94	458.80	1.21
$Ca2p_{3/2}$	-	-	347.00	1.67
P 2s	-	-	197.70	2.88

4.3.4 Porosity Characterisation

Following the compositional characterisation of the synthesised scaffolds, the findings of the structural characterisation will be presented here. The powder metallurgy with the space holding fabrication process resulted in highly porous scaffolds. An assessment of the porosity features of the resultant structures is vital to determine the scaffolds' efficiency in tissue engineering. These structural features significantly influence the mechanical properties and biological functionality of the synthesised scaffolds [290, 291]. Helium pycnometer, scanning electron microscopy, and micro-tomography were conducted to characterise the porosity of scaffolds. These techniques were utilised to investigate the feasibility of the scaffold's structure by exploring open porosity, average pore size and pores' interconnectivity.

4.3.4.1 Skeletal Density and Open Porosity of the Synthesised Scaffolds

The skeletal density and open porosity of the synthesised scaffolds were measured by the helium pycnometer technique. This method gives the most accurate porosity estimation due to the high diffusivity of helium and its ability to penetrate the smallest pores in structure [232, 233]. The skeletal density of scaffolds (ρ) is defined as the ratio of mass (M) to the measured skeletal volume ($V_{pycnometric}$), which is the volume of the solid material with closed pores.

$$\rho = \frac{M}{V\,\text{pycnometric}} \qquad (4.7)$$

The helium pycnometer technique can quantify only the open porosity accessible to the helium. The open porosity (P_{open}) is defined as the ratio of open pores volume (V_{pore}) to the total volume (V_{total}).

$$P_{open}(\%) = \frac{V\ \text{pore}}{V\ \text{total}} = \frac{V\ \text{total} - V\ \text{pycnometric}}{V\ \text{total}} \qquad (4.8)$$

Table 4.4 shows the apparent density, skeletal density and open porosity of the synthesised scaffolds. The apparent density of the synthesised scaffolds was measured based on the sample's mass and apparent volume. Then, skeletal density and open porosity estimation were performed using a helium pycnometer. The values were calculated following (4.7) and (4.8) formulas [168, 234, 292].

Pure titanium samples, referred to as (0,0), were tested to serve as a reference to compare it with the composite and porous samples. The pure titanium sample had a density of 4.39 g/cm^3 and open porosity of ~ 26%. The resultant density depended on the applied compaction pressure during the fabrication process, which affected the green density [293]. Sintering temperature also significantly influenced the final density and porosity due to the densification behaviour of solid powders during heating [293] since individual powders bond together during the sintering process through the solid-state diffusion [168].

Increasing the volume fraction of the space holder (KCl) raised the porosity and reduced the apparent density of scaffolds. Open porosity increased from 37.89% to 55.40% for samples (20,0) and (40,0), respectively, indicating that the space holder particles were removed after the immersion in heated water.

For solid composite samples (0,5) and (0,10), open porosity increased from ~ 27.97% to 29.41%, respectively, by increasing the ratio of DCPD-Fe mineral from 5 vol% to 10 vol%. A similar influence of DCPD-Fe mineral ratio on porosity was observed in samples (20, 0), (20, 5), and (20,10) since open porosity increased from 37.89% to 38.65%. This influence was more significant in higher porous samples (40, 0), (40, 5), and (40,10) as the open porosity increased from 55.40% to 60.00% by increasing the mineral ratio from 0 to 10 vol%. A possible

explanation for this observation is that small pores were formed between pressed and sintered particles of titanium and DCPD-Fe. That suggests some particles of the mineral phase was set between titanium particles, which lost the physical contact between titanium particles and led to higher porosity.

All the synthesised scaffolds have open porosity greater than 30vol%, which is promising for bone scaffolds. The optimal structure of bone scaffold must contain porosity in the range of 30 - 90 vol%, as reported in the literature [168]. However, the helium pycnometer method is limited and can measure only the open porosity accessible to the helium. Therefore, SEM and micro CT techniques will help complete the comprehensive analysis of the porous structure of the synthesized scaffolds [234, 294].

Table 4.4: The mean values of density and open porosity of the synthesised scaffolds (n=3).

Sample*	Designed scaffold		Apparent density (g/cm^3)	Skeletal density (g/cm^3)	Open porosity (%)
	KCl (vol%)	DCPD-Fe (vol%)			
(0,0)	0	0	3.25	4.39	25.96
(0,5)	0	5	3.09	4.29	27.97
(0,10)	0	10	3.00	4.25	29.41
(20,0)	20	0	2.72	4.38	37.89
(20,5)	20	5	2.60	4.20	38.09
(20,10)	20	10	2.54	4.14	38.65
(40,0)	40	0	1.94	4.35	55.40
(40,5)	40	5	1.88	4.30	56.28
(40,10)	40	10	1.68	4.20	60.00

*Samples named as following (KCl vol%, DCPD-Fe vol%), for example (20,5) means the sample containing 20vol% of KCl and 5vol% of DCPD-Fe.

4.3.4.2 Micro-structure of the Synthesised Scaffolds

Scanning electron microscopy examined the microstructure of the synthesised scaffolds sintered in an inert atmosphere. Figure 4.15 is the microstructure of the composite material Ti/5vol% DCPD-Fe, showing the tiny pores between Ti grains and DCPD-Fe particles. This finding confirms the helium pycnometer results when open porosity increased by a higher ratio of DCPD-Fe mineral. Figures 4.16a,b,c,d display SEM images of the porous titanium samples fabricated with two different percentages of the space holder KCl (20 vol% and 40 vol%). As can be observed, the space holding particles have been removed entirely after the leaching and sintering process. As visible, the surface roughness is relatively high, which is supposed to enhance osteoblasts' adhesion and differentiation. The pores are nearly spherical, and the size of solo pores is equivalent to KCl particle size. As can be observed in SEM images, large macropores characterised the architecture of scaffolds with an average size of 100 – 450 μm. In addition to the larger pores, smaller pores are formed between pressed and sintered particles (< 50 μm), providing an interconnection throughout the structure. The pores in the scaffold with only 20vol% KCl seem to be more self-isolated and closed. However, higher porosity affected the structure and resulted in a higher level of aggregation, leading to larger and more irregularly pores (600 – 850 μm). More pore clusters' aggregation increased the interconnectivity significantly in the 40%vol KCl scaffolds. However, pore interconnectivity also depends on the densification during the powder pressing and sintering process. This microstructure of the synthesised scaffolds is ideal for bone substitutes; hence, pore size must be large enough to enable cell migration, support the circulation of blood and nutrients, and eventually allow the penetration of new bone. As well, smaller pores can aid to develop an effective vascular network. In this respect, and according to the tissue engineering research, the ideal bone scaffold must have a pore size with a minimum of 50 – 100 μm to promote bone regeneration [20, 103, 176-178, 295, 296]. However, the mechanical properties will be

compromised if the scaffold has too large pores because of the void volume [20, 103, 176-178, 295, 296]. Pore interconnectivity is also essential for bone scaffolds as it facilitates cell seeding, penetration, and migration of osteoblast cells into the scaffold [20, 103, 176-178, 295, 296]. However, more accurate results regarding the interconnectivity of the pores were assessed by the micro CT technique.

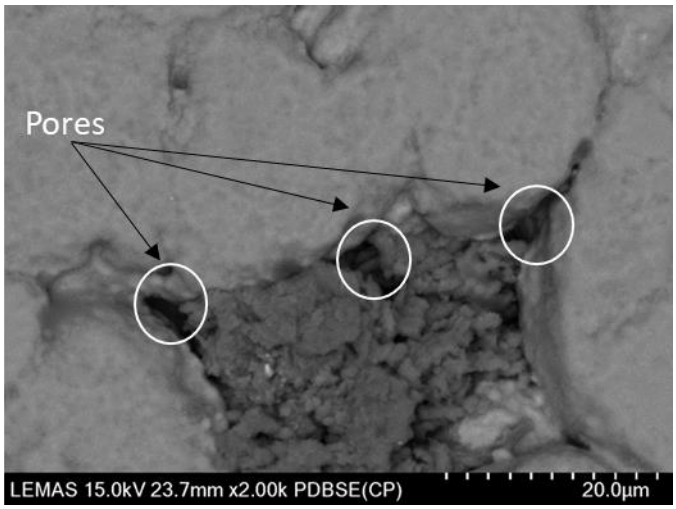

Figure 4.15: Magnified SEM image of Ti/5vol% DCPD-Fe showing the pores between titanium grains and mineral particles.

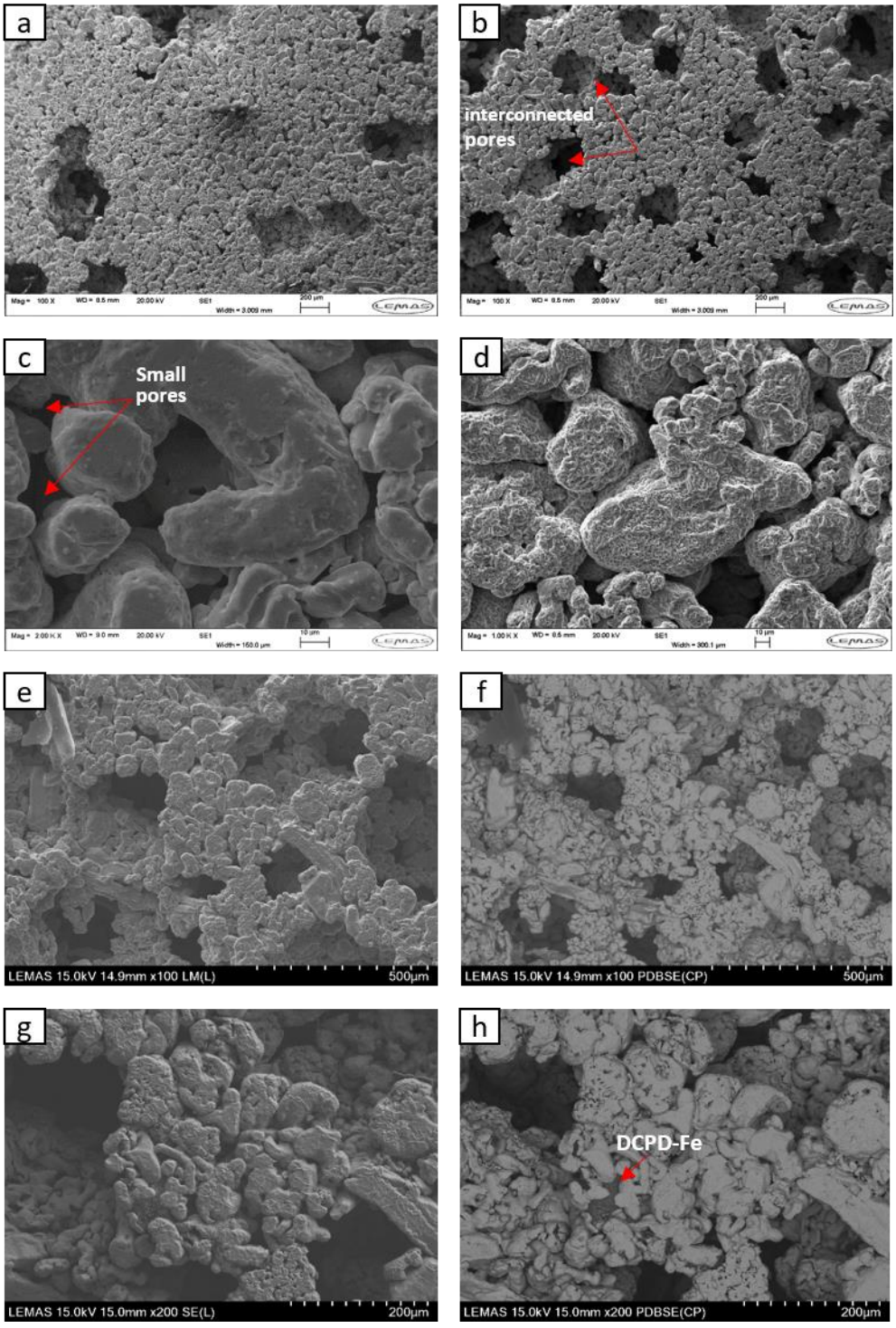

Figure 4.16: SEM images of the porous scaffolds showing the morphology, size, distribution and interconnectivity of pores; Ti scaffold with 20%vol KCl (20,0) (a & c), Ti scaffold with 40%vol KCl (40,0) (b & d) and porous composite scaffold containing 10%vol DCPD-Fe (40,10) (e, f, g, and h).

4.3.4.3 Distribution and Interconnectivity of Pores

The computed tomography (μ-CT) technique was used to investigate the distribution and interconnectivity of pores inside the structure of scaffolds. However, micro CT analysis is quite challenging for metal samples due to the attenuating X-rays. Hence the possibility of getting dark and bright grainy artefacts obscure some details in the scan images [290, 297]. The results are dependent on the applied algorithms and setups; thus, results are approximate with minor errors. The samples were characterised in different planes, and hundreds of cross-sections in three directions were recorded. Dragonfly software was then used to reconstruct the three-dimensional structure from these hundreds of cross-sections.

Figure 4.17 shows 2D and 3D μ-CT images of the porous titanium scaffold fabricated using 40%vol of KCl. Figure 4.17b corresponds to the sample's top view cross-section (x, y-direction). Figures 4.17c,d show the cross-sections of the side views (x, z-direction) and (y, z-direction). Pores (in black) are visible and distributed within the structure (in grey). As depicted in the top view, the spherical shape of the single pores is related to the shape of the initial space holder particles (KCl particles). The potassium chloride KCl crystals are entirely removed during the dissolution process, providing well-defined pores. The open pores are present from the surface through to the centre of the scaffold. Figure 4.18 displays the porous composite scaffolds Ti/10vol% DCPD-Fe; Figure 4.18a,b corresponds to the (40,10) scaffold fabricated with 40%vol KCl, whilst Figure 4.18c,d belongs to the (20,10) scaffold fabricated with only 20%vol KCl. The Dragonfly analysis showed that the total porosity was approximately 47% for the (20,10) scaffold and 65% for the (40,10) scaffold.

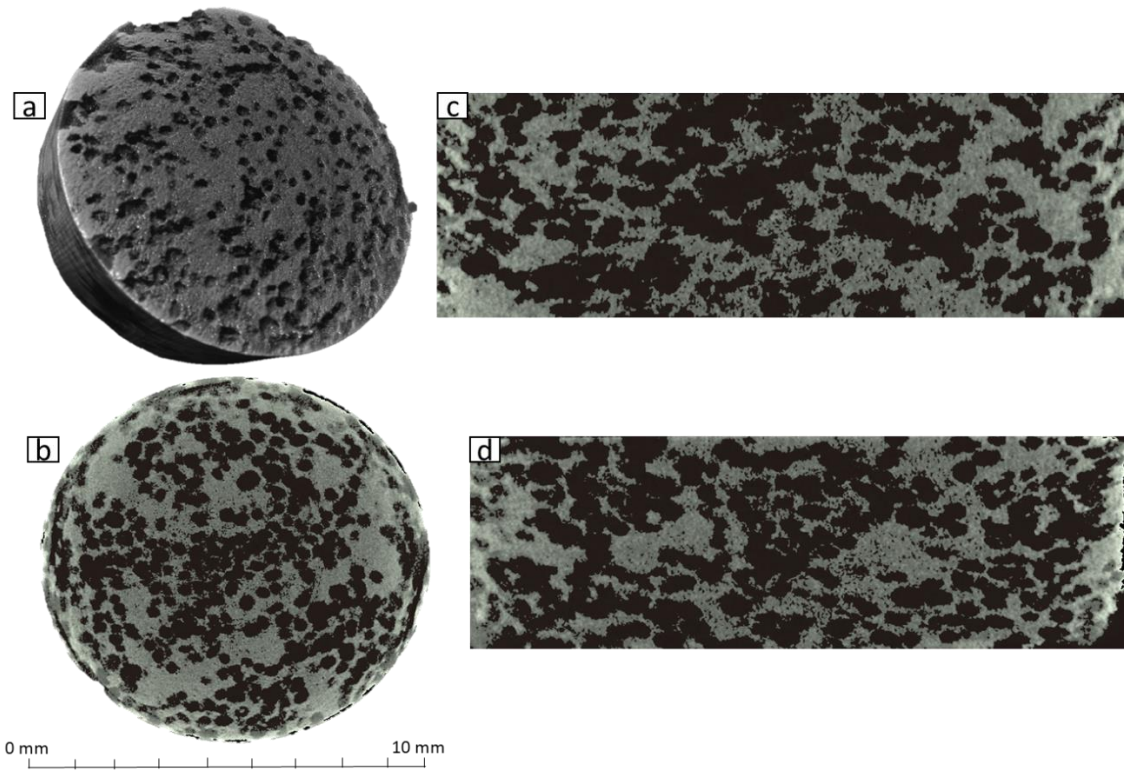

Figure 4.17: μ-CT images of the 40%vol KCl titanium scaffold (40,0); 3D image of the scaffold (a), top view cross-section (x, y-direction) (b), side view (x, z-direction) (c) and side view (y, z direction) (d); hence pores (in black) and the structure (in grey).

The pores inside the scaffold with higher porosity are mostly interconnected and accessible (~ 95%), as shown in green in Figure 4.18a,b, whilst very few pores are inaccessible, as illustrated in red. However, lower porosity and interconnectivity are presented in (20,10) scaffold, as shown in Figures 4.18c,d, since ~ 20% of pores are inaccessible. These findings are very close to the results obtained from the helium pycnometer method. An accessible porous structure indicates the potential of providing an excellent stable fixation with growing bone. Adequate biological fixation is a vital requirement to create a highly convoluted interface between the growing bone and the porous scaffold [167, 298-301]. The open and interconnected pores would facilitate the transport of nutrients and oxygen required during bone tissue growth [103,

302]. On the other hand, the broad pore size range (100 – 850 μm) should be sufficient to enable blood supply inside the scaffold. Literature also showed that a mean pore size greater than 300 μm facilitates cells proliferation [167, 298-301].

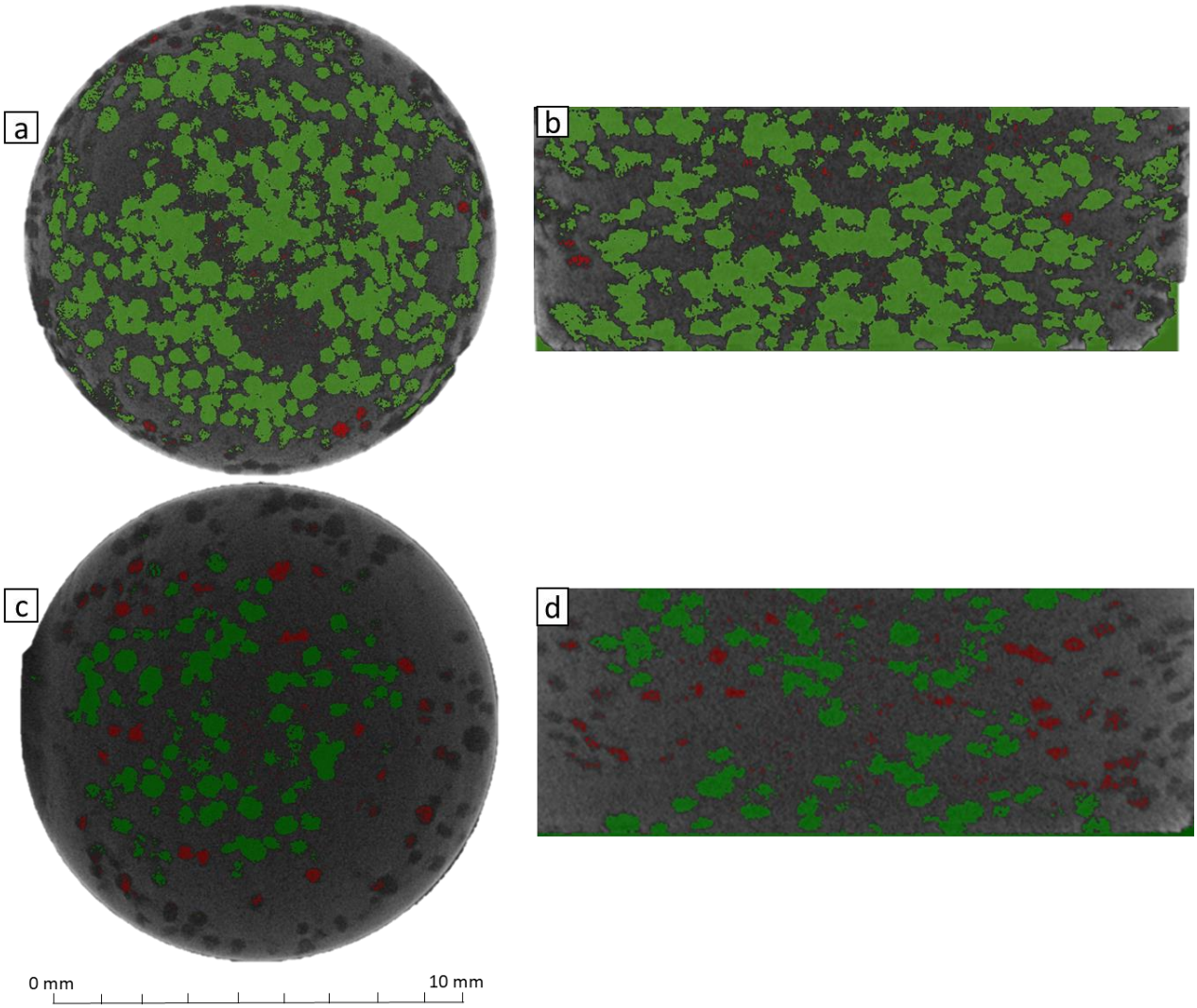

Figure 4.18: Cross sections showing the accessible pores in green and inaccessible pores in red for the porous composite scaffolds Ti/10vol% DCPD-Fe; (40,10) scaffold (a & b) and (20,10) scaffold (c & d).

4.4 Conclusion

This chapter presented the phase transformation and morphology of the synthesised mineral (DCPD-Fe). According to XRD results, no change in the crystal structure of all titanium scaffolds was observed. The calculated lattice parameters after the sintering process showed ~ 3-8% increase in the atomic percent of oxygen. XPS proved the presence of calcium titanate on the surface of the composite scaffolds, while TiO_2 existed on the surface of pure titanium scaffolds. The open porosity of the synthesised scaffolds ranged between 26 – 60%. Pore size was distributed between large pores 100 – 850 μm and small pores < 50 μm. Pores were ~95% interconnected and accessible in the scaffold (40,10).

Chapter 5

Mechanical Behaviour of Synthesised Scaffolds

5.1 Introduction

This chapter studied the mechanical properties of the synthesised scaffolds as a function of fabrication parameters. Three different synthesis variables, porosity, CaP ratio and sintering temperature, were considered in the study. The effect of oxygen content on the mechanical behaviour of the synthesised scaffolds was also discussed. Then, finite element analysis was included to determine the stress and strain distribution through the scaffolds.

5.2 Optimisation of Mechanical Properties

The Box-Behnken design along with the mechanical properties of the synthesised scaffolds sintered in an inert atmosphere are shown in Table 5.1.

Table 5.1: The mean values of mechanical properties of the synthesised scaffolds (n=3).

Variables			**Responses**		
Temperature [°C]	**KCl [vol%]**	**CaP [vol%]**	**Young Modulus [GPa]**	**Yield Stress [MPa]**	**Ultimate Strength [MPa]**
850	0	5	20.80	300	600
850	20	0	10.75	82	200
850	20	10	10.50	68	72
850	40	5	3.30	14	50
1000	0	0	40.80	450	700
1000	0	10	29.00	400	600
1000	20	5	20.50	125	165
1000	40	0	10.00	45	140
1000	40	10	8.70	35	130
1150	0	5	30.50	435	650
1150	20	0	20.20	120	340
1150	20	10	20.17	105	165
1150	40	5	9.60	38	138

Figure 5.1 displays the variety in the failure behaviour between titanium scaffold (0,0) (Figure 5.1 a) and porous titanium scaffold (20,0) (Figure 5.1b).

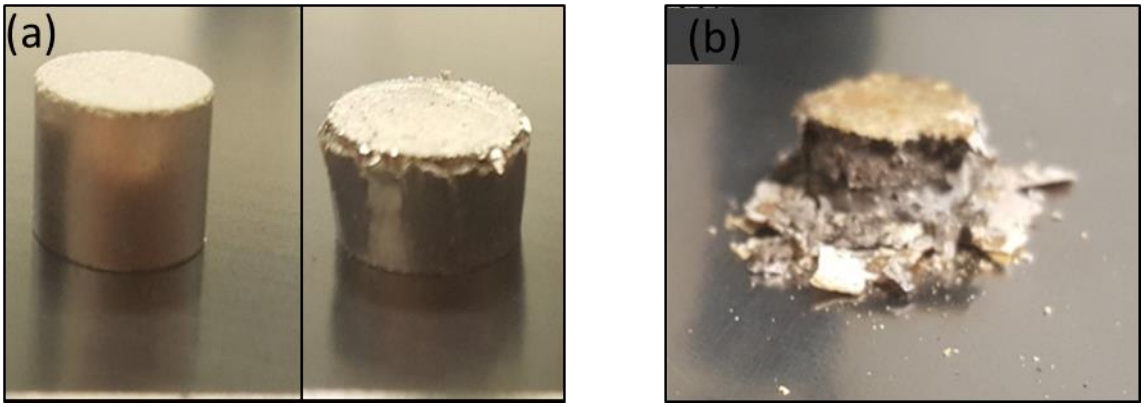

Figure 5.1: Some broken samples after uniaxial compression test; (a) titanium scaffold before (left) and after (right) testing, (b) porous titanium scaffold fabricated by 20%vol KCl and sintered at 1150^0C.

The theoretical models for the responses: Young modulus, compressive strength and yield stress are shown in Eq (5.1), (5.2) and (5.3), respectively. The models considered the effect of the synthesis variables and their interaction terms on the responses. The statistical analysis was done by implementing response surface methodology (RSM) using three factors Box-Behnken design (BBD). The regression equations were generated describing the change of Young modulus, compressive strength and yield stress against the alterations in synthesis parameters, including sintering temperature, porosity and CaP ratio. The experimental values of the mechanical properties (responses) were entered corresponding to the input synthesis parameters (variables) in the created design matrix [202, 205, 242].

$$\text{Young Modulus [GPa]} = -245.2 + 0.531A - 0.521B - 1.13C - 0.000248A^2 + 0.00284B^2 + 0.0196C^2 - 0.000283AB + 0.00007AC + 0.0263BC \quad (5.1)$$

$$\text{Compressive Strength [MPa]} = 321 + 0.49A - 37.00B - 11.6C - 0.000083A^2 + 0.4909B^2 + 1.245C^2 + 0.00317AB - 0.0157AC + 0.225BC \quad (5.2)$$

$$\text{Yield Stress [MPa]} = -955 + 2.248A - 7.73B + 7.7C - 0.000933A^2 + 0.2319B^2 - 0.410C^2 - 0.00925AB - 0.0003AC - 0.1500BC \quad (5.3)$$

Where; A, B and C are the variables of sintering temperature, porosity and CaP ratio, respectively. The R^2 values were ~ 98%, indicating that the models could not explain less than 2% variations. The adjusted determination coefficient (R^2 (adj) = 97.72%) was also able to confirm the significance of the models.

Then model reduction was applied by eliminating the insignificant terms to simplify the models and maximise the precision of predictions. The parameter $\alpha = 0.05$ was used as the threshold for statistical significance. The p-value was used to check the relevance of each term since all the terms with p-value > 0.05 were removed. The final reduced models of the mechanical properties are:

$$\text{Young Modulus [GPa]} = 0.3 + 0.0293A - 0.5594B \quad (5.4)$$

$$\text{Compressive Strength [Mpa]} = 380.0 + 0.3092A - 32.50B - 10.32C + 0.4857B^2 \quad (5.5)$$

$$\text{Yield Stress [Mpa]} = 176.3 + 0.1950A - 17.95B + 0.2375B^2 \quad (5.6)$$

Pareto charts and normal plots of the standardised effects are depicted in Figure 5.2, showing the influence of synthesis parameters on the mechanical properties. The Pareto chart shows the absolute values of the standardised effects from the most significant to the slightest. The reference line in the chart refers to the statistically significant effects. In the normal plot, the red square refers to the significant influence on response, while the blue circle has a nonsignificant impact.

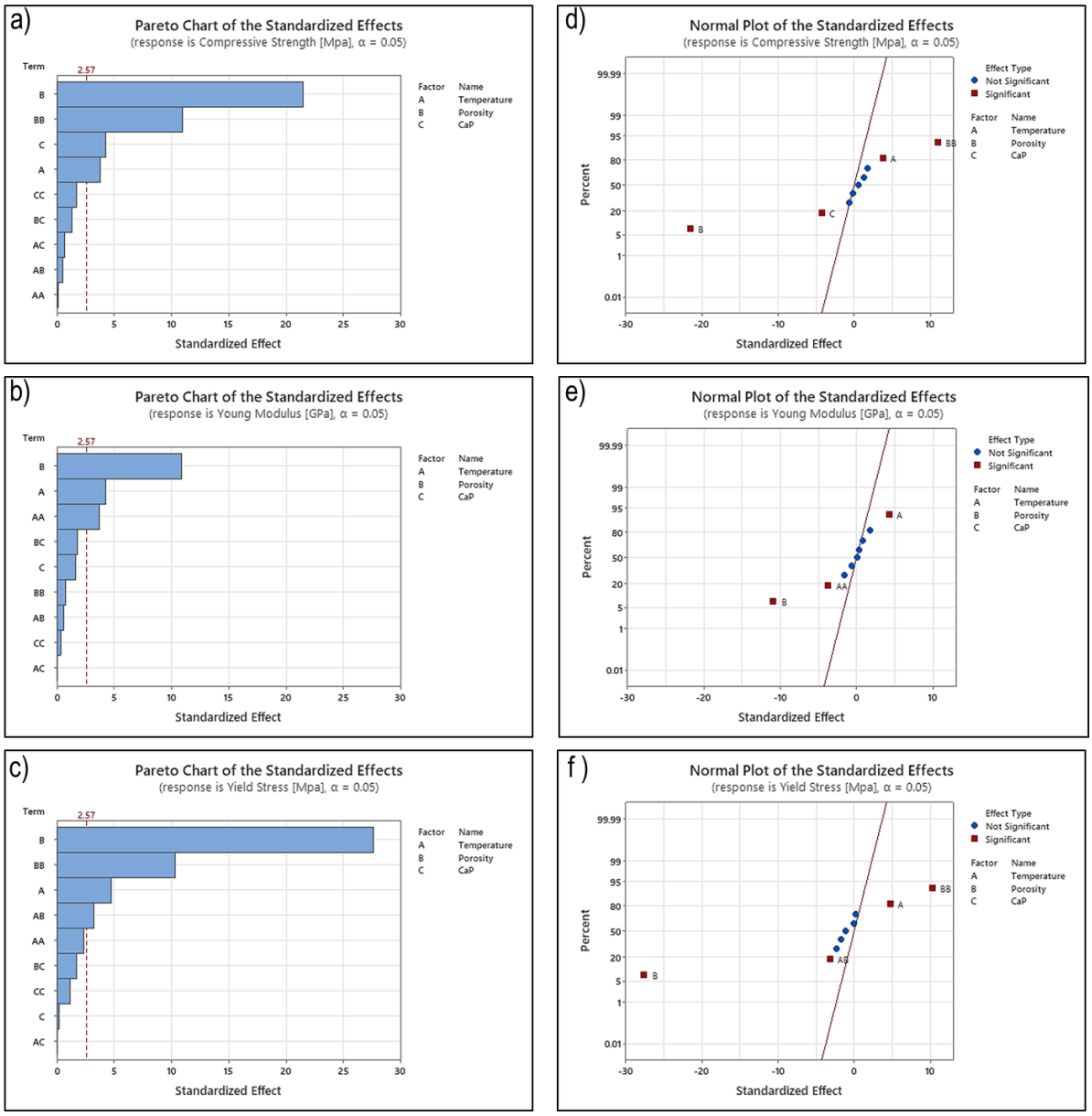

Figure 5.2: Pareto charts and normal plots of the standardised effects for the mechanical properties; pareto charts (a,b,c) and normal plots (d,e,f) of the standardised effects for the compressive strength, Young modulus, and yield stress, respectively; α=0.05

Based on these results, 2D contour plots for the mechanical properties are presented in Figure 5.3, considering the variables with the most significant impact.

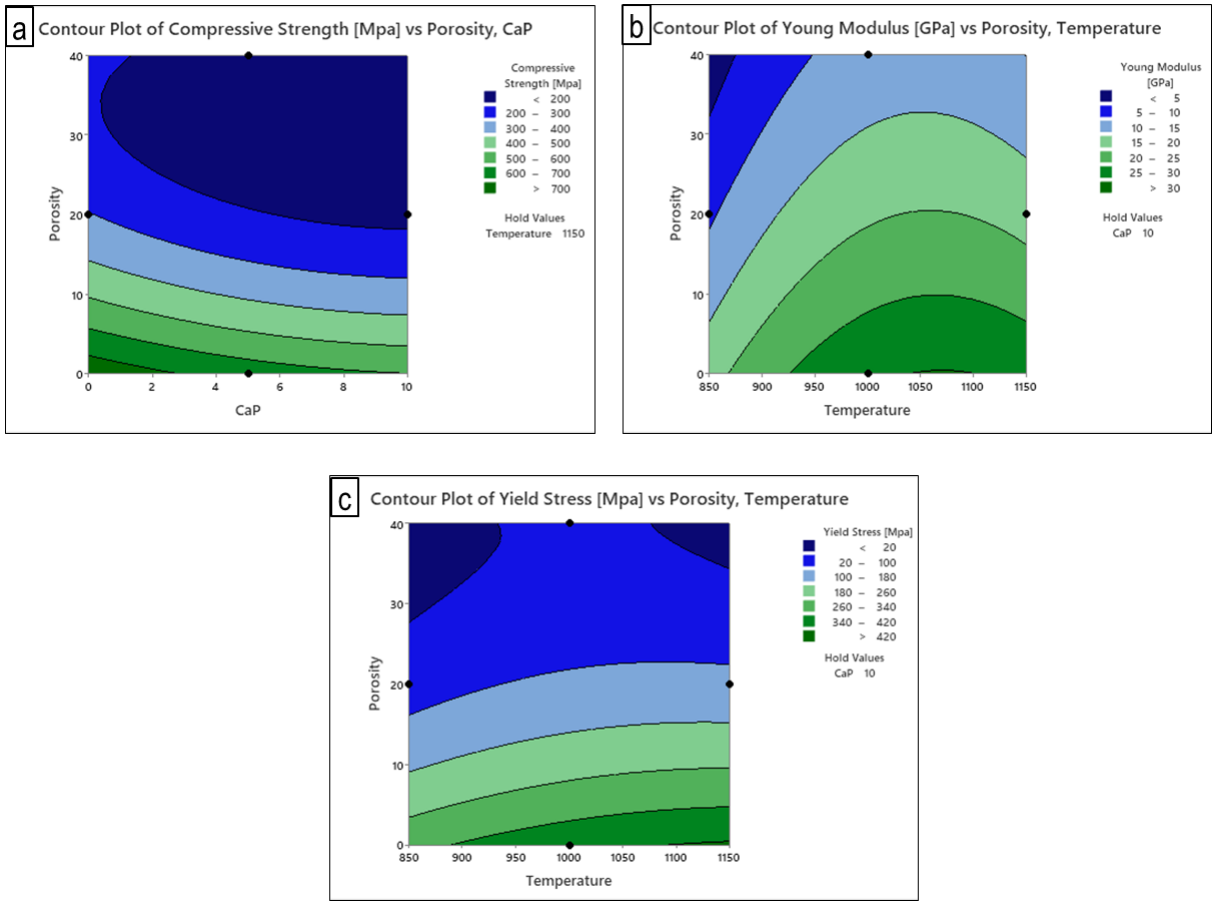

Figure 5.3: 2D contour plots showing the effect of porosity and CaP on compressive strength when the temperature is 1150^{o}C (a), and the effect of porosity and temperature on elastic modulus and yield stress when the CaP ratio is 10vol% (b and c).

The obtained results indicated that the rise in sintering temperature from 850 to 1150^{o}C resulted in an increase in elastic modulus, compressive strength and yield stress. Figure 5.3a illustrates the effect of porosity and CaP ratio on the compressive strength since porosity had a negative contribution, mainly when the KCl fraction was higher than 20%. Increasing the CaP ratio led to a remarkable reduction in the ultimate compressive strength; for example, the compressive

strength of the (20,0) and (20,10) scaffolds sintered at 1150^{o}C were 340 and 165 MPa, respectively. This finding indicated that increasing the CaP ratio from 0 to 10vol% for the scaffolds with the same designed porosity (20vol% KCl) and sintered at the same temperature decreased compressive strength to half value. Figures 5.3b,c show the effect of porosity and temperature on Young's modulus and yield stress, respectively. The porosity had a negative impact on both Young's modulus and yield stress [93]. However, the more decisive influence of porosity existed in the yield stress values. The elastic modulus values for the porous composite scaffolds ranged between 3.30 – 20.50 GPa based on porosity value, CaP ratio and sintering temperature. Young's modulus values for the porous composite scaffolds are comparable with that of the human femur bone (4 - 20 GPa) [243, 244, 303, 304], which indicates they are supposed to minimise the stress-shielding effect. Also, they exhibited suitable compressive strength ~ 130 - 165 MPa at sintering temperature 1000^{o}C or higher. These values are similar to data reported in the literature for compressive strength vs. age for the femur cortical bone ~ 90 - 180 MPa [243, 303, 305-307].

The fabrication using powder metallurgy with space holding technique greatly influenced the scaffolds' mechanical properties. As discussed in Chapter 4, mixing titanium with CaP mineral increased the porosity inside the pressed and sintered structure, resulting in lower density values, which eventually influences the mechanical integrity. As reported in the literature, the mechanical properties of porous materials depend strongly on microstructural characteristics such as pore shape, pore size, and connectivity [308]. High porosity increases the possibility of forming micro-cracks or defects in the structure, decreasing compressive strength. However, introducing pores into a scaffold structure either by the space holder KCl or the CaP particles can be beneficial in reducing the stiffness to match that of the surrounding bone. This finding

has been reported in previous studies on porous materials, revealing a decrease in elastic modulus with increasing total porosity [303].

Regarding sintering at high temperatures, it has been found that the mechanical properties of the synthesised scaffolds increased significantly due to high-temperature diffusion, which enhances the particles' bonding [293, 309]. According to XRD characterisation in Chapter 4, an increase in the c/a ratio with a higher sintering temperature was determined due to the higher oxygen content. The higher c/a ratio increases the strength of scaffolds due to the restricted number of slip planes in the hcp structure, as proven in previous studies [266, 268, 269, 293, 309-312].

5.3 Numerical Analysis

Numerical analysis was vital to accomplish the comprehensive understanding of the mechanical behaviour of the synthesised scaffolds. The study presented the stress and strain distribution along the damaged femur bone with the synthesised scaffolds. The scaffolds (20,10) and (40,10) were chosen to be studied in this analysis to investigate the stress and strain distribution. These two porous composite scaffolds showed interesting mechanical properties, with the best balance between stiffness and compressive strength and, consequently, ideal candidates for the use as cortical bone substitutes. Analysis of the femur bone with pure titanium scaffold (0,0) and bone graft using real properties of bone as displayed in Chapter 3 (Section 3.6.2: Materials Properties and Meshing) were also done. The analysis of these two scaffolds (0,0) and bone was considered as a reference to compare with in order to assess the mechanical behaviour of the porous composite scaffolds (20,10) and (40,10).

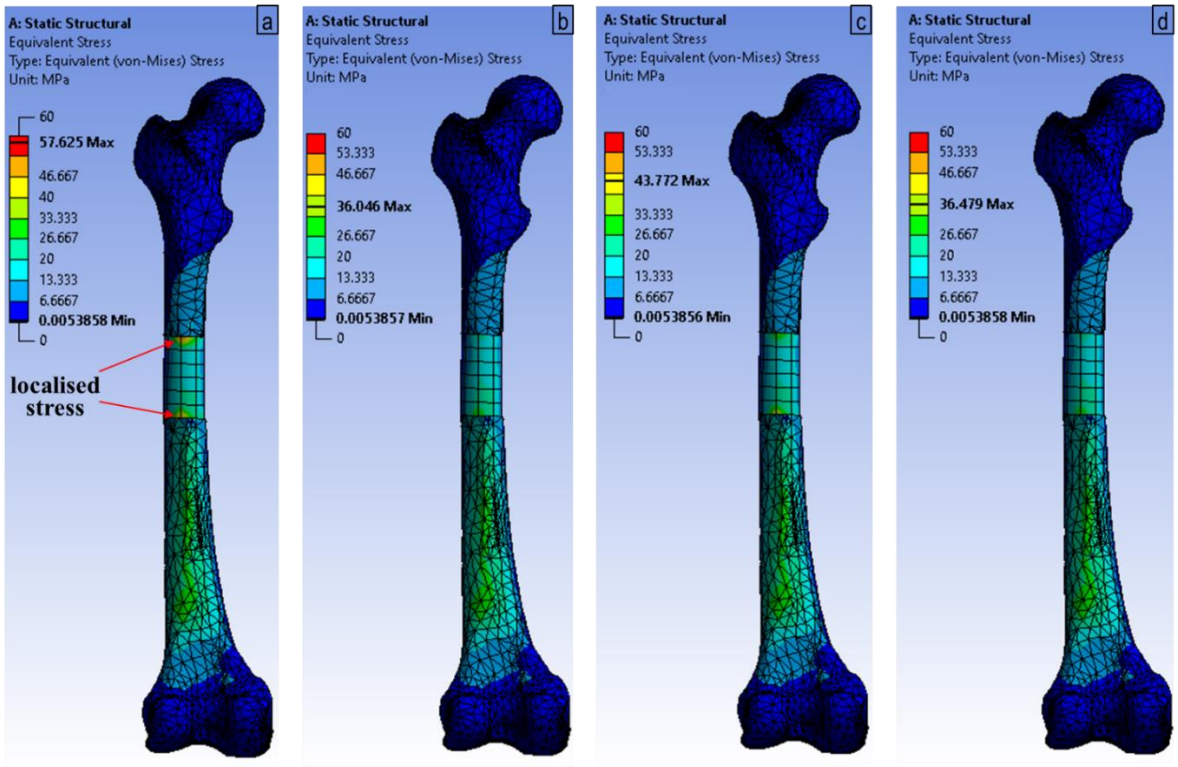

Figure 5.4: Equivalent von Mises stress of fractured femoral shaft with the scaffolds; titanium scaffold (0,0) (a), bone graft (b), (20,10) scaffold fabricated by 20%vol KCl & 10%vol CaP (c) and (40,10) scaffold fabricated by 40%vol KCl & 10% vol CaP (d). Colour coding ranges from low values in blue to higher values in red.

The equivalent von Mises stress obtained from the stress analysis of the femur bone with scaffolds during normal standing up is shown in Figure 5.4. The maximum stress for the titanium scaffold (0,0) was 57.62MPa which occurred on the contact surfaces between the scaffold and the femoral shaft (Figure 5.4a). The maximum stress for the model with the scaffold (20,10) fabricated using 20%vol KCl, and 10% vol CaP was 43.77MPa (Figure 5.4c), which also happened on the contact surfaces but with a lower value compared to the titanium scaffold. The results of scaffold (40,10) manufactured using 40%vol KCl and 10% vol CaP (Figure 5.4d) and the bone graft (Figure 5.4b) were very similar. The maximum stress value was ~ 36MPa distributed along the femoral shaft with the scaffold without stress concentration.

The equivalent elastic strain was also compared for the four models of the femur bone with scaffolds during normal standing up, as displayed in Figure 5.5. The strain distribution was along the femoral shaft, but the maximum value was closer to the distal part, which was fixed with the boundary conditions. By analysing the strain distribution through the four scaffolds, we can see that minor elastic strain was generated on the titanium scaffold (0,0) ~ 1.42e-4 % (Figure 5.5a). The strain distributions of the bone graft and (40,10) scaffold were similar, as shown in Figure 5.5b and Figure 5.5d, respectively. The strain occurred along these two scaffolds with maximum value on the contact area between the lower surface of the scaffolds and the femoral shaft. The elastic strain generated along the bone graft ranged between 0.24 – 0.61%, and for (40,10) scaffold was 0.18 – 0.56%. However, the elastic strain along the (20,10) scaffold was lower, with a range of 1.42e-4 – 0.12% (Figure 5.4c).

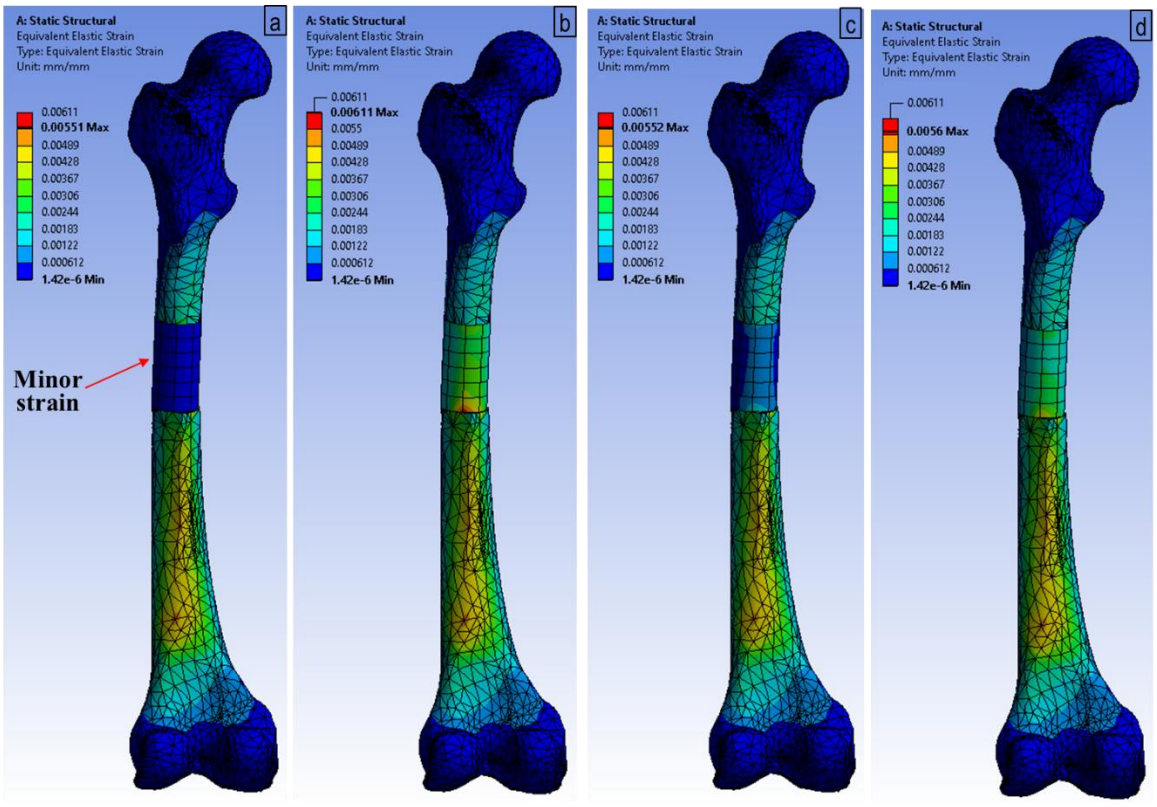

Figure 5.5: Equivalent elastic strain of fractured femoral shaft with the scaffolds; titanium scaffold (0,0) (a), bone graft (b), (20,10) scaffold (c) and (40,10) scaffold (d). Colour coding ranges from low values in blue to higher values in red.

Excessive stress with negligible strain was exhibited by the titanium scaffold (0,0), which was far away from the behaviour of the bone graft. The behaviour of titanium scaffold can be explained according to the simple mechanical rule in the composite system (femoral shaft and scaffold) since the stiffer component (titanium scaffold) withstood the greater load. That means the scaffold was overloaded, whereas the femoral shaft was unloaded due to the mismatch in stiffness. This finding indicates a high risk of stress shielding that can impair the scaffold's stability for long-term performance [54, 313, 314]. The bone tissue grows more in the loaded area while weaker in the unloaded areas containing less bone and more potential to fracture [244, 305, 306, 315, 316]. Better behaviour was exhibited by the synthesised scaffolds (20,10) and (40,10) since lower stress was generated, indicating better matching with the femoral shaft stiffness. Closer stiffness values to the natural bone were achieved by creating the porous composite structure of titanium with CaP. This result is supposed to help reduce the stress-shielding effect and peri-scaffold bone resorption [71, 185, 187-190]. On the other hand, the negligible strain in the titanium scaffold refers to improper scaffold-to-bone load transfer. In contrast, porous composite scaffolds (20,10) and (40,10) were able to generate interface scaffold-bone micromotions, which should support the osteointegration [48, 317-319]. The ability of the scaffolds to respond to the mechanical loading and deform is supposed to significantly enhance bone ingrowth due to stimuli cells' response.

5.4 Conclusion

The mechanical properties of the synthesised scaffolds depended highly on the fabrication parameters. The high values of mechanical properties are attributed to the high sintering temperature and low values of mineral ratio and porosity level. The elastic modulus values for the porous composite scaffolds ranged between 3.30 – 20.50 GPa, which indicates they are supposed to minimise the stress-shielding effect. Also, they exhibited suitable compressive

strength ~ 130 - 165 MPa at sintering temperature 1000^{o}C or higher. The results of the numerical study showed that the porous composite scaffolds (20,10) and (40,10) exhibited lower stiffness values closer to that of natural bone, providing lower stress concentration and a good load transfer which should be beneficial to stimulate the formation of new bone.

Chapter 6

The Influence of Synthesised Scaffolds on Cellular Response

6.1 Introduction

The synthesised scaffolds were tested in vitro to investigate the influence of porosity and Fe^{+3} doped brushite on the biological performance of osteoblasts. The chapter started with biocompatibility testing to examine G292 cell line viability and growth. Qualitative and quantitative assessments for the attachment and proliferation of osteoblasts on the scaffolds' surfaces were also conducted using Fluorescence imaging and PicoGreen DNA assay. Later, characterisation for the composition and surface of the pure Ti and composite material Ti/10DCPD-Fe was undertaken to examine the changes after osteoblasts seeding.

6.2 Biocompatibility Analysis

Biocompatibility is an essential requirement for bone scaffolds; hence, contact and extract testing were performed on the synthesised scaffolds. Evaluation of biocompatibility was conducted *in vitro* using G292 osteoblasts to assess the viability and growth of the cells [320, 321].

6.2.1 Contact Cytotoxicity

The direct contact assay is a qualitative assessment of cytotoxicity via microscopic analysis to observe any changes in the morphology or number of cells. The synthesised scaffolds were cultured with 1×10^4 G292 osteoblast cells for 72 hours to achieve 80% confluency. Six groups of scaffolds (n=3 for each) presenting different porosity and mineral ratios were evaluated by qualitative observation, as illustrated in Figure 6.1(c, d, e, f, g, h). Microscopic imaging of the cells proliferated near all the scaffolds exhibited similar results in terms of morphology and attachment compared to the negative control (Figure 6.1a). The positive control consisting of 40% dimethyl sulfoxide (DMSO) resulted in a lack of cell growth due to cell lysis, as depicted in Figure 6.1b. The consistent morphology and number of osteoblast cells proliferated throughout all the zones near the scaffolds confirmed no cytotoxicity signs.

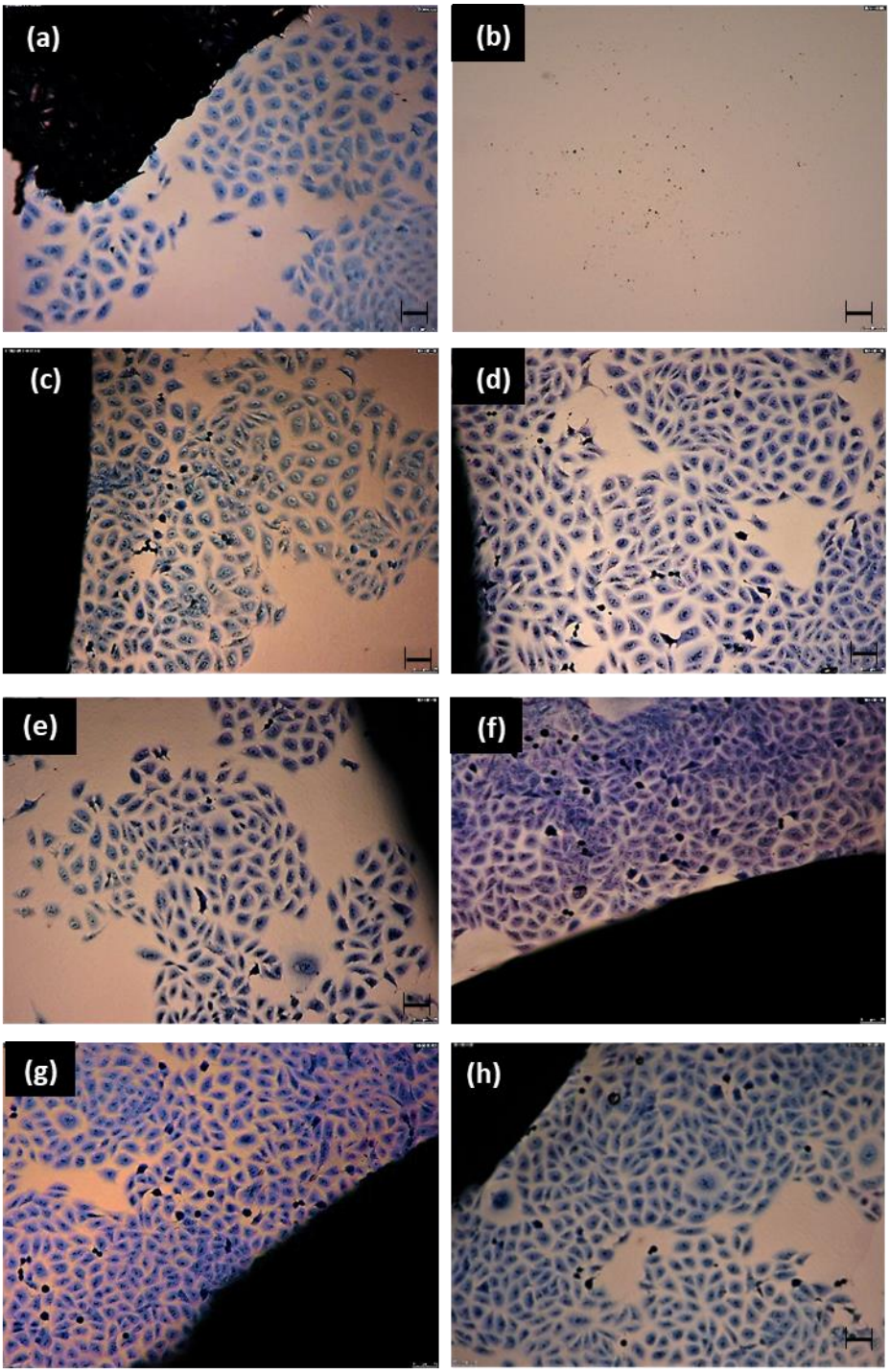

Figure 6.1: Brightfield illumination images of Giemsa stained cell cultures to determine contact cytotoxicity after 72h. Images show negative control (steir-stripe) (a), positive control (40% DMSO) (b) in comparison with pure Ti (0,0) (c), (0,10) scaffold (d), (20.0) scaffold (e), (20.10) scaffold (f), (40.0) scaffold (g) and (40.10) scaffold (h). (n=3) and scale bar: 75 μm

6.2.2 Extract Cytotoxicity

Extract cytotoxicity testing was vital to assess the potential toxic effects of released substances from the scaffolds on cells. Alamar Blue assay was followed to determine any changes in the oxidation-reduction range of the cellular metabolism [321, 322]. Negative control and positive control refer to the G292 cells incubated with the DMEM and 40% DMSO, respectively. The results showed the viability of the osteoblast cells on all scaffolds was equivalent to the negative control, as shown in Figure 6.2. There were no significant differences between any of the scaffolds and the negative control. The results showed a considerable reduction of Alamar Blue due to the growing osteoblast cells during the incubation with soluble extracts of scaffolds. While the positive control containing 40% DMSO exhibited dye oxidation that resulted from the significant cells growth inhibition [323, 324], as shown in Figure 6.2. Together these indicate that all scaffolds are biocompatible and support the growth of cells.

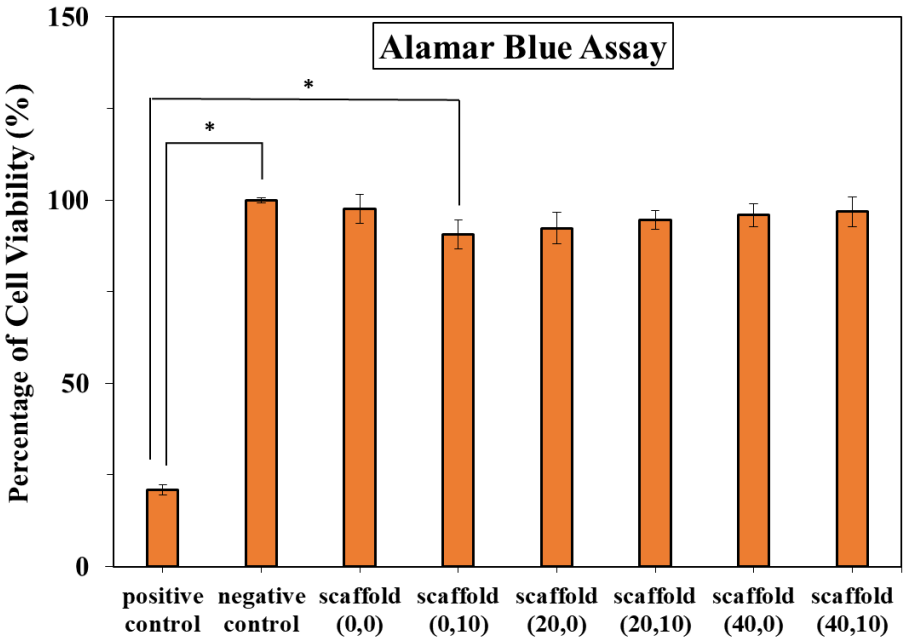

Figure 6.2: Cell viability evaluation for the synthesised scaffolds considering different porosity and mineral ratio levels. Negative and positive controls symbolise cells treated with media and 40% DMSO, respectively. Data represent the Mean ± SD, n=3, *$p < 0.05$.

6.3 Cell Attachment and Proliferation

Qualitative and quantitative assessments for the cell growth on the surface of the scaffolds were conducted in vitro using the G292 cell line. Fluorescence imaging and PicoGreen DNA assay examined the attachment and proliferation of osteoblasts on the scaffolds' surfaces.

6.3.1 Fluorescence Imaging

Cell adhesion and spreading on the scaffold surface are the initial interaction between the scaffold and cells that highly influence cells proliferation [325]. The osteoblasts are considered attachment-dependent cells; since they need to attach to the surface and spread to start proliferating. Therefore, it is essential to investigate the influence of the morphology and composition of the synthesised scaffolds on cell adhesion [326]. Qualitative analysis using confocal microscopy was conducted to assess the potential of the synthesised scaffolds to interact effectively with the osteoblast cells. The cytoskeleton of osteoblasts stained by Alexa Fluor 488 and DAPI are presented in Figure 6.3. Alexa Fluor 488 dye shows the cytoplasmic in green, and DAPI staining shows the nucleus in blue.

After incubation for three days, fluorescent imaging showed an excellent adhesion for intact and flat spread cells on all scaffolds' surfaces. The results showed that cells attached to the surfaces of (0,0) and (0,10) scaffolds, as depicted in Figures 6.3a,b indicating the excellent interaction between osteoblasts and the scaffolds' components (titanium and Fe^{+3} doped brushite). However, there is no apparent difference between the six groups of scaffolds. Therefore, quantitative analysis was required to investigate precisely the effect of the morphology and composition of the synthesised scaffolds on cell growth.

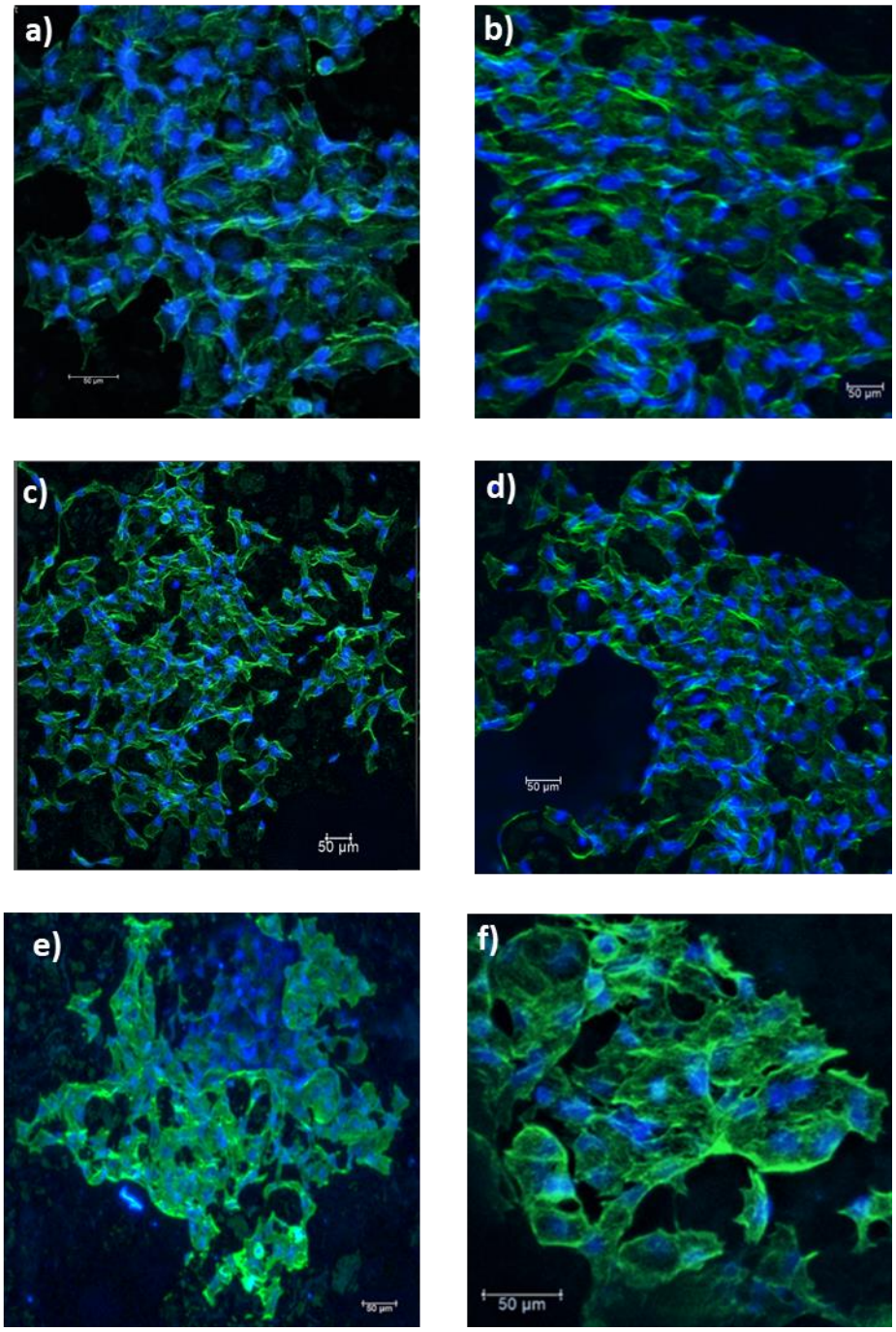

Figure 6.3: Confocal microscopy images visualising G292 cell line attachment on the synthesised scaffolds after incubation for 3days. (0,0) scaffold (a), (0,10) scaffold (b), (20,0) scaffold (c), (20,10) scaffold (d), (40,0) scaffold (e), and (40,10) scaffold (f). The green colour represents the actin cytoskeleton, and the blue colour represents the cell nucleus. Scale bar: 50 µm.

6.3.2 PicoGreen dsDNA

Quantitative testing was employed using the PicoGreen dsDNA assay to investigate the influence of the morphology and composition of the scaffolds on cell growth [326]. The number of cells was measured at predetermined periods (4 hours, 1 day, 3 days and 7 days). The purpose was to quantitatively determine which mineral ratio and porosity level offer the best cell attachment and proliferation.

Figure 6.4 compares the viable cell densities for the synthesised scaffolds after 4 hours,1 day, 3 days and 7 days of culture. More osteoblast densities were measured for all the synthesised scaffolds with increasing the cell culture time. Statistical analysis confirmed that the differences in cell densities were significant (P-value < 0.05) for all culture periods.

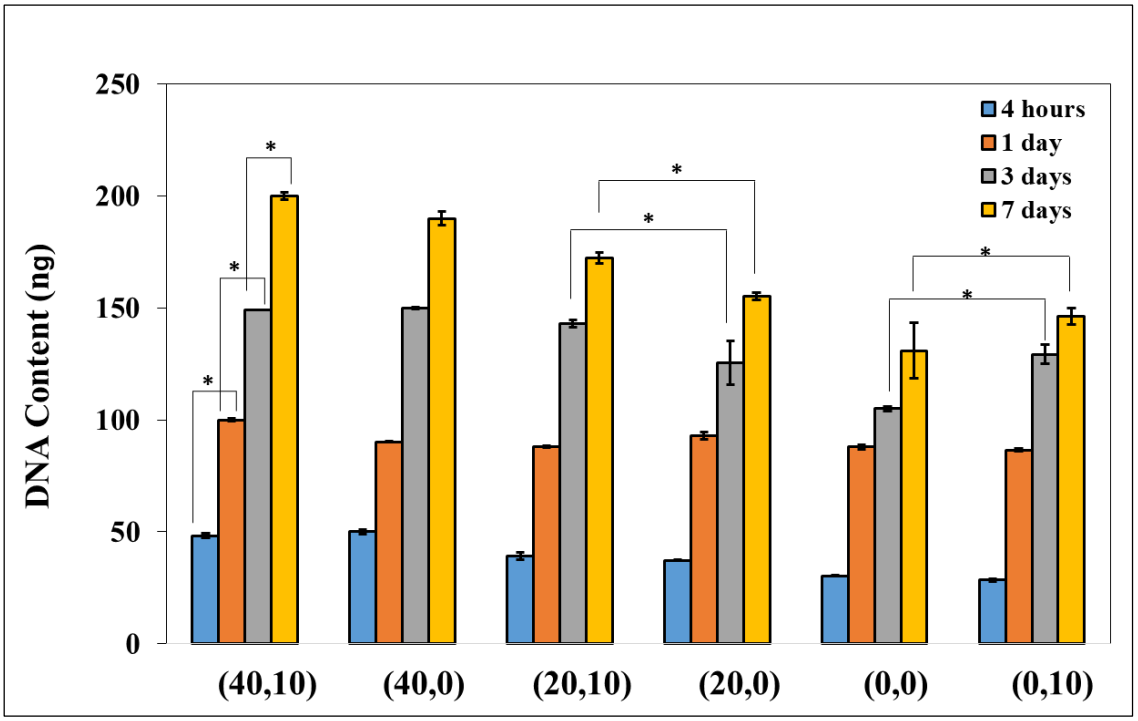

Figure 6.4: Osteoblast cell proliferation on the surface of the synthesised scaffolds evaluated using PicoGreen assay. Data represent the Mean ± SD, n=3, *p < 0.05.

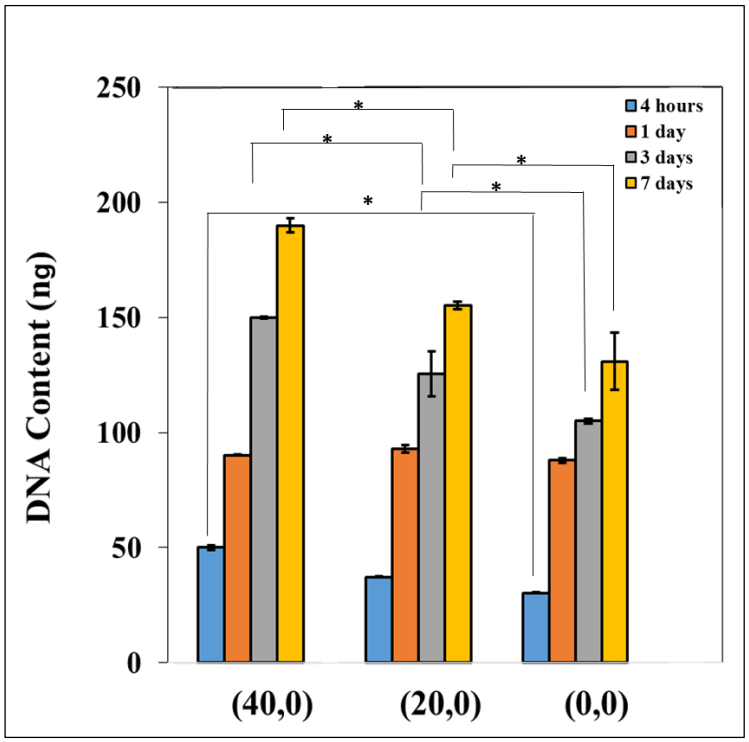

Figure 6.5: Osteoblast cell proliferation on the surface of the porous scaffolds (40,0) and (20,0) in comparison with the solid titanium scaffold (0,0). Data represent the Mean ± SD, n=3, *p < 0.05.

Figure 6.5 compares the viable cell densities for the porous scaffolds (20,0) and (40,0) with solid titanium (0,0) after 4 hours,1 day, 3 days and 7 days of culture. The results showed that after 7 days of incubation, cells proliferated more on the scaffold with higher porosity. Scaffold (40,0) presented a higher proliferation rate with ~ 18.3% compared to (20,0) sacaffold and ~ 31% compared to solid titanium (0,0) scaffold. According to Chapter 4 results, the average pore size of the fabricated porous scaffolds (40,0) and (20,0) ranged between 100 – 450 μm, and the size of interconnected pores was about 600 – 850 μm. This finding correlates with previous studies that reported porous bone scaffolds with an average pore size of 100 - 1500 μm facilitated excellent osteoblast cell attachment and proliferation [167, 298-301, 318, 325]. Whilst, too large pores > 1500 μm resulted in a decrease in the surface area, limiting cell attachment [298]. The configuration of porosity, interconnectivity and surface area of the synthesised porous scaffolds (40,0) and (20,0) were suitable for the cells to adhere and

proliferate. Literature demonstrated that cells prefered to agglomerate and attach as clusters in and near the pores in porous structures [302].

Figure 6.4 displayed that no considerable effect of the Fe^{+3} doped brushite (DCPD-Fe) mineral on cell proliferation after only 4 hours of incubation. However, the results after 3 and 7 days proved a higher number of cells on the surface of the composite scaffold (0,10) compared to (0,0). Scaffold (0,10) had a higher proliferation rate with ~ 19.2% after 3 days and ~ 10.5% after 7 days in comparison with pure titanium scaffold (0,0).

The porous composite scaffold (40,10) presented the positive influence of porosity and Fe^{+3} doped brushite mineral (DCPD-Fe) on osteoblasts proliferation after seven days of culture as shown in Figure 6.4. This finding is consistent with the literature showing better bone formation in CaP based scaffolds [103, 132].

6.4 Characterisation after Cell Seeding

In vitro experiments investigated the effect of the synthesised scaffolds on osteoblasts, considering the influence of composition and porosity of scaffolds. In order to inspect the interaction between the cells and scaffolds, characterisation for the pure titanium and composite material Ti/10DCPD-Fe was conducted after cell seeding.

XRD patterns of the pure Ti and composite material Ti/10DCPD-Fe after cell seeding for seven days are plotted in Figures 6.5 and 6.6. The XRD patterns of Ti and composite material before cell culture are also presented for comparison purposes.

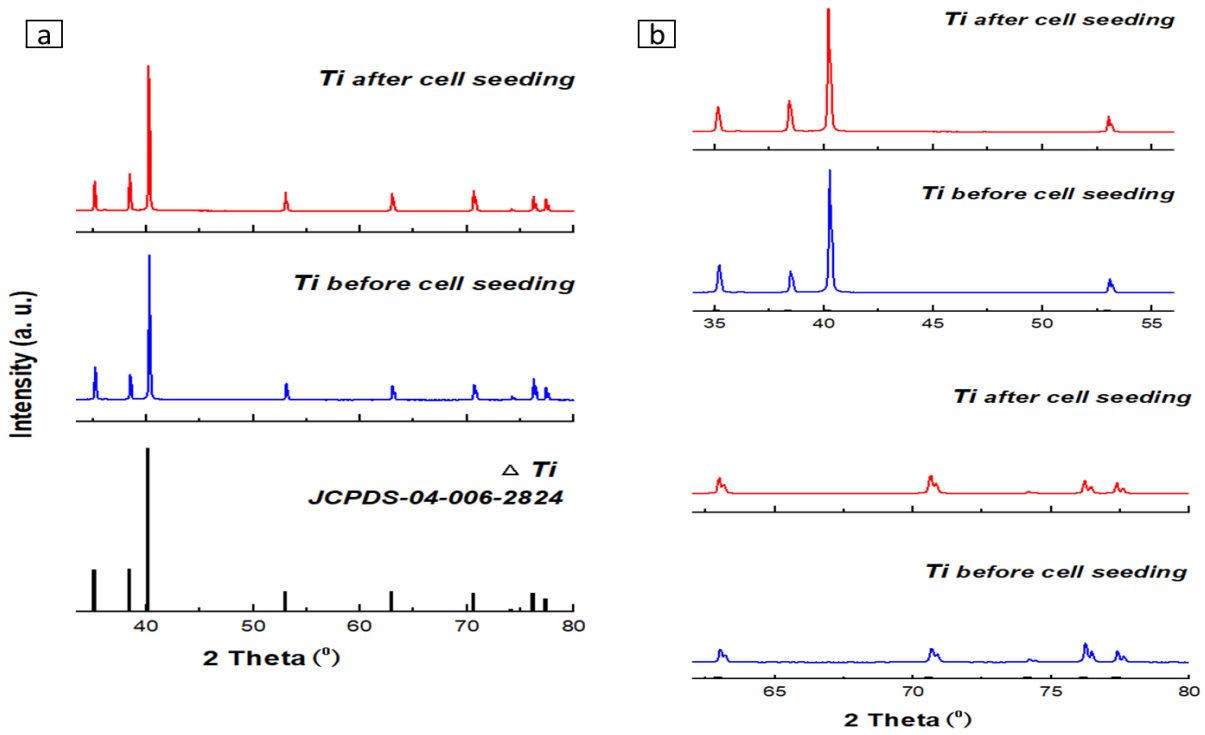

Figure 6.6: A comparison of X-ray diffraction patterns of Ti scaffolds before and after cell seeding for 7 days; with indexing to the JCPDS reference files of titanium Ti (Δ) (a), and the magnified scale of XRD patterns (b).

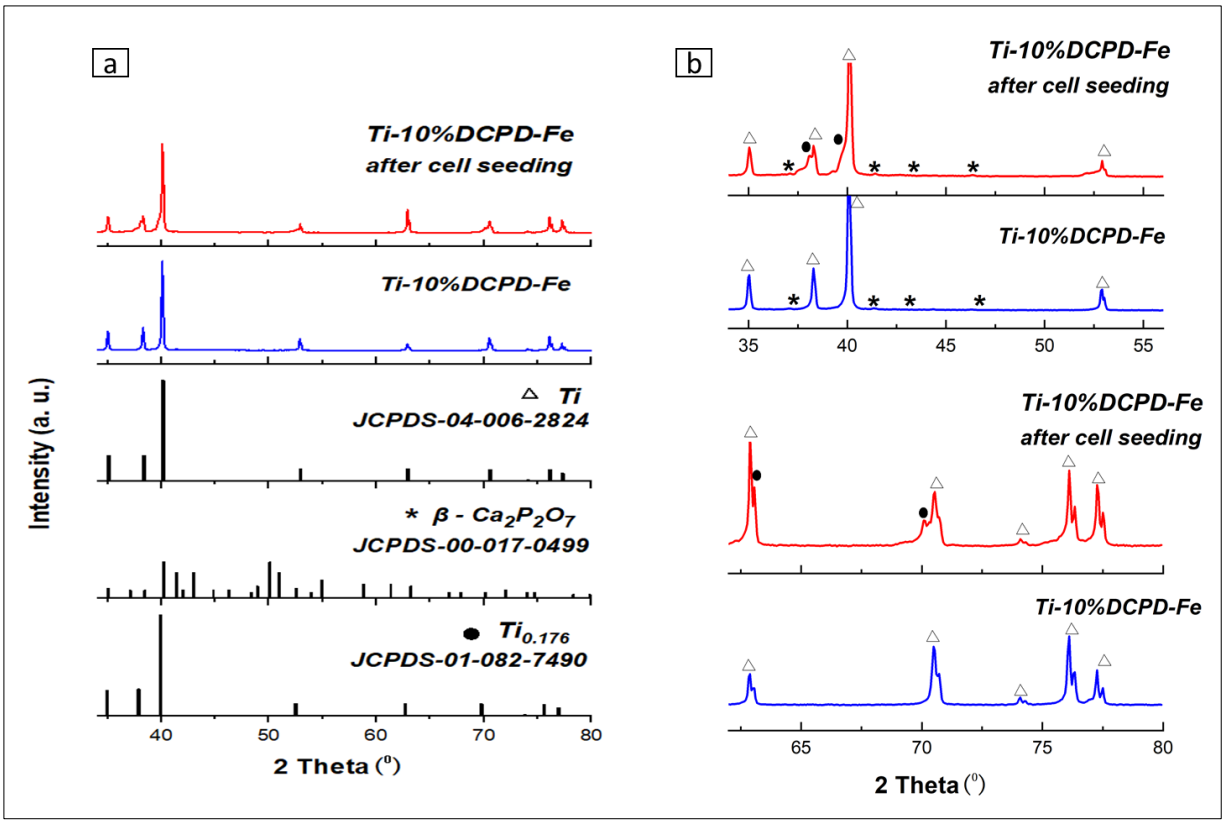

Figure 6.7: A comparison of X-ray diffraction patterns of the composite material Ti-10 % DCPD-Fe before and after cell seeding for 7 days; with indexing to the JCPDS reference files of titanium Ti (Δ), β-pyrophosphate β - $Ca_2P_2O_7$ (*), and $TiO_{0.176}$ (•) (a), and the magnified scale of XRD patterns (b).

There were no changes in the titanium scaffold after cell culture, and all peaks were linked with α-titanium (JCPDS 04-006-2824 card). The main identified phases of the composite material (titanium with 10%vol Fe^{3+} dopped brushite) after cell seeding were: α-titanium Ti (JCPDS 04-006-2824 card) and β-pyrophosphate β - $Ca_2P_2O_7$ with reference pattern (JCPDS-00-017-0499 card). The peaks associated with $2\theta^o$ ~ 37.76°, 39.83°, 62.95°, 69.55° were linked with titanium oxide $TiO_{0.176}$ (JCPDS 01-082-7490 card) [271, 277, 327]. The peaks corresponding to Titanium Oxide $TiO_{0.176}$ were not observed in the XRD pattern of the composite material before cell culture. This result indicated a higher oxygen concentration in the composite scaffold after cell seeding since $TiO_{0.176}$ contains ~ 15% atomic percent of oxygen. This finding

suggests that cells were growing on the surface of the composite material and provided oxygen to the scaffold. Whilst in pure titanium, no evidence of the presence of oxygenated titanium $TiO_{0.176}$ in the structure, which means the synthesised composite scaffold exhibited a better cell hosting environment. The dissolved oxygen in the composite scaffold would support cell growth and activity for longer-term. This may explain the higher cell proliferation on the surface of the composite scaffold compared to pure titanium after 3 and 7 days. However, to clarify this finding, the DNA quantification after a more extended period (> 7 days) would be helpful.

Surface analysis was also performed for the synthesised scaffolds after cell culture for seven days. Figure 6.7 displays the XPS survey spectra of the pure Ti and the composite material Ti/10DCPD-Fe before (in red) and after (in black) cell seeding. The most significant change on the surface of pure titanium after cell seeding was the lower intensity of the titanium (Ti 2p) peak. For the composite material, not only was a decrease in the intensity of titanium (Ti 2p) peak but also (Ca 2p) and (P 2s) peaks almost disappeared. The surface of both scaffolds, titanium and composite, showed more substantial peaks of oxygen (O 1s), nitrogen (N 1s) and carbon (C 1s) after cell seeding. XPS technique can penetrate only 5 – 10nm of the surface, which explains the decrease in intensity for the component peaks of the scaffolds. The more substantial peaks of oxygen, nitrogen and carbon on the surface of scaffolds after incubation with osteoblasts indicated to the growth of cells. Higher concentrations of oxygen, nitrogen and carbon gave a good sign of the biocompatible nature of the surfaces of scaffolds and the excellent interaction with cells. The results in Chapter 4 confirmed the formation of titanium dioxide TiO_2 and calcium titanate $CaTiO_3$ on the surface of the Ti and Ti/10DCPD-Fe scaffolds, respectively. According to literature, these oxides provide the scaffold's surface with

properties similar to those of natural bone, enhancing biocompatibility and increasing the bonding with cells [277, 284, 289, 328-330].

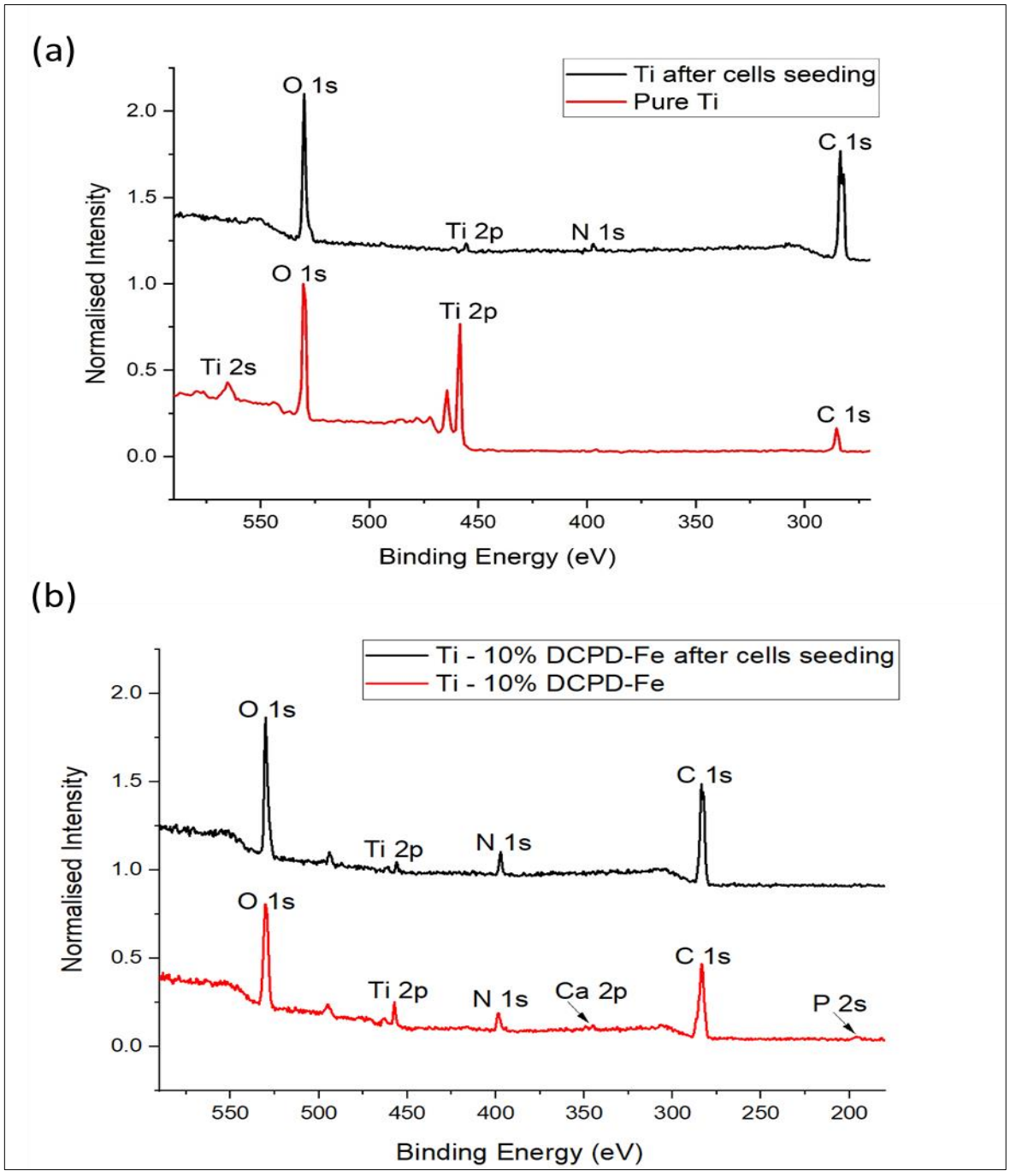

Figure 6.8: XPS survey spectra of (a): pure Ti and (b): composite material Ti/10DCPD-Fe before (in red) and after (in black) incubation with G292 cell for 7days.

SEM-EDX mapping of the composite material Ti/10DCPD-Fe, as shown in Figure 6.8, confirmed the XRD and XPS results. Higher concentrations of oxygen, nitrogen and carbon were detected on the surface of the scaffold, demonstrating the growth of osteoblasts.

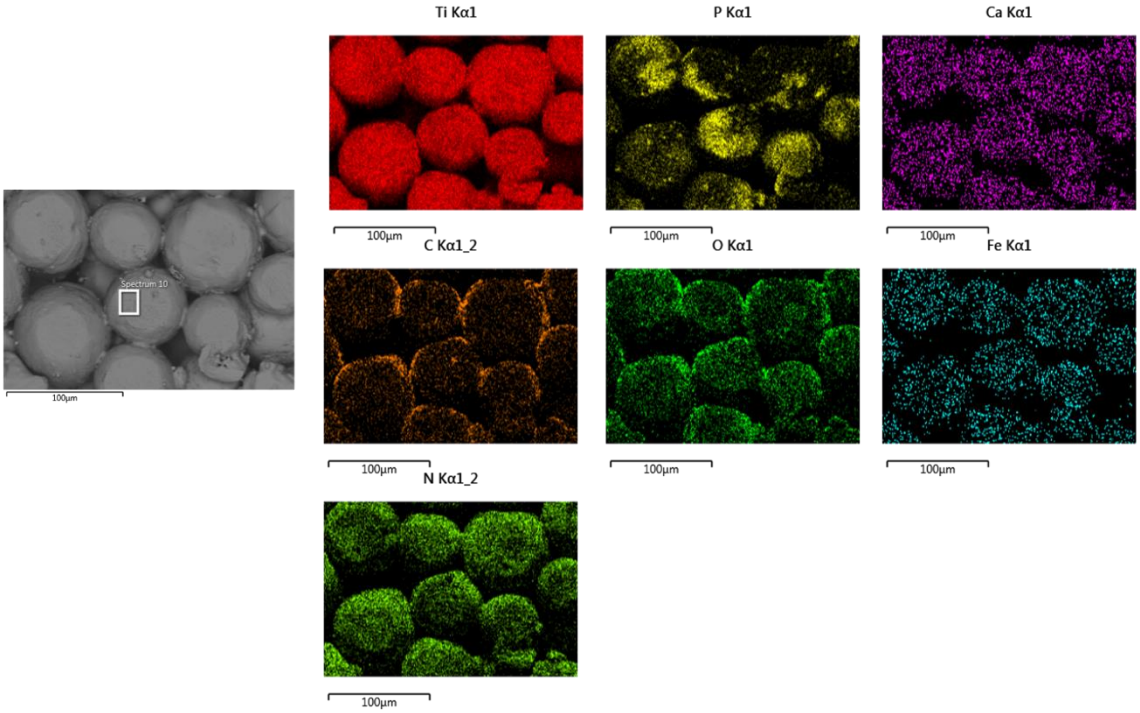

Figure 6.9: EDX mapping of titanium with 10vol% Fe^{+3} doped brushite illustrating the scaffold composition after cells seeding for 7 days.

6.5 Conclusion

In vitro results demonstrated that all the synthesised scaffolds were non-toxic, biocompatible, and promoted osteoblasts' adhesion and growth. The (20,10) and (40,10) scaffolds promoted the proliferation of osteoblasts due to the higher porosity and DCPD-Fe ratio. XRD results showed that the composite material Ti/ DCPD-Fe exhibited a better cell hosting environment than pure titanium. XPS and EDX data presented higher oxygen, nitrogen, and carbon ratio on the scaffolds' surface; reffering to cells' metabolic activity.

Chapter 7

Overall Discussion

7.1 Characterisation of Scaffolds

The powder metallurgy with a space holder technology was feasible and effective for producing porous composite scaffolds with ~ 38 – 60% open porosity. The phase constitution of the sintered composite material (titanium with 10%vol Fe^{3+} dopped brushite) was α-titanium and β-pyrophosphate (β-$Ca_2P_2O_7$). Beta pyrophosphate is a promising material for bone tissue engineering due to its significant role in hard tissue mineralisation, as reported in previous studies [331, 332]. XPS results showed that the surface of the sintered composite material presented the formation of calcium titanate $CaTiO_3$ whilst only TiO_2 was detected on the surface of sintered pure titanium. According to literature, these oxides provide the scaffold's surface with properties similar to those of natural bone, enhancing biocompatibility and increasing the bonding with cells [277, 284, 289, 328-330].

The synthesised porous scaffolds (20,0), (20,10), (40,0) and (40,10) included an optimal pore size distributed between 100 – 450 μm. According to tissue engineering research, bone scaffolds must have a minimum pore size of 50 – 100 μm for adequate bone regeneration [38, 47, 194-196]. Pore size directly affects new bone development since larger pores vascularise and stimulate osteogenesis faster [20, 102, 333]. Smaller pores (< 50 μm) were also observed in the synthesised scaffolds, which are beneficial for providing an interconnection throughout the whole structure. The μCT images displayed the open and interconnected pores, which should provide adequate fixation to the surrounding tissue and promote the diffusion of oxygen and nutrients to cells and transport metabolic waste out of the scaffold [334, 335].

On the othe hand, the lack of vascularisation in large bone defects due to a scaffold with closed pores is one of the most critical obstacles limiting the extent of bone regeneration[54, 336-339]. The porous composite scaffold (40,10) with interconnected and accessible pores ~ 95% is promising to successfully promote vascularisation at the defect site.

7.2 Mechanical Behaviour of Scaffolds

The fabrication using powder metallurgy with a space holder greatly influenced the scaffolds' mechanical properties. Mixing pure titanium with DCPD-Fe mineral increased the porosity inside the pressed and sintered structure, resulting in lower density values, eventually influencing the mechanical integrity. However, introducing pores into the scaffold structure either by the space holder KCl or the DCPD-Fe particles was beneficial in reducing the stiffness to match the natural bone value. This finding was consistent with previous studies on porous materials, showing a decrease in elastic modulus with increasing total porosity [303]. In general, high porosity increases the possibility of forming micro-cracks or defects in the structure, decreasing compressive strength [93, 308]. Therefore, a balance must be preserved during the design and manufacturing of scaffolds to get the appropriate porous structure with optimal mechanical properties. The additive of DCPD-Fe mineral to titanium helped moderate the stiffness of scaffolds to match the cortical femoral bone without causing stress localisation due to very high porosity (> 70%), as reported in previous works [26, 102].

The results showed that the rise in sintering temperature significantly increased elastic modulus, compressive strength and yield stress due to high-temperature diffusion, which enhanced the particles' bonding [293, 309]. On the other hand, XRD results displayed an increase in the lattice parameter ratio of c/a with a higher sintering temperature due to the upper interstitial oxygen concentration. This finding suggests that the mechanical properties of the synthesised scaffolds were affected by the lattice expansion that arises during the sintering process. The increase in c/a ratio with respect to the interstitial oxygen concentration increases the strength of scaffolds due to the restricted number of slip planes in the hcp structure, as proven in previous studies [266, 268, 269, 293, 309-312, 327, 340].

However, oxygen concentration must be cautiously controlled to obtain the required mechanical properties. High oxygen concentration leads to massive oxidation, negatively

affecting the mechanical properties of titanium. We can see the enormous difference in mechanical properties of the scaffolds sintered in the air compared to those in an inert atmosphere (Appendix A).

The (20,10) and (40,10) scaffolds exhibited a more uniform stress distribution and better strain transfer across the scaffold/bone interface compared to the pure titanium scaffold. The stress and strain developed by (20,10) and (40,10) scaffolds were comparable with cortical femur bone values. The designed scaffolds exhibited mechanical behaviour and stiffness, making them suitable for minimising the stress shielding effect and reducing mechanically mediated bone resorption [319]. However, we can not decide which scaffold is the best to use as a replacement for a segmental bone defect until we determine the type of fixation. The fixation of the scaffold with the surrounding bone must give support during bone healing. However, several factors, including the surgery, scaffold and patient, will play an essential role in determining the best fixation method.

7.3 Cellular Response of Scaffolds

The influence of scaffold on the viability and growth of osteoblasts is a critical factor in the success of bone regeneration. Therefore, scaffolds with different compositions and porosity were tested *in vitro*. The outcomes suggested that all the synthesised scaffolds were non-toxic and biocompatible. Furthermore, cells presented excellent adhesion and growth, and their morphology shows a healthy attachment with well-spread shape, which is indicative of a high cellular interaction with all scaffolds' surfaces. As indicated elsewhere, these proprieties demonstrated the osteoconductive capability potential of all these scaffolds [20, 103, 161]. However, exploring precisely the effect of porosity and Fe^{+3} doped brushite demonstrated the cell proliferation rate increased by increasing the scaffold's porosity. In Chapter 4, μCT results illustrated how pores were interpenetrating and interconnected in the scaffold with 40 vol%

KCl (40,0), whilst lower interconnectivity was in the scaffold with 20 vol% KCl (20,0) due to the closed pores. These results can explain the significant effect of the scaffolds with 40%vol KCl on cell growth and proliferation density. The porous structure with interconnected micro and macro pores is ideal for bone scaffolds as it facilitates cell seeding, penetration, and migration of osteoblast cells. Also, pores interconnectivity provides adequate diffusion of nutrients and oxygen to cells and transports metabolic waste from the scaffold [20, 40, 98, 169, 170].

In the extended incubation period with cells (after three and seven days), the composite scaffold (0,10) containing DCPD-Fe mineral enhanced the proliferation of osteoblasts. The composite material Ti/10DCPD-Fe exhibited a better cell hosting environment than the pure titanium for the long term incubation. XPS results showed the formation of $CaTiO_3$ on the surface of the sintered composite material, which can be one of the reasons behind the higher osteoblast adhesion and proliferation. Previous studies showed better integration with the surrounding bone after coating or modification of titanium surface with $CaTiO_3$ [283-288].

Characterisation results presented a higher oxygen concentration in the composite material after cell seeding due to the formation of titanium oxide $TiO_{0.176}$ which contains ~ 15% atomic percent of oxygen. This product indicates that cells were growing on the surface of the composite material (Ti/10DCPD-Fe) and provided oxygen to the scaffold. The additive of 10 %vol DCPD-Fe mineral to pure titanium succeeded in creating bio-interactive material to enhance bone regeneration. The composite material (Ti/10DCPD-Fe) is supposed to have osteoconductive and osteoinductive properties due to the ability to create biodegradable channels. Many studies have reported a better degradation rate of Beta-calcium pyrophosphate (β-$Ca_2P_2O_7$) comparable to bone regeneration rate than other CaPs materials to support bone formation [124, 128-133, 200].

On the other hand, the potential of using the dissolved oxygen in the composite scaffold as a source of O_2 to support cell growth and activity for a longer term would also be promising.

However, an extended dsDNA quantification test should be done to confirm this finding and investigate the effect of dissolved oxygen on the cells' growth.

Chapter 8
Conclusion & Future Work

8.1 Conclusion

This work presented the design and fabrication of porous composite scaffolds (titanium/ Fe^{+3} doped brushite), which can provide the appropriate mechanical support and biological response during bone restoration. The most important outcomes of this research could be summarised as the following:

- The resultant phases after sintering composite material (titanium/10% vol Fe^{3+} dopped brushite) in argon at 1000^{o}C were hexagonal α-titanium and β-pyrophosphate (β-$Ca_2P_2O_7$).

- Surface analysis for the sintered composite material (Ti/10DCPD-Fe) presented the formation of calcium titanate $CaTiO_3$.

- The powder metallurgy with space holder process was feasible in fabricating scaffolds with open, large enough and interconnected pores. Scaffolds (40,10) and (20,10) are supposed to allow vascularisation and ease penetration of cells.

- The elastic modulus of the (40,10) and (20,10) scaffolds were 8.7 and 20.17 GPa, respectively at sintering temperature ≥ 1000^{o}C. These values are comparable with that of the human femur bone (4 - 20 GPa), which indicates they are supposed to minimise the stress-shielding effect.

- (40,10) and (20,10) scaffolds exhibited also suitable compressive strength ~ 130 and 165 MPa, respectively at sintering temperature ≥ 1000^{o}C. These values are similar to the femoral cortical bone ~ 90 - 180 Mpa.

- The numerical study suggests that the synthesised scaffolds (20,10) and (40,10) have the potential to perform well for bone regeneration within segmental defects and could be biomechanically flexible in interaction with the surrounding bone.

- All the synthesised scaffolds were non-toxic and biocompatible with no harmful effects on the osteoblast cells.

- The *in-vitro* results showed that the synthesised scaffolds were osteoconductive and supported cells to attach and proliferate. Higher proliferation rates were detected in scaffolds containing DCPD-Fe mineral and higher porosity.

- The porous composite scaffolds (20,10) and (40,10) could be promising for promoting successful osseointegration. These scaffolds succeeded in meeting the five requirements of bone scaffolds as identified in the 'Diamond Concept'. The scaffolds are biocompatible, osteoconductive, have the proper porous structure, exhibit the potential to trigger vascularisation and have mechanical properties consistent with the cortical bone.

8.2 Limitations

There are two major limitations in this work that could be addressed in future research.

- First, the numerical study was affected by the computer performance and specifications. The shortage of a high-speed processor restricted the creation of a 3D meshed model that imitates the actual structure of the porous composite scaffold. The study considered the physical and mechanical properties of the synthesised scaffolds without taking into account the effect of the geometry and distribution of pores on stress and strain behaviour.

- Second, the lockdowns and restrictions resulting from the Covid-19 pandemic adversely affected the biological experiments. The entire bone cell viability and proliferation studies were destroyed during the lockdown, which resulted in repeating the incomplete work. The period of time spent on repeating was designed to spend on angiogenesis testing for the synthesised porous composite scaffolds.

8.3 Recommendations and Future Work

At this point, some future research directions are proposed that can further enhance the work developed in this thesis.

- Further mechanical testing would be recommended to get a comprehensive understanding of the mechanical behaviour of the synthesised scaffolds. The scaffold may display good behaviour under uniaxial stress (as addressed in this work), but when multiaxial stress is produced due to a notch, the scaffold might not withstand the elastic and plastic deformation in different directions. Therefore, three points bending test with a notch would be important to calculate the fracture toughness of the scaffolds.

- The numerical study should be validated using a 3D model created by high-resolution μCT images.

- The finite element analysis could include the fixation method for the synthesised scaffold with bone tissue.

- Further studies are required to investigate the influence of the DCPD-Fe mineral on the osteogenic differentiation, angiogenesis and mineralisation.

- Endothelial cells assay would be suggested as these cells are from the inner surface of blood vessels and thus can form vascularisation networks. This test would inspect the influence of the created porous structure on the proliferation of endothelial cells.

- *In vivo* experiments for the (20,10) and (40,10) scaffolds will be conducted during my next three years project to investigate the influence of the synthesised scaffolds on cells response.

- Also, the porosity and mineral ratio of the porous composite material (Ti/ DCPD-Fe) will be adjusted by considering porosity value between (20%vol and 40%vol KCl) and increasing the mineral ratio by more than (10%vol DCPD-Fe) which potentially may result in better biodegradable behaviour.

- Furthermore, designing and fabricating a two-layered scaffold that embodies all the required properties in a physiological analogue of a natural bone will be running. The outer layer of the scaffold is made up of the porous composite material Ti/10DCPD-Fe (investigated in this thesis), and the inner layer is made up of freeze-dried chitosan with

brushite (investigated in my colleague's work [345]). The outer layer can work as synthetic cortical bone providing a scaffold with mechanical stability and stimulation of bone growth, and the inner layer behaves as synthetic cancellous to facilitate tissue growth and ensure vascularisation.

Appendices

Appendix A: Scaffolds sintered in air

1. Scaffolds characterisation

The X-ray diffraction patterns of the titanium samples sintered in two different environments, air and argon, are presented in Figure 1 and compared with the X-ray diffraction pattern of the initial Ti powder.

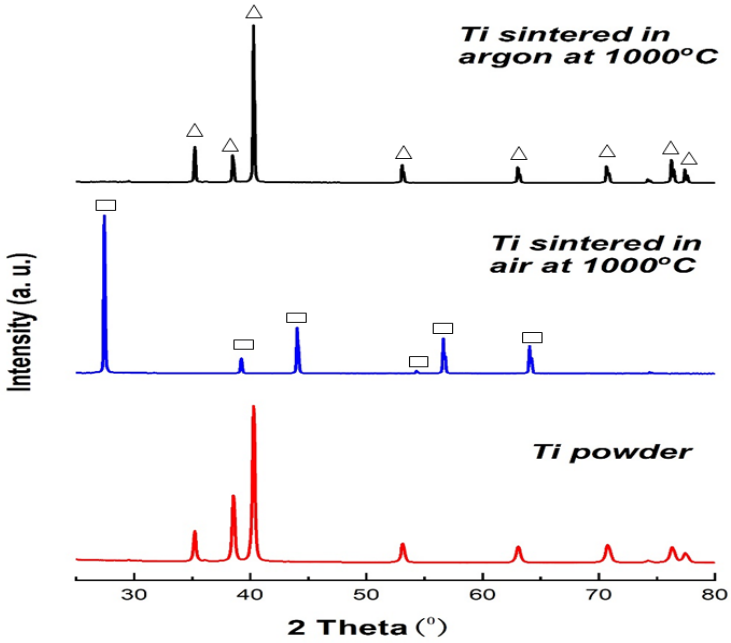

Figure 1: Normalised X-ray diffraction patterns of initial Ti powder and Ti pellets sintered in air and argon at 1000 °C for 2h, with indexing to the JCPDS reference files of titanium (Δ) and titanium dioxide (□).

Ti samples sintered in these two environments exhibited different diffraction patterns. Ti sintered in the presence of O_2 had diffraction peaks associated with $2\theta^o$ ~ 27.43°, 39.18°, 56.63°, 64.06°. These peaks match the reference standard XRD data for TiO_2 rutile (JCPDS:

00-034-0180). Ti pellet was oxidised because titanium reacted rapidly with the oxygen when heated in the air at 1000 ^{o}C due to the strong chemical affinity and high solid solubility of oxygen in titanium [312]. Whilst all the peaks of titanium pellet sintered in an inert atmosphere were related to α-Ti with a hexagonal close-packed (hcp) structure, according to the information reported in the database card (JCPDS 04-006-2824).

The EDX elemental mapping of pure titanium samples sintered in air showed that most of the titanium was oxidised, as shown in Figure 2.

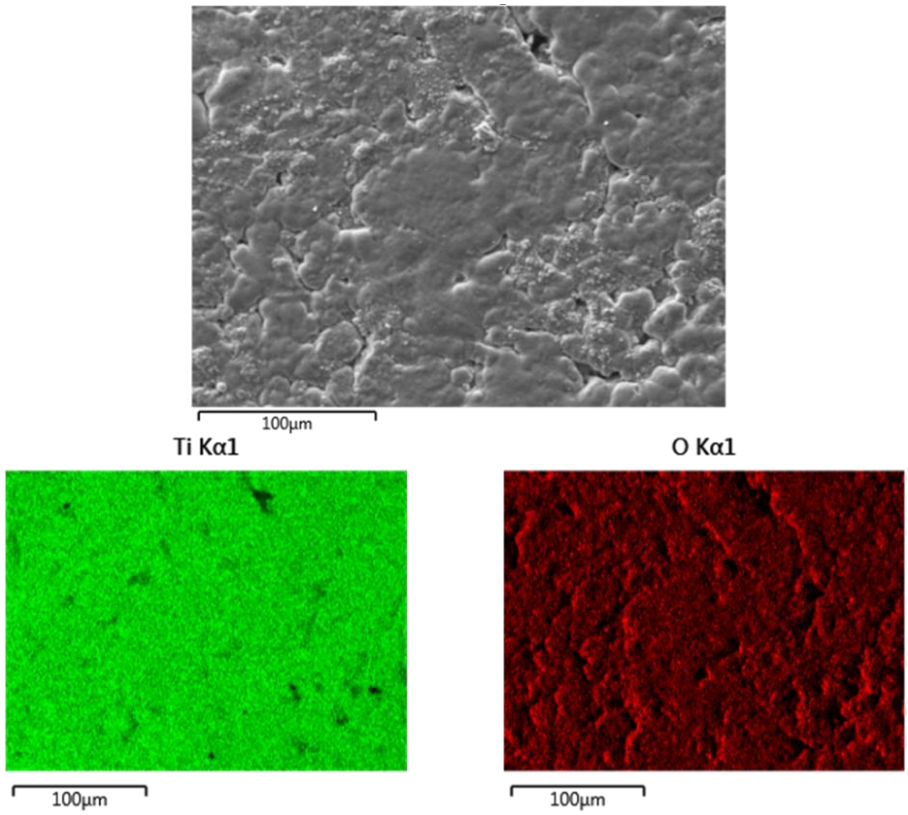

Figure 2: EDX mapping of pure titanium sample sintered in the presence of O_2 at 1000^{o}C for 2h.

2. Mechanical properties:

Table 1 displays the ultimate strength of the scaffolds designed and fabricated according to Box Behnken's design. Compressive strength was negatively affected by the sintering process in air. The low values of compressive strength restrict the use of these scaffolds in load-bearing applications.

Table 1: Compressive strength of the synthesised scaffolds sintered in air.

Temperature [°C]	KCl [vol%]	CaP [vol%]	Ultimate Strength [MPa]
850	0	5	113
850	20	0	85
850	20	10	37
850	40	5	49
1000	0	0	133
1000	0	10	15
1000	20	5	37
1000	40	0	33
1000	40	10	25
1150	0	5	17
1150	20	0	16
1150	20	10	19
1150	40	5	18

Appendix B: Experimental protocols

Proliferation experiment using DNA quantitation (Quant-iT PicoGreen dsDNA Assay Kit)

This protocol was used to determine the proliferation of cells after 4 hours, 1day, 3days, and 7 days of incubation.

Cells lysis:

- 1% solution of Triton-X100 (Alfa Aesar) was prepared by adding PBS.
- The samples were rinsed twice with PBS and 1.5 mL of 1% Triton was added to the samples and frozen for 15 mins at -80°C and then defrosted at 37°C. This cycle was repeated three times, with scraping by pipette tips each time to lyse all the cells.
- The lysates were then centrifuged at 1200 rpm for 5 min, and 100 µL of the supernatants was used to determine DNA content.

Standard stalk solution of ds DNA:

The data were calibrated using a DNA standard curve following these steps:

- First, 1x TE buffer solution was prepared by diluting 750 µl of 20x TE buffer (200 mM Tris-HCl, 20 mM EDTA, pH 7.5, Invitrogen by Thermo Fisher Scientific) in 14.25 ml of nuclease free water.
- Then ds DNA standard solution was prepared by diluting 20 µl of ds DNA (100µg/ml) (Invitrogen by Thermo Fisher Scientific) in 980 µl of 1x TE buffer to prepare serial dilutions (2000, 1000, 500, 250, 125, 62.5, 31.3,15.6, 7.8, 3.9, 1.95, 0.98, 0.49 ng/mL) and the blank (TE buffer only) to get several points for the DNA standard curve.

Picogreen solution preparation:

- Each 10 µl concentrated of PicoGreen (Invitrogen by Thermo Fisher Scientific) was diluted in a 990 µl TE buffer to the prepare PicoGreen solution.
- For DNA quantitation, 100 µl of PicoGreen solution was added to each well (i.e., to each 100 µl standard DNA and 100 µl from the samples in the 96 well plate), and then the well plate was kept at room temperature for 5 min in the dark.
- The plate reader (Varioskan Flash plate reader, Thermo Scientific) was used for fluorescence examination for DNA evaluation at excitation wavelength 480 nm and emission of 520 nm.

References

1. Rosen, C.J., 2009. Primer on the Metabolic Bone Diseases and Disorders of Mineral Metabolism. John Wiley & Sons.
2. National Hip Fracture Database, annual report. 2017, Royal College of Physicians: London: RCP.
3. National Hip Fracture Database (NHFD), annual report 2018, Royal College of Physicians: London: RCP.
4. National Hip Fracture Database (NHFD) annual report 2019. United Kingdom.
5. Johansen, A., et al., 2014. 48 Using the national hip fracture database (NHFD) to profile the impact of hip fracture on the NHS. *Age and Ageing*. 43(2): p. ii13-ii13.
6. Tyas, B., Wilkinson, M. and Singisetti, K., 2021. Effect of Covid-19 on best practice care of hip fracture patients: An analysis from the National Hip Fracture Database (NHFD). *The Surgeon*. 19(5): p. e298-e303.
7. Svedbom, A., et al., 2013. Osteoporosis in the European Union: a compendium of country-specific reports. *Arch Osteoporos*. 8(1-2): p. 137.
8. Amini, A.R., Laurencin, C.T. and Nukavarapu, S.P., 2012. Bone tissue engineering: recent advances and challenges. *Critical Reviews in Biomedical Engineering*. 40(5).
9. Mozafari, M., F. Sefat, and A. Atala, editors, 2019. Handbook of Tissue Engineering Scaffolds: Volume One [Online]. Woodhead Publishing. [Accessed 13 July 2020]. Available from: https://books.google.co.uk/books?hl=en&lr=&id=OZadDwAAQBAJ&oi=fnd&pg=PP1&dq=#v=onepage&q&f=false
10. Giannoudis, P.V., Einhorn, T.A. and Marsh, D., 2007. Fracture healing: the diamond concept. *Injury*. 38: p. S3-S6.
11. Giannoudis, P.V., et al., 2008. The diamond concept–open questions. *Injury*. 39: p. S5-S8.
12. Calori, G.M. and Giannoudis, P.V., 2011. Enhancement of fracture healing with the diamond concept: the role of the biological chamber. *Injury*. 42(11): p. 1191-1193.
13. Kanis, J., et al., Risk of hip fracture according to the World Health Organization criteria for osteopenia and osteoporosis. *Bone*, 2000. 27(5): p. 585-590.
14. Walsh, W.R., et al., 2017. Critical size bone defect healing using collagen–calcium phosphate bone graft materials. *PloS One*. 12(1): p. e0168883.
15. Cooper, G.M., et al., 2010. Testing the "critical-size" in calvarial bone defects: revisiting the concept of a critical-sized defect (CSD). *Plastic Reconstructive Surgery*. 125(6): p. 1685–1692.
16. Schemitsch, E.H., 2017. Size matters: defining critical in bone defect size. *Journal of Orthopaedic Trauma*. 31: p. S20-S22.
17. Miller, C.P. and Chiodo, C.P., 2016. Autologous bone graft in foot and ankle surgery. *Foot Ankle Clinics*. 21(4): p. 825-837.
18. Arrington, E.D., et al., 1996. Complications of iliac crest bone graft harvesting. *Clinical Orthopaedics & Related Research*. 329: p. 300-309.
19. Elsalanty, M.E. and Genecov, D.G., 2009. Bone grafts in craniofacial surgery. C*raniomaxillofacial trauma & reconstruction*. 2(3-4): p. 125-134.
20. Moreno, M., et al., 2016. Scaffolds for Bone Regeneration: State of the Art. *Curr Pharm Des*. 22(18): p. 2726-36.

21. Chiarello, E., Cadossi, M., Tedesco, G., Capra, P., Calamelli, C., Shehu, A. and Giannini S., 2013. Autograft, allograft and bone substitutes in reconstructive orthopedic surgery. *Aging clinical and experimental research*. 25(1):101-103.
22. Nazirkar, G., et al., 2014. Effortless effort in bone regeneration: a review. *Journal of International Oral Health*. 6(3): p. 120.
23. Zimmermann, G. and Moghaddam, A., 2011. Allograft bone matrix versus synthetic bone graft substitutes. *Injury*. 42: p. S16-S21.
24. Siregar, H., Gunawan, R. and Fitriadi, D., 2021. A Case Series: Non-vascularized Autologous Fibular Graft in the Treatment of Major Segmental Bone Defect after Post-traumatic at Diaphyseal Femur. *Macedonian Journal of Medical Sciences*. 9(C): p. 175-181.
25. Chen, Q. and Thouas, G.A., 2015. Metallic implant biomaterials. *Materials Science and Engineering: R: Reports*. 87: p. 1-57.
26. Kramschuster, A. and Turng, L.S., 2012. Fabrication of tissue engineering scaffolds [Online]. In: Ebnesajjad, S., editor. *Handbook of Biopolymers and Biodegradable Plastics: Properties, Processing and Applications*. [Accessed 20 June 2020]. Available from:https://books.google.co.uk/books?hl=en&lr=&id=2ICjqmDWVQMC&oi=fnd&pg=PA427&dq
27. Sanli, I., Arts, J.J.C. and Geurts, J., 2016. Clinical and radiologic outcomes of a fully hydroxyapatite-coated femoral revision stem: excessive stress shielding incidence and its consequences. *The Journal of Arthroplasty*. 31(1): p. 209-214.
28. Gordeladze, J.O., et al., 2017. Bone tissue engineering: state of the art, challenges, and prospects. Tissue Engineering for Artificial Organs: Regenerative Medicine, *Smart Diagnostics and Personalized Medicine. Wiley*. p. 525-551.
29. Piveteau, L.-D., et al., 1999. Thin films of calcium phosphate and titanium dioxide by a sol-gel route: a new method for coating medical implants. *Journal of Materials Science: Materials in Medicine*. 10(3): p. 161-167.
30. Ibrahim, M.Z., et al., 2017. Biomedical materials and techniques to improve the tribological, mechanical and biomedical properties of orthopedic implants–A review article. *Journal of Alloys and Compounds*. 714: p. 636-667.
31. Hench, L.L. and Jones, J.R., 2015. Bioactive glasses: frontiers and challenges. *Frontiers in Bioengineering and Biotechnology*. 3: p. 194.
32. Ma, R., et al., 2016. Osseointegration of nanohydroxyapatite- or nano-calcium silicate-incorporated polyetheretherketone bioactive composites in vivo. *International Journal of Nanomedicine*. p. 6023–6033.
33. Wang, H. 2004. *Hydroxyapatite degradation and biocompatibility.* Ph.D. thesis, The Ohio State University.
34. Clavell, R.S., et al., 2016. *In vitro* assessment of the biological response of Ti6Al4V implants coated with hydroxyapatite microdomains. *Journal of Biomedical Materials Research Part A*. 104(11): p. 2723-2729.
35. Levine, B.R. and Fabi, D.W., 2010. Porous metals in orthopedic applications – A review. *Materialwissenschaft und Werkstofftechnik*. 41(12): p. 1001-1010.
36. Saran, U., Piperni, S.G. and Chatterjee, S., 2014. Role of angiogenesis in bone repair. *Archives of Biochemistry and Biophysics*. 561: p. 109-117.
37. Ma, R., et al., 2016. Osseointegration of nanohydroxyapatite-or nano-calcium silicate-incorporated polyetheretherketone bioactive composites *in vivo*. *International Journal of Nanomedicine*. 11: p. 6023.
38. Liverani, L., Roether, J. and Boccaccini, A., 2017. Nanofiber composites in bone tissue engineering [Online], In: Ramalingam, M. and Ramakrishna, S., editors. *Nanofiber Composites for Biomedical Applications*. Elsevier. p. 301-323. [Accessed 18 June

2020]. Available from: https://www.sciencedirect.com/science/article/pii/B9780081001738000120
39. Liu, P.S. and Chen, G.F., 2014. *Porous materials: processing and applications* [Online]. Elsevier. p. 113-188. [Accessed 23 August 2020]. Available from: https://books.google.co.uk/books?hl=en&lr=&id=KwJ0AwAAQBAJ&oi=fnd&pg=PP1&dq
40. O'brien, F.J., 2011. Biomaterials & scaffolds for tissue engineering. *Materials Today*. 14(3): p. 88-95.
41. Polo-Corrales, L., Latorre-Esteves, M. and Ramirez-Vick, J.E., 2014. Scaffold design for bone regeneration. *Journal of Nanoscience and Nanotechnology*. 14(1): p. 15-56.
42. Sheikh, M.S.A., Ganorkar, A.P. and Dehankar, R.N., 2016. Finite Element Analysis of Femoral Intramedullary Nailing. *Journal for Research*. 2(10): p. 2395-7549.
43. Kumar, K.N., et al., 2015. Biomechanical stress analysis of a human femur bone using ANSYS. *Materials Today: Proceedings*. 2(4-5): p. 2115-2120.
44. Davis, J. 2003. Materials for Medical Devices. ASM Handbook Series.
45. Bansiddhi, A., et al., 2008. Porous NiTi for bone implants: a review. *Acta Biomaterialia*. 4(4): p. 773-782.
46. Long, M. and Rack, H.J., 1998. Review, Titanium alloys in total joint replacement—a materials science perspective. 19: p. 1621–1639.
47. Bansiddhi, A. and Dunand, D.C., 2014. Titanium and NiTi foams for bone replacement [Online]. In: Mallick, K., editor. *Bone Substitute Biomaterials*. Woodhead Publishing. p. 142-179. [Accessed 12 April 2021]. Available from: https://www.sciencedirect.com/science/article/pii/B978085709497150007X
48. Amini, A.R., Laurencin, C.T. and Nukavarapu, S.P., 2012. Bone tissue engineering: recent advances and challenges. Critical Reviews. *Biomedical Engineering*. 40(5).
49. Anon. Structure of bone [Online]. Department of Materials Science & Metallurgy, University of Cambridge, [Accessed 21 July 2021]. Available from: https://www.doitpoms.ac.uk/tlplib/bones/structure.php
50. O'Keefe, R.J., Tuan, R.S., Lane, N.E., Awad, H.A., Barry, F., Bunnell, B.A., Colnot, C., Drake, M.T., Drissi, H., Dyment, N.A. and Fortier, L.A., 2020. American Society for Bone and Mineral Research-Orthopaedic Research Society Joint Task Force Report on Cell-Based Therapies. *Journal of Bone and Mineral Research*. 35(1), pp.3-17.
51. Augat, P. and Schorlemmer, S., 2006. The role of cortical bone and its microstructure in bone strength. *Age and Ageing*. 35(2): p. ii27-ii31.
52. Viguet-Carrin, S., Garnero, P. and Delmas, P.D., 2006. The role of collagen in bone strength. *Osteoporosis international*. 17(3): p. 319-336.
53. Muiznieks, L.D. and Keeley, F.W., 2013. Molecular assembly and mechanical properties of the extracellular matrix: A fibrous protein perspective. *Biochimica et Biophysica Acta -Molecular Basis of Disease*. 1832(7): p. 866-875.
54. Dapporto, M., Tampieri, A. and Sprio, S., 2017. Composite calcium phosphate/titania scaffolds in bone tissue engineering [Online]. In: Janus, M., editor. *Application of Titanium Dioxide*. p. 43-59. [Accessed 08 April 2022]. Available from: https://books.google.co.uk/books?hl=en&lr=&id=6m-QDwAAQBAJ&oi=fnd&pg=PA43&dq=Dapporto,+
55. Biologydictionary.net Editors. *Compact Bone* [Online]. Biology Dictionary, Biologydictionary.net, [Accessed 28 April 2019]. Available from: https://biologydictionary.net/compact-bone/
56. Anon. *Structure and composition of bone* [Online]. Department of Materials Science & Metallurgy, University of Cambridge, [Accessed 21 July 2021]. Available from: https://www.doitpoms.ac.uk/tlplib/bones/structure.php

57. Voo, L., Armand, M. and Kleinberger, M., 2004. Stress fracture risk analysis of the human femur based on computational biomechanics. *Johns Hopkins APL Technical Diges*. 25(3): p. 223-230.
58. Heaney, R.P. and Whedon, G.D., *Bone* [Online], Encyclopedia Britannica. [Accessed 13 June 2018]. Available from: https://www.britannica.com/science/bone-anatomy/Bone-morphology.
59. Rucci, N., 2008. Molecular biology of bone remodelling. *Clinical Cases in Mineral Bone Metabolism*. 5(1): p. 49.
60. Florencio-Silva, R., et al., 2015. Biology of bone tissue: structure, function, and factors that influence bone cells. *BioMed Research International*. p. 17.
61. Nam, N.H., and Kampa, N., 2013. Bone Cell Function: A Review. *The Thai Journal of Veterinary Medicine*. 43(3): p. 329–336.
62. Shier, D., Butler, J. and Lewis, R., 2003. *Hole's essentials of human anatomy and physiology*. McGraw-Hill. [Accessed 17 July 2019]. Available from: https://hhh.gavilan.edu/jcrocker/documents/Ch05-08Review.pdf
63. Delaisse, J.-M., et al., 2020. Re-thinking the bone remodeling cycle mechanism and the origin of bone loss. *Bone*. 141: p. 115628.
64. Hadjidakis, D.J. and Androulakis, I.I., 2006. Bone remodeling. *Annals of the New York Academy of Sciences*. 1092(1): p. 385-396.
65. Carano, R.A. and Filvaroff, E.H., 2003. Angiogenesis and bone repair. *Drug Discovery Today*. 8(21): p. 980-989.
66. LaStayo, P.C., Winters, K.M. and Hardy, M., 2003. Fracture healing: bone healing, fracture management, and current concepts related to the hand. J*ournal of Hand Therapy*. 16(2): p. 81-93.
67. Cheng, W., et al., 2020. Injectable hydrogel systems with multiple biophysical and biochemical cues for bone regeneration. *Biomaterials Science*. 8(9): p. 2537-2548.
68. Checa, S., 2018. Multiscale agent-based computer models in skeletal tissue regeneration [Online]. In: Cerrolaza, M., Shefelbine, S.J. and Garzón-Alvarado D., editors. *Numerical Methods and Advanced Simulation in Biomechanics and Biological Processes*. Academic Press. p. 239-244. [Accessed 15 November 2019]. Available from: https://www.sciencedirect.com/science/article/pii/B9780128117187000137
69. Dimitriou, R., et al., 2011. Bone regeneration: current concepts and future directions. *BMC Medicine*. 9(1): p. 1-10.
70. Marsell, R. and Einhorn, T.A., 2011. The biology of fracture healing. *Injury*. 42(6): p. 551-555.
71. Giannoudis, P.V., Dinopoulos, H. and Tsiridis, E., 2005. Bone substitutes: an update. *Injury*. 36(3): p. S20-S27.
72. Albrektsson, T. and Johansson, C., 2001. Osteoinduction, osteoconduction and osseointegration. *European Spine Journal*. 10: p. S96–S101.
73. Di Silvio, L. and Jayakumar, P., 2009. Cellular response to osteoinductive materials in orthopaedic surgery [Online]. In: Di Silvio, L., editor. *Cellular Response to Biomaterials*. Woodhead Publishing. p. 313-343. [Accessed 26 May 2021]. Available from: https://www.sciencedirect.com/science/article/pii/B9781845693589500132
74. Iaquinta, M.R., Mazzoni, E., Bononi, I., Rotondo, J.C., Mazziotta, C., Montesi, M., Sprio, S., Tampieri, A., Tognon, M. and Martini, F., 2019. Adult stem cells for bone regeneration and repair. *Frontiers in Cell Developmental Biology*. 7: p. 268.
75. Parithimarkalaignan, S. and Padmanabhan, T.V., 2013. Osseointegration: An Update. *The Journal of Indian Prosthodontic Society*. 13(1): p. 2-6.
76. Bankoff, A. D. P., 2012. Biomechanical Characteristics of the Bone. In: Goswami, T., editor. *Human Musculoskeletal Biomechanics* [Online]. London: IntechOpen.

[Accessed 06 June 2019]. Available from: https://www.intechopen.com/chapters/21043 doi: 10.5772/19690
77. Koch, J.C., 1917. The laws of bone architecture. *American Journal of Anatomy*. 21(2): p. 177-298.
78. Wang, X., Nyman, J.S., Dong, X., Leng, H. and Reyes, M., 2010. Fundamental Biomechanics in Bone Tissue Engineering. S*ynthesis Lectures on Tissue Engineering*. 2(1): p. 1-225.
79. Arshad, R. 2004. Modelling of the inhomogeneities within the human intervertebral disc. MSc. thesis, Institute of Mechanics, Chair II, University of Stuttgart
80. Mubeen B, Ahmed I, and Jameel A., 2015. Study of mechanical properties of bones and mechanics of bone fracture. *In Proceedings of 60th Congress of ISTAM*. p. 16-19.
81. Marcus R, Dempster DW, Cauley JA, Feldman D, editors 2013. Osteoporosis (Fourth Edition) [Online]. Academic Press. [Accessed 09 June 2019]. Available from: https://books.google.co.uk/books?hl=en&lr=&id=b1FtazykqzMC&oi=fnd&pg=PP1&dq=Marcus,+R.,+et+al.,+Osteoporosis.
82. Boughton, O.R., et al., 2018. Measuring bone stiffness using spherical indentation. *PLoS One*. 13(7): p. e0200475.
83. Lowe, J.A. and Fischer, S.J. 2018. Femur Shaft Fractures-Broken Thighbone [Online]. *OrthoInfo*. [Accessed 20 May 2020]. Available from: https://orthoinfo.aaos.org/en/diseases--conditions/femur-shaft-fractures-broken-thighbone/
84. Bergh C, Wennergren D, Möller M, and Brisby H., 2020. Fracture incidence in adults in relation to age and gender: A study of 27,169 fractures in the Swedish Fracture Register in a well-defined catchment area. *PloS One*. 15(12): p. e0244291.
85. Roseti, L., et al., 2017. Scaffolds for bone tissue engineering: state of the art and new perspectives. *Materials Science and Engineering: C*. 78: p. 1246-1262.
86. Meyer, A.C., et al., 2021. Trends in hip fracture incidence, recurrence, and survival by education and comorbidity: a Swedish Register-based Study. *Epidemiology (Cambridge, Mass.)*. 32(3): p. 425.
87. Deshmukh, R. and Kulkarni, S., 2015. A review on biomaterials in orthopedic bone plate application. *International Journal of Current Engineering and Technology*. 5(4): p. 2587-2591.
88. Das, S. and Sarangi, S.K., 2014. Finite element analysis of femur fracture fixation plates. *International Journal of Basic and Applied Biology*. 1(1): p. 1-5.
89. Maharaj, P.S., Maheswaran, R. and Vasanthanathan, A., 2013. Numerical analysis of fractured femur bone with prosthetic bone plates. *Procedia Engineering*. 64: p. 1242-1251.
90. Lesso-Arroyo, R., et al., 2004.Biomechanical Behavior of the Knee Joint Using ANSYS. *in International ANSYS Conference Proceedings*.
91. Amornsamankul, S., Kaorapapong, K. and Wiwatanapataphee, B., 2010. Three-dimensional simulation of femur bone and implant in femoral canal using finite element method. *International Journal of Mathematics and Computers in Simulation*. 4(4): p. 171-178.
92. Wieding, J., et al., 2013. Finite element analysis on the biomechanical stability of open porous titanium scaffolds for large segmental bone defects under physiological load conditions. *Medical Engineering & Physics*. 35(4): p. 422-432.
93. Karuppudaiyan, S., Singh, D.K.J. and Santosh V.M., 2018. Finite element analysis of scaffold for large defect in femur bone. *in IOP Conference Series: Materials Science and Engineering*. IOP Publishing.

94. Damien, C.J. and Parsons, J.R., 1991. Bone graft and bone graft substitutes: a review of current technology and applications. *Journal of Applied Biomaterials & Functional Materials*. 2(3): p. 187-208.
95. Cypher, T.J. and Grossman, J.P., 1996. Biological principles of bone graft healing. *The Journal of Foot and Ankle Surgery*. 35(5): p. 413-417.
96. Dimitriou, R., et al., 2011. Complications following autologous bone graft harvesting from the iliac crest and using the RIA: a systematic review. *Injury*. 42: p. S3-S15.
97. Tang, D., et al., 2016. Biofabrication of bone tissue: approaches, challenges and translation for bone regeneration. *Biomaterials*. 83: p. 363-382.
98. Ghassemi, T., et al., 2018. Current concepts in scaffolding for bone tissue engineering. *Archives of Bone and Joint Surgery*. 6(2): p. 90.
99. Bártolo, P.J., Almeida, H.A., Rezende, R.A., Laoui, T., Bidanda, B., 2008. Advanced Processes to Fabricate Scaffolds for Tissue Engineering [Online]. In: Bidanda, B., Bártolo, P. editors. *Virtual Prototyping & Bio Manufacturing in Medical Applications.* Springer, Boston, MA. [Accessed 21 May 2020]. Available from: https://doi.org/10.1007/978-0-387-68831-2_8
100. Giannoudis, P.V., et al., 2013. Bone regeneration strategies: current trends but what the future holds? *Injury*. 44: p. S1-S2.
101. Andrzejowski, P. and Giannoudis, P.V., 2019. The 'diamond concept'for long bone non-union management. *Journal of Orthopaedics and Traumatology*. 20(1): p. 1-13.
102. Gorth, D. and Webster, T., 2011. Matrices for tissue engineering and regenerative medicine [Online]. In: Lysaght, M., and Webster, T., *Biomaterials for Artificial Organs*. Woodhead Publishing. p. 270 - 286. [Accessed 21 May 2020]. Available from: https://www.sciencedirect.com/science/article/pii/B9781845696535500108
103. Bose, S., Roy, M. and Bandyopadhyay, A., 2012. Recent advances in bone tissue engineering scaffolds. *Trends in Biotechnology*. 30(10): p. 546-554.
104. Sergi, R., Bellucci, D. and Cannillo, V., 2020. A review of bioactive glass/natural polymer composites: State of the art. *Materials*. 13(23): p. 5560.
105. Sultana, N., Hassan, M.I. and Lim, M.M., 2015. Scaffolding Biomaterials [Online]. In: *Composite Synthetic Scaffolds for Tissue Engineering and Regenerative Medicine. SpringerBriefs in Materials.* p. 1-11. Springer, Cham. [Accessed 25 June 2020]. Available from:https://doi.org/10.1007/978-3-319-09755-8_1
106. Blackwood, D., 2003. Biomaterials: past successes and future problems. *Corrosion Reviews*. 21(2-3): p. 97-124.
107. Lantada, A.D., 2019. Handbook of active materials for medical devices: advances and applications. Pan Stanford.
108. Winkler, T., et al., 2018. A review of biomaterials in bone defect healing, remaining shortcomings and future opportunities for bone tissue engineering: The unsolved challenge. *Bone & Joint Research*. 7(3): p. 232-243.
109. Mudali, U.K., Sridhar, T.M., Eliaz, N. and Raj, B., 2003. Failures of stainless steel orthopedic devices-causes and remedies. *Corrosion Reviews*. p. 231-268.
110. Bandyopadhyay, A., et al., 2019. Additively manufactured calcium phosphate reinforced CoCrMo alloy: Bio-tribological and biocompatibility evaluation for load-bearing implants. *Additive Manufacturing*. 28: p. 312-324.
111. Liao, Y., et al., 2013. CoCrMo metal-on-metal hip replacements. *Physical Chemistry Chemical Physics*. 15(3): p. 746-756.
112. Milošev, I. 2012. CoCrMo Alloy for Biomedical Applications. In: Djokić, S., editors. *Biomedical Applications. Modern Aspects of Electrochemistry* [Online]. Springer, Boston, MA. [Accessed 15 June 2019]. Available from: https://doi.org/10.1007/978-1-4614-3125-1_1

113. Schank, C. 2017. Titanium: The Medical Metal of Choice [Online]. Supra alloys. [Accessed 20 July 2019]. Available from: http://www.supraalloys.com/medical-titanium.php
114. Feller , L., et al., 2014. Osseointegration: biological events in relation to characteristics of the implant surface. *South African Dental Journal*. 69(3): p. 112-117.
115. Schüpbach, P., et al., 2005. The human bone-oxidized titanium implant interface: A light microscopic, scanning electron microscopic, back-scatter scanning electron microscopic, and energy-dispersive x-ray study of clinically retrieved dental implants. *Clinical Implant Dentistry and Related Research*. 7: pp.s36-s43.
116. Sidambe, A.T., 2014. Biocompatibility of advanced manufactured titanium implants—A review. *Materials*. 7(12): p. 8168-8188.
117. Das, K., et al., 2008. Surface modification of laser-processed porous titanium for load-bearing implants. *Scripta Materialia*. 59(8): p. 822-825.
118. Dehghan-Manshadi, A., et al., 2018. Porous Titanium Scaffolds Fabricated by Metal Injection Moulding for Biomedical Applications. *Materials*. 11(9): p. 1573.
119. Chen, Y., et al., 2017. Manufacturing of graded titanium scaffolds using a novel space holder technique. *Bioactive Materials*. 2(4): p. 248-252.
120. Yun, Y., et al., 2009. Revolutionizing biodegradable metals. *Materials Today*. 12(10): p. 22-32.
121. Jeong, J., et al., 2019. Bioactive calcium phosphate materials and applications in bone regeneration. *Biomaterials Research*. 23(1): p. 1-11.
122. Laasri, S., et al., 2016. Mechanical properties of calcium phosphate biomaterials. *Molecular Crystals and Liquid Crystals*. 628(1): p. 198-203.
123. Li, Z. and Kawashita, M., 2011. Current progress in inorganic artificial biomaterials. *Journal of Artificial Organs*. 14(3): p. 163-170.
124. Sakti, Y.M., et al., 2021. Diamond Concept as Principle for the Development of Spinal Cord Scaffold: A Literature Review. *Open Access Macedonian Journal of Medical Sciences*. 9(F): p. 754-769.
125. Shu, F., et al., 2016. Synthesis of amorphous coating by laser cladding multi-layer Co-based self-fluxed alloy powder. *Materials Letters*. 176: p. 306-309.
126. Eliaz, N. and N. Metoki, 2017. Calcium phosphate bioceramics: a review of their history, structure, properties, coating technologies and biomedical applications. *Materials*. 10(4): p. 334.
127. Khan, W.S., et al., 2012. An osteoconductive, osteoinductive, and osteogenic tissue-engineered product for trauma and orthopaedic surgery: how far are we? *Stem Cells International*.
128. Anastasiou, A., et al., 2017. β-pyrophosphate: A potential biomaterial for dental applications. *Materials Science and Engineering: C*. 75: p. 885-894.
129. Engstrand, J., Persson, C. and Engqvist, H., 2014. The effect of composition on mechanical properties of brushite cements. *Journal of the Mechanical Behavior of Biomedical Materials*. 29: p. 81-90.
130. Anastasiou, A., et al., 2016. Sintering of calcium phosphates with a femtosecond pulsed laser for hard tissue engineering. *Materials & Design*. 101: p. 346-354.
131. Grover, L.M., et al., 2013. The effect of amorphous pyrophosphate on calcium phosphate cement resorption and bone generation. *Biomaterials*. 34(28): p. 6631-6637.
132. Naga, S.M., et al., 2014. Biological Performance of Calcium Pyrophosphate-coated Porous Alumina Scaffolds. *International Journal of Applied Ceramic Technology*. 11(1): p. 1-11.
133. Lin, F.-H., et al., 1995. Mechanical properties and histological evaluation of sintered β-$Ca_2P_2O_7$ with $Na_4P_2O_7 \cdot 10H_2O$ addition. *Biomaterials*. 16(10): p. 793-802.

134. Davis, J., 2003. Handbook of materials for medical devices. ASM Handbook Series.
135. Zhou, H. and Lee, J., 2011. Nanoscale hydroxyapatite particles for bone tissue engineering. *Acta Biomaterialia*. 7(7): p. 2769-2781.
136. Khanal, S.P., et al., 2016. Improvement of the fracture toughness of hydroxyapatite (HAp) by incorporation of carboxyl functionalized single walled carbon nanotubes (CfSWCNTs) and nylon. *Materials Science and Engineering: C*. 60: p. 204-210.
137. Shuai, C., et al., 2013. Correlation between properties and microstructure of laser sintered porous β-tricalcium phosphate bone scaffolds. *Science and Technology of Advanced Materials*.
138. Moussa, H., et al., 2020. High strength brushite bioceramics obtained by selective regulation of crystal growth with chiral biomolecules. *Acta Biomaterialia*. 106: p. 351-359.
139. Koester, K.J., Ager, J. and Ritchie, R., 2008. The true toughness of human cortical bone measured with realistically short cracks. *Nature Materials*. 7(8): p. 672-677.
140. Sola, A., et al., 2011. Bioactive glass coatings: a review. *Surface Engineering*. 27(8): p. 560-572.
141. Pereira, M.M., Jones, J.R. and Hench, L.L. 2005. Bioactive glass and hybrid scaffolds prepared by sol–gel method for bone tissue engineering. *Advances in Applied Ceramics*. 104(1): p. 35-42.
142. Krishnan, V. and Lakshmi, T., 2013. Bioglass: A novel biocompatible innovation. *Journal of Advanced Pharmaceutical Technology & Research*. 4(2): p. 78.
143. Bloyer, D.R., et al., 1999. Fabrication and Characterization of A Bioactive Glass Coating on Titanium Implant Alloys. *Acta Materialia*. 47(15-16): p. 4221-4224.
144. Popescu , A.C., et al., 2009. Biocompatible and bioactive nanostructured glass coatings synthesized by pulsed laser deposition: *In vitro* biological tests. *Applied Surface Science*. p. 5486–5490.
145. Floroian , L., et al., 2008. Nanostructured bioglass thin films synthesized by pulsed laser deposition: CSLM, FTIR investigations and *in vitro* biotests. *Applied Surface Science*. 255(5): p. 3056–3062.
146. Rahaman, M.N., et al., 2011. Bioactive glass in tissue engineering. *Acta Biomaterialia*. 7(6): p. 2355-2373.
147. Liu, X., et al., 2013. Mechanical properties of bioactive glass (13-93) scaffolds fabricated by robotic deposition for structural bone repair. *Acta Biomaterialia*. 9(6): p. 7025-7034.
148. Avgoustakis, K., 2005. Polylactic-co-glycolic acid (PLGA). *Encyclopedia of Biomaterials and Biomedical Engineering*. 1(1): p. 1-11.
149. Basha, R.Y., TS, S.K. and Doble, M., 2015. Design of biocomposite materials for bone tissue regeneration. *Materials Science and Engineering: C*. 57: p. 452-463.
150. Porter, J.R., Ruckh, T.T. and Popat, K.C., 2009. Bone tissue engineering: a review in bone biomimetics and drug delivery strategies. *Biotechnology Progress*. 25(6): p. 1539-1560.
151. Gentile, P., et al., 2014. An overview of poly (lactic-co-glycolic) acid (PLGA)-based biomaterials for bone tissue engineering. *International Journal of Molecular Sciences*. 15(3): p. 3640-3659.
152. Kumbar S, Laurencin C, Deng M, editors, 2014. Natural and synthetic biomedical polymers [Online]. Newnes. [Accessed 01 August 2021]. Available from: https://books.google.co.uk/books?hl=en&lr=&id=QX58AQAAQBAJ&oi=fnd&pg=PP1&dq=Kumbar,+S.,+C.+Laurencin,+and+M.+Deng,+Natural+and+synthetic+biomedical+polymers.

153. Mikos, A.G., et al., 1993. Preparation of poly (glycolic acid) bonded fiber structures for cell attachment and transplantation. *Journal of Biomedical Materials Research*. 27(2): p. 183-189.
154. Mikos, A.G., et al., 1993. Laminated three-dimensional biodegradable foams for use in tissue engineering. *Biomaterials*. 14(5): p. 323-330.
155. Mooney, D.J., et al., 1996. Novel approach to fabricate porous sponges of poly (D, L-lactic-co-glycolic acid) without the use of organic solvents. *Biomaterials*. 17(14): p. 1417-1422.
156. Floroiana, L., et al., 2007. Synthesis and Characterization of Bioglass Thin Films. Digest *Journal of Nanomaterials and Biostructures*. 2.3: p. 285-291.
157. Turnbull, G., et al., 2018. 3D bioactive composite scaffolds for bone tissue engineering. *Bioactive Materials*. 3(3): p. 278-314.
158. Chu, C., et al., 2002. Fabrication and characterization of hydroxyapatite reinforced with 20 vol% Ti particles for use as hard tissue replacement. *Journal of Materials Science: Materials in Medicine*. 13(10): p. 985-992.
159. Chu, C., et al., 2006. Fabrication and characterization of titanium-matrix composite with 20 vol% hydroxyapatite for use as heavy load-bearing hard tissue replacement. *Journal of Materials Science: Materials in Medicine*. 17(3): p. 245-251.
160. Chu, C., et al., 2004. Mechanical and biological properties of hydroxyapatite reinforced with 40 vol.% titanium particles for use as hard tissue replacement. *Journal of Materials Science: Materials in Medicine*. 15(6): p. 665-670.
161. Olszta, M.J., Cheng, X., Jee, S.S., Kumar, R., Kim, Y.Y., Kaufman, M.J., Douglas, E.P. and Gower, L.B., 2007. Bone structure and formation: A new perspective. *Materials Science Engineering: R: Reports*. 58(3-5): p. 77-116.
162. Castro, N.J., O'brien, J. and Zhang, L.G., 2015. Integrating biologically inspired nanomaterials and table-top stereolithography for 3D printed biomimetic osteochondral scaffolds. *Nanoscale*. 7(33): p. 14010-14022.
163. Scaglione, S., et al., 2012. Order versus Disorder: in vivo bone formation within osteoconductive scaffolds. *Scientific Reports*. 2(1): p. 1-6.
164. Carrel, J.P., et al., 2016. A 3D printed TCP/HA structure as a new osteoconductive scaffold for vertical bone augmentation. *Clinical Oral Implants Research*. 27(1): p. 55-62.
165. Moussa, M., et al., 2015. Medium-term function of a 3D printed TCP/HA structure as a new osteoconductive scaffold for vertical bone augmentation: A simulation by BMP-2 activation. *Materials*. 8(5): p. 2174-2190.
166. Staffa, G., et al., 2012. Custom made bioceramic implants in complex and large cranial reconstruction: a two-year follow-up. *Journal of Cranio-Maxillofacial Surgery*. 40(3): p. e65-e70.
167. Karageorgiou, V. and Kaplan, D., 2005. Porosity of 3D biomaterial scaffolds and osteogenesis. *Biomaterials*. 26(27): p. 5474-5491.
168. Dabrowski, B., et al., 2010. Highly porous titanium scaffolds for orthopaedic applications. *Journal of Biomedical Materials Research Part B: Applied Biomaterials*. 95(1): p. 53-61.
169. Rubshtein, A., et al., 2017. Properties of biocomposites based on titanium scaffolds with a different porosity. *Bulletin of Materials Science*. 40(3): p. 453-457.
170. Nouri, A. , Hodgson, P. D. , Wen, C., 2010. Biomimetic Porous Titanium Scaffolds for Orthopedic and Dental Applications. In: Mukherjee, A. , editor. Biomimetics Learning from Nature [Online]. London: IntechOpen. [Accessed 05 September 2021]. Available from: https://www.intechopen.com/chapters/10040 doi: 10.5772/8787

171. Portal Núñez, S., Lozano, D. and Esbrit, P., 2012. Role of angiogenesis on bone formation. 27: p. 8.
172. Hankenson KD, Dishowitz M, Gray C, and Schenker M., 2011. Angiogenesis in bone regeneration. *Injury*. 42(6): p. 556-561.
173. Castano, O., et al., 2014. Angiogenesis in bone regeneration: tailored calcium release in hybrid fibrous scaffolds. *ACS Applied Materials & Interfaces*. 6(10): p. 7512-7522.
174. Zhai, W., et al., 2012. Silicate bioceramics induce angiogenesis during bone regeneration. *Acta Biomaterialia*. 8(1): p. 341-349.
175. Keramaris, N., et al., 2008. Fracture vascularity and bone healing: a systematic review of the role of VEGF. *Injury*. 39: p. S45-S57.
176. Costa-Pinto, A.R., Reis, R.L. and Neves, N.M., 2011. Scaffolds based bone tissue engineering: the role of chitosan. *Tissue Engineering Part B: Reviews*. 17(5): p. 331-347.
177. Williams, D.F., 2008. On the mechanisms of biocompatibility. *Biomaterials*. 29(20): p. 2941-2953.
178. Navarro, M., et al., 2008. Biomaterials in orthopaedics. *Journal of the Royal Society Interface*. 5(27): p. 1137-1158.
179. Mahyudin, F., Widhiyanto, L., Hermawan, H., 2016. Biomaterials in Orthopaedics [Online]. In: Mahyudin, F., Hermawan, H. editors. *Biomaterials and Medical Devices. Advanced Structured Materials*, vol 58, p. 161-181. Springer, Cham. [Accessed 25 September 2021]. Available from: https://doi.org/10.1007/978-3-319-14845-8_7
180. Henkel, J., et al., 2013. Bone regeneration based on tissue engineering conceptions—a 21st century perspective. *Bone Research*. 1(1): p. 216-248.
181. Byrne, D.P., et al., 2007. Simulation of tissue differentiation in a scaffold as a function of porosity, Young's modulus and dissolution rate: application of mechanobiological models in tissue engineering. *Biomaterials*. 28(36): p. 5544-5554.
182. Hutmacher, D.W., 2000. Scaffolds in tissue engineering bone and cartilage. *Biomaterials*. 21(24): p. 2529-2543.
183. Millis, D.L., 2014. Responses of musculoskeletal tissues to disuse and remobilization, in *Canine Rehabilitation and Physical Therapy*. Elsevier. p. 92-153.
184. Middleton, K.A., Ma, Y.H.V. and You, L., 2017 . Measuring bone cell response to fluid shear stress and hydrostatic/dynamic pressure. In: Zdero, R., editor. Experimental Methods in Orthopaedic Biomechanics [Online]. pp. 217-232. Academic Press. [Accessed 05 September 2021]. Available from: https://www.sciencedirect.com/science/article/pii/B9780128038024000147
185. Sivananthan, S., Goodman, S.B. and Burke, M., 2021. Failure mechanisms in joint replacement. In: Revell, P., editor. Joint Replacement Technology (Third Edition) [Online]. pp. 373-402. Woodhead Publishing. [Accessed 15 November 2021]. Available from: https://www.sciencedirect.com/science/article/pii/B9780128210826000170
186. Burke, M. and Goodman, S., 2008. Failure mechanisms in joint replacement. In: Revell, P., editor. Joint replacement technology [Online]. pp. 264-285. Woodhead Publishing. [Accessed 15 November 2021]. Available from: https://www.sciencedirect.com/science/article/pii/B9781845692452500123
187. Fuchs, R.K., Warden, S.J. and Turner, C.H., 2009. Bone anatomy, physiology and adaptation to mechanical loading. In: Planell, J.A., Best, S.M., Lacroix, D. and Merolli, A. editors. Bone repair biomaterials [Online]. pp. 25-68. Woodhead Publishing. [Accessed 03 December 2020]. Available from: https://www.sciencedirect.com/science/article/pii/B9781845693855500027

188. Lovald, S. and Kurtz, S.M., 2012. Applications of polyetheretherketone in trauma, arthroscopy, and cranial defect repair [Online]. In: Kurtz, S.M., editor. *PEEK biomaterials handbook*. William Andrew Publishing. p. 243-260. [Accessed 05 December 2020]. Available from: https://www.sciencedirect.com/science/article/pii/B9781437744637100156
189. Goharian, A., 2019. *Osseointegration of Orthopaedic Implants* [Online]. Academic Press. [Accessed 01 June 2020]. Available from: https://books.google.co.uk/books?hl=en&lr=&id=_UyNDwAAQBAJ&oi=fnd&pg=PP1&dq=Goharian,+A.,+
190. Shayesteh Moghaddam, N., et al., 2016. Metals for bone implants: Safety, design, and efficacy. *Biomanufacturing Reviews*. 1(1): p. 1-16.
191. Wintermantel, E., Mayer, J. and Goehring, T.N., 2001. Composites for Biomedical applications. *Encyclopedia of Materials: Science and Technology*. 1371: p. 1376.
192. Bouët, G., et al., 2015. *In vitro* three-dimensional bone tissue models: from cells to controlled and dynamic environment. *Tissue Engineering Part B: Reviews*. 21(1): p. 133-156.
193. Bodén, H., 2006. A clinical study of uncemented hip arthroplasty: Radiological findings of host-bone reaction to the stem. Karolinska Institutet (Sweden).
194. Abbasi, N., et al., 2020. Porous scaffolds for bone regeneration. *Journal of Science: Advanced Materials and Devices*. 5(1): p. 1-9.
195. Nam, J.H., et al., 2020. Validation of the optimal scaffold pore size of nasal implants using the 3-dimensional culture technique. *Archives of Plastic Surgery*. 47(4): p. 310.
196. Han, Y., et al., 2021. Effect of Pore Size on Cell Behavior Using Melt Electrowritten Scaffolds. *Frontiers in Bioengineering and Biotechnology*. 9: p. 495.
197. Torres, Y., J. Pavón, and J. Rodríguez, 2012. Processing and characterization of porous titanium for implants by using NaCl as space holder. *Journal of Materials Processing Technology*. 212(5): p. 1061-1069.
198. Elmadani, E., et al., 2012. Characterization of Rare-Earth Oxide Photoactivated Calcium Phosphate Minerals for Resurfacing Teeth. *Journal of the American Ceramic Society*. 95(9): p. 2716-2724.
199. Toshima, T., et al., 2014. Morphology control of brushite prepared by aqueous solution synthesis. *Journal of Asian Ceramic Societies*. 2(1): p. 52-56.
200. Alsubhe, E., et al., 2020. Analysis of the osteogenic and mechanical characteristics of iron (Fe2+/Fe3+)-doped β-calcium pyrophosphate. *Materials Science and Engineering: C*. 115: p. 111053.
201. Betke, A. and Kickelbick, G., 2014 Bottom-up, wet chemical technique for the continuous synthesis of inorganic nanoparticles. *Inorganics*. 2(1): p. 1-15.
202. Bhatt, A. and Parappagoudar, M.B., 2015. Modeling and analysis of mechanical properties in structural steel-DOE approach. *Archives of Foundry Engineering*. 15(4): p. 5-12.
203. Perry, L.A., Montgomery, D.C. and Fowler, J.W., 2007. A partition experimental design for a sequential process with a large number of variables. *Quality and Reliability Engineering International*. 23(5): p. 555-564.
204. Zyska, A., Konopka, Z., Łągiewka, M. and Nadolski, M., 2013. Optimization of squeeze parameters and modification of AlSi7Mg alloy. *Archives of Foundry Engineering*.
205. Mandal, A. and Roy, P., 2006. Modeling the compressive strength of molasses–cement sand system using design of experiments and back propagation neural network. *Journal of Materials Processing Technology*. 180(1-3): p. 167-173.

206. Fang, Z.Z., 2010. *Sintering of advanced materials* [Online]. Elsevier. [Accessed 12 May 2019]. Available from: https://books.google.co.uk/books?hl=en&lr=&id=NYpwAgAAQBAJ&oi=fnd&pg=PP1&dq=
207. Arifvianto, B. and Zhou, J., 2014. Fabrication of metallic biomedical scaffolds with the space holder method: A review. *Materials*. 7(5): p. 3588-3622.
208. Müller, U., et al., 2006. Do human osteoblasts grow into open-porous titanium. *Eur Cell Mater*. 11: p. 8-15.
209. Bosman, H.L. 2016. *Influence of powder particle size distribution on press-and-sinter titanium and Ti-6Al-4V preforms*. MSc. thesis, Stellenbosch University.
210. Scott, A., 2011. Basics of X-ray powder diffraction, in *Massachusetts-USA*, Disponível.
211. Stanjek, H. and Häusler, W.J.H.I., 2004. Basics of X-ray Diffraction. *Hyperfine Interactions*. 154(1): p. 107-119.
212. Anon, X-ray Diffraction [Online]. JoVE Science Education Database. Materials Engineering, Cambridge, MA, [Accessed 09 July 2020]. Available from: https://www.jove.com/v/10446/x-ray-diffraction
213. Raja, P.M.V. and Barron, A. R., X-ray Crystallography [Online]. Rice University. [Accessed 15 July 2021]. Available from: https://chem.libretexts.org/Bookshelves/Analytical_Chemistry/Physical_Methods_in_Chemistry_and_Nano_Science_(Barron)/07%3A_Molecular_and_Solid_State_Structure/7.03%3A_X-ray_Crystallography
214. Thornton, S.T. and A. Rex, 2012. Modern Physics for Scientists and Engineers, Cengage Learning.
215. Pednekar, P.P., et al., 2017. Mesoporous silica nanoparticles: a promising multifunctional drug delivery system [Online]. In: Ficai, A., Grumezescu, A.M. editors. *Nanostructures for Cancer Therapy*. Elsevier. p. 593-621. [Accessed 12 September 2022]. Available from: https://www.sciencedirect.com/science/article/pii/B9780323461443000234
216. Anon, Scanning Electron Microscopy [Online]. Nanoscience instruments: [Accessed 01 July 2019]. Available from: https://www.nanoscience.com/techniques/scanning-electron-microscopy/
217. Akhtar, K., et al., 2018. Scanning electron microscopy: principle and applications in nanomaterials characterization, in *Handbook of Materials Characterization*. Springer. p. 113-145.
218. Starborg, T., et al., 2019. Experimental steering of electron microscopy studies using prior X-ray computed tomography. *Ultramicroscopy*. 201: p. 58-67.
219. Pauwels, B. and Sasov, A., 2013. X-ray Nano-and Micro-tomography in an SEM. *Microscopy Today*. 21(2): p. 24-28.
220. Rennie, M.Y., et al., 2014. Scanning electron microscopy and micro-computed tomography imaging of the utero-and fetoplacental circulations, in *The Guide to Investigation of Mouse Pregnancy*, Elsevier. p. 637-648.
221. Axelsson, S. 2012. *Surface characterization of titanium powders with x-ray photoelectron spectroscopy*. MSc. thesis, Chalmers University of Technology.
222. Anon, Scanning Electron Microscope A To Z. Basic Knowledge For Using The SEM, JEOL. [Accessed 01 July 2019]. Available from: https://www.jeol.co.jp/en/applications/pdf/sm/sem_atoz_all.pdf
223. Abd Mutalib, M., et al., 2017. Scanning electron microscopy (SEM) and energy-dispersive X-ray (EDX) spectroscopy [Online]. In: Hilal, N., Ismail, A.F., Matsuura, T. and Oatley-Radcliffe, D. editors. *Membrane Characterization*. Elsevier. p. 161-179.

[Accessed 05 July 2019]. Available from: https://www.sciencedirect.com/science/article/pii/B9780444637765000097
224. Suryanarayana, C., and Norton, M.G., 1998. Crystal Structure Determination. II: Hexagonal Structures. In: *X-Ray Diffraction A Practical Approach* [Online]. (pp 125–152), Springer, Boston, MA. [Accessed 15 December 2020]. Available from: https://doi.org/10.1007/978-1-4899-0148-4_5
225. Thermofisher, X-Ray Photoelectron Spectroscopy. XPS surface analysis of materials ranging from metals to polymers [Online]. Thermofisher Scientific: [Accessed 23 July 2019]. Available from: https://www.thermofisher.com/uk/en/home/materials-science/xps-technology.html
226. Kolmakov, A., et al., 2011. Graphene oxide windows for in situ environmental cell photoelectron spectroscopy. *Nature Nanotechnology*. 6(10): p. 651-657.
227. PerkinElmer, 2008. STA 6000/8000 Simultaneous Thermal Analyzer [Online]. [Accessed 21 August 2019]. Available from: https://resources.perkinelmer.com/corporate/content/relatedmaterials/brochures/bro_sta-6000.pdf
228. Cassel, B., et al., Use of the STA 8000 Simultaneous Thermal Analyzer for Melt Analysis of Alloys. Berry College Department of Chemistry Mount Berry, GA USA. [Accessed 23 Febreuary 2020]. Available from: https://resources.perkinelmer.com/labsolutions/resources/docs/app_sta8000_analyzer_meltanalysis_alloys.pdf
229. Coats, A.W. and Redfern, J.P., 1963. Thermogravimetric analysis. A review. *Analyst*. 88(1053): p. 906-924.
230. National Research Council, 2003. Beyond the Molecular Frontier: Challenges for Chemistry and Chemical Engineering [Online]. Washington, DC: The National Academies Press. Available from: doi: 10.17226/10633.
231. Hitachi, Principle of differential thermal analysis (DTA). Hitachi High-Tech GLOBAL. [Accessed 15 August 2019]. Available from: https://www.hitachi-hightech.com/global/products/science/tech/ana/thermal/descriptions/dta.html
232. Yang, X., et al., 2017. Characterization of the absolute volume change of cement pastes in early-age hydration process based on helium pycnometry. *Construction and Building Materials*. 142: p. 490-498.
233. Webb, P.A., 2001. Volume and density determinations for particle technologists. *Micromeritics Instrument Corp*. 2(16): p. 01.
234. Cheppudira Thimmaiah, P., et al., 2018. A new approach to compute the porosity and surface roughness of porous coated capillary-assisted low pressure evaporators. *Scientific Reports*. 8(1): p. 1-11.
235. Torsæter, O. and Abtahi, M., 2003. *Experimental reservoir engineering laboratory workbook*. Norwegian University of Science and Technology. Available from: https://www.spec2000.net/downloads/LabManual.pdf
236. O'Sullivan, J.D., et al., 2018. X-ray micro-computed tomography (μCT): an emerging opportunity in parasite imaging. *Parasitology*. 145(7): p. 848-854.
237. Microphotonics, 2020. What is Micro-CT? An Introduction [Online]. Microphotonics Inc. [Accessed 01 Febreuary 2020]. Available from: https://www.microphotonics.com/what-is-micro-ct-an-introduction/
238. Rohrer, G., 2014. Microstructural Characterization of Hard Ceramics. *Comprehensive Hard Materials*. 2: p. 265-284.
239. Maire, E. and Withers, P.J., 2014. Quantitative X-ray tomography. *International Materials Reviews*. 59(1): p. 1-43.

240. Kerckhofs, G., et al., 2006. Standardisation and validation of micro-CT for the morphological characterisation of porous structures. in Proc. 9th Eur. Conf. Non-Destructive Testing (ECNDT). *Berlin, Germany*.
241. Glistau, E., Schenk, M. and Machado, N.I.C., 2017. Full-factorial design of experiments in logistics systems, *in International Multidisciplinary Scientific Conference.* University of Miskolc, Hungary.
242. He, S., et al., 2012. Response surface methodology optimization of fermentation conditions for rapid and efficient accumulation of macrolactin A by marine Bacillus amyloliquefaciens ESB-2. *Molecules*. 18(1): p. 408-417.
243. Öhman, C., et al., 2011. Compressive behaviour of child and adult cortical bone. *Bone*. 49(4): p. 769-776.
244. Bayraktar, H.H., et al., 2004. Comparison of the elastic and yield properties of human femoral trabecular and cortical bone tissue. *Journal of Biomechanics*. 37(1): p. 27-35.
245. Kotha, S. and N. Guzelsu, 2003. Tensile damage and its effects on cortical bone. *Journal of Biomechanics*. 36(11): p. 1683-1689.
246. Bhosale, R.S. and Zambare, B.R., 2013. Sex determination from femur using length of femur in Maharashtra. *Journal of Dental and Medical Sciences*. 3(4): p. 01-03.
247. Mahmoudi, M., 2017. Femur Bone [Online]. GrabCAD Community. [Accessed 19 April 2019]. Available from: https://grabcad.com/library/femur-bone-2
248. Sheikh, M.S.A., Ganorkar, A.P. and Dehankar, R.N., 2016. Finite Element Analysis of Femoral Intramedullary Nailing. *Journal for Research*. p. 2395-7549.
249. Yousif, A.E. and Aziz, M.Y., 2012. Biomechanical Analysis of the human femur bone during normal walking and standing up. *IOSR Journal of Engineering*. 2(8): p. 13-19.
250. Qasim, M., et al., 2016. Patient-specific finite element estimated femur strength as a predictor of the risk of hip fracture: the effect of methodological determinants. *Osteoporosis International*. 27(9): p. 2815-2822.
251. Lucero, C.M., et al., 2013. The cancer-related transcription factor Runx2 modulates cell proliferation in human osteosarcoma cell lines. *Journal of Cellular Physiology*. 228(4): p. 714-723.
252. Muller, M., 2006. *Introduction to confocal fluorescence microscopy* (Second Edition) [Online]. Vol. 69. SPIE press. [Accessed 19 August 2019]. Available from: https://books.google.co.uk/books?hl=en&lr=&id=t7N4G4x9zGcC&oi=fnd&pg=PR11&dq=
253. Lagali, N. editor, 2013. *Confocal Laser Microscopy: Principles and Applications in Medicine, Biology, and the Food Sciences*. BoD–Books on Demand. [Accessed 19 August 2019]. Available from: https://books.google.co.uk/books?hl=en&lr=&id=buacDwAAQBAJ&oi=fnd&pg=PR9&dq=
254. Soliman, D.M. 2017. *Augmented microscopy: Development and application of high-resolution optoacoustic and multimodal imaging techniques for label-free biological observation.* Ph.D. thesis, Technische Universität München.
255. Li, Z., et al., 2018. Heat treatment effect on the mechanical properties, roughness and bone ingrowth capacity of 3D printing porous titanium alloy. *RSC Advances*. 8(22): p. 12471-12483.
256. Mekmene, O., et al., 2009. Effects of pH and Ca/P molar ratio on the quantity and crystalline structure of calcium phosphates obtained from aqueous solutions. *Dairy Science & Technology*. 89(3): p. 301-316.
257. Arifuzzaman, S.M. and Rohani, S., 2004. Experimental study of brushite precipitation. *Journal of Crystal Growth*. 267(3-4): p. 624-634.

258. Cheng, P.-T. and Pritzker, K.P., 1983. Solution Ca/P ratio affects calcium phosphate crystal phases. *Calcified Tissue International*. 35(1): p. 596-601.
259. Lee, D. and Kumta, P.N., 2010. Chemical synthesis and stabilization of magnesium substituted brushite. *Materials Science and Engineering: C*. 30(7): p. 934-943.
260. McIntosh, A.O. and Jablonski, W.L., 1956. X-ray diffraction powder patterns of calcium phosphates. *Analytical Chemistry*. 28(9): p. 1424-1427.
261. Gozalian, A., et al., 2011. Synthesis and thermal behavior of Mg-doped calcium phosphate nanopowders via the sol-gel method. *Scientia Iranica*. 18(6): p. 1614-1622.
262. Dosen, A. and Giese, R.F., 2011. Thermal decomposition of brushite, $CaHPO_4$ $2H_2O$ to monetite $CaHPO_4$ and the formation of an amorphous phase. *American Mineralogist*. 96(2-3): p. 368-373.
263. Blake, A.J., Cole, J.M., Evans, J.S., Main, P., Parsons, S. and Watkin, D.J., 2009. *Crystal structure analysis: principles and practice* (Second Edition). Clegg, W. editor. Vol. 13. OUP Oxford. [Accessed 26 October 2021]. Available from: https://books.google.co.uk/books?hl=en&lr=&id=d_1QEAAAQBAJ&oi=fnd&pg=PR9&dq=Blake,+A.J.,+et+al.,+
264. Suryanarayana, C., and Norton, M.G., 1998. Crystal Structure Determination. II: Hexagonal Structures. In: *X-Ray Diffraction A Practical Approach* [Online]. (pp 125–152), Springer, Boston, MA. [Accessed 15 December 2020]. Available from: https://doi.org/10.1007/978-1-4899-0148-4_5
265. Ning, C. and Zhou, Y., 2008. Correlations between the in vitro and *in vivo* bioactivity of the Ti/HA composites fabricated by a powder metallurgy method. *Acta Biomaterialia*. 4(6): p. 1944-1952.
266. Oh, J.-M., et al., 2011. Oxygen effects on the mechanical properties and lattice strain of Ti and Ti-6Al-4V. *Metals and Materials International*. 17(5): p. 733-736.
267. Ohring, M., 1995. *Engineering materials science*. Academic Press. [Accessed 25 January 2018]. Available from: https://books.google.co.uk/books?hl=en&lr=&id=LcvgiCbOo38C&oi=fnd&pg=PP1&dq=
268. Kwasniak, P., et al., 2014, Influence of oxygen content on the mechanical properties of hexagonal Ti—First principles calculations. *Materials Science and Engineering: A*. 590: p. 74-79.
269. Ji, X., et al., 2018. Effect of oxygen addition on microstructures and mechanical properties of Ti-7.5 Mo alloy. *Journal of Alloys and Compounds*. 737: p. 221-229.
270. Dechamps, M., et al., 1977. Influence of the distribution of the interstitial oxygen atoms on the lattice parameters in dilute HCP titanium-oxygen solid solutions (90–4000 ppm at). *Scripta Metallurgica*. 11(11): p. 941-945.
271. Murray, J.L. and Wriedt, H.A., 1987. The O− Ti (oxygen-titanium) system. *Journal of Phase Equilibria*. 8(2): p. 148-165.
272. Mondal, D., et al., 2011. Comparative study of microstructures and material properties in the vacuum and spark plasma sintered Ti-calcium phosphate composites. *Materials Transactions*. 52(7): p. 1436-1442.
273. Ergun, C., 2008. Effect of Ti ion substitution on the structure of hydroxylapatite. *Journal of the European Ceramic Society*. 28(11): p. 2137-2149.
274. Niespodziana, K., 2019. Synthesis and properties of porous Ti-20 wt.% HA nanocomposites. *Journal of Materials Engineering and Performance*. 28(4): p. 2245-2255.
275. Salman, S., et al., 2009. Sintering effect on mechanical properties of composites of natural hydroxyapatites and titanium. *Ceramics International*. 35(7): p. 2965-2971.

276. Arifin, A., et al., 2014. Material processing of hydroxyapatite and titanium alloy (HA/Ti) composite as implant materials using powder metallurgy: a review. *Materials & Design*. 55: p. 165-175.
277. Omran, A., et al., 2015. Fabrication and evaluation of porous Ti–HA bio-nanomaterial by leaching process. *Arabian Journal of Chemistry*. 8(3): p. 372-379.
278. Ribeiro, A., et al., 2013. Dense and porous titanium substrates with a biomimetic calcium phosphate coating. *Applied Surface Science*. 265: p. 250-256.
279. Balbinotti, P., et al., 2011. Microstructure development on sintered Ti/HA biocomposites produced by powder metallurgy. *Materials Research*. 14(3): p. 384-393.
280. Wagner, C., et al., 2003. NIST standard reference database 20, Version 3.4 (Web version). National Institute of Standards and Technology, *Gaithersburg*, MD.
281. Ye, H., Liu, X.Y. and Hong, H., 2013. Fabrication of titanium/fluorapatite composites and in vitro behavior in simulated body fluid. *Journal of Materials Science & Technology*. 29(6): p. 523-532.
282. Shvab, R., Hryha, E. and Nyborg, L., 2017. Surface chemistry of the titanium powder studied by XPS using internal standard reference. Powder Metallurgy. 60(1): p. 42-48.
283. Riaz, A., et al., 2021. Tunable Pseudo-Piezoelectric Effect in Doped Calcium Titanate for Bone Tissue Engineering. *Materials*. 14(6): p. 1495.
284. Webster, T.J., et al., 2003. Increased osteoblast adhesion on titanium-coated hydroxylapatite that forms $CaTiO_3$. *Journal of Biomedical Materials Research Part A*: An Official Journal of The Society for Biomaterials, The Japanese Society for Biomaterials, and The Australian Society for Biomaterials and the Korean Society for Biomaterials. 67(3): p. 975-980.
285. Hamada, K., et al., 2002. Hydrothermal modification of titanium surface in calcium solutions. *Biomaterials*. 23(10): p. 2265-2272.
286. Ohtsu, N., et al., 2007. Calcium phosphates formation on $CaTiO_3$ coated titanium. *Journal of Materials Science: Materials in Medicine*. 18(6): p. 1009-1016.
287. Cheng, H., et al., 2020. Calcium titanate micro-sheets scaffold for improved cell viability and osteogenesis. *Chemical Engineering Journal*. 389: p. 124400.
288. Wang, Z.-l., et al., 2017. Enhanced biocompatibility and osseointegration of calcium titanate coating on titanium screws in rabbit femur. *Journal of Huazhong University of Science and Technology [Medical Sciences]*. 37(3): p. 362-370.
289. Yadi, M., et al., 2020. $CaTiO_3$/α-TCP coatings on CP-Ti prepared via electrospinning and pulsed laser treatment for in-vitro bone tissue engineering. *Surface and Coatings Technology*. 401: p. 126256.
290. Ho, S.T. and D.W. Hutmacher, 2006. A comparison of micro CT with other techniques used in the characterization of scaffolds. *Biomaterials*. 27(8): p. 1362-1376.
291. Lin, A.S., et al., 2003. Microarchitectural and mechanical characterization of oriented porous polymer scaffolds. *Biomaterials*. 24(3): p. 481-489.
292. Semel, F.J. and Lados, D.A., 2006. Porosity analysis of PM materials by helium pycnometry. *Powder Metallurgy*. 49(2): p. 173-182.
293. Qian, M., Schaffer, G. and Bettles, C., 2010. Sintering of titanium and its alloys [Online]. In: Fang Z.Z., editor. *Sintering of Advanced Materials*., Woodhead Publishing. p. 324-355. [Accessed 20 December 2018]. Available from: https://www.sciencedirect.com/science/article/pii/B9781845695620500133
294. Chang, C., 1988. Measuring density and porosity of grain kernels using a gas pycnometer. *Cereal Chem*. 65(1): p. 13-15.
295. Ikada, Y., 2006. Challenges in tissue engineering. *Journal of the Royal Society Interface*. 3(10): p. 589-601.

296. Liu, X. and Ma, P.X., 2004. Polymeric scaffolds for bone tissue engineering. *Annals of Biomedical Engineering*. 32(3): p. 477-486.
297. Tuan, H.S. and Hutmacher, D.W. 2007. The biomedical applications of computed tomography [Online]. In: Leondes, C.T. editor. *Biomechanical Systems Technology: Volume 1: Computational Methods*. World Scientific. p. 193-223. [Accessed 10 November 2019]. Available from: https://www.worldscientific.com/doi/abs/10.1142/9789812770042_0006
298. Murphy, C.M., Haugh, M.G. and O'brien, F.J., 2010. The effect of mean pore size on cell attachment, proliferation and migration in collagen–glycosaminoglycan scaffolds for bone tissue engineering. *Biomaterials*. 31(3): p. 461-466.
299. Kuboki, Y., Jin, Q. and Takita, H., 2001. Geometry of carriers controlling phenotypic expression in BMP-induced osteogenesis and chondrogenesis. *The Journal of Bone & Joint Surgery*. 83(1): p. S105-S115.
300. Roosa, S.M.M., et al., 2010. The pore size of polycaprolactone scaffolds has limited influence on bone regeneration in an *in vivo* model. *Journal of Biomedical Materials Research Part A:* An Official Journal of The Society for Biomaterials, The Japanese Society for Biomaterials, and The Australian Society for Biomaterials and the Korean Society for Biomaterials. 92(1): p. 359-368.
301. Tsuruga, E., et al., 1997. Pore size of porous hydroxyapatite as the cell-substratum controls BMP-induced osteogenesis. *The Journal of Biochemistry*. 121(2): p. 317-324.
302. Chen, Y., et al., 2017. Mechanical properties and biocompatibility of porous titanium scaffolds for bone tissue engineering. *Journal of the Mechanical Behavior of Biomedical Materials*. 75: p. 169-174.
303. Ajaxon, I., et al., 2017. Elastic properties and strain-to-crack-initiation of calcium phosphate bone cements: Revelations of a high-resolution measurement technique. *Journal of the Mechanical Behavior of Biomedical Materials*. 74: p. 428-437.
304. Prochor, P., Piszczatowski, S. and Sajewicz, E., 2016. Biomechanical evaluation of a novel Limb Prosthesis Osseointegrated Fixation System designed to combine the advantages of interference-fit and threaded solutions. *Acta of Bioengineering and Biomechanics*. 18(4): p. 21-31.
305. Havaldar, R., Pilli, S.C. and Putti, B.B., 2014. Insights into the effects of tensile and compressive loadings on human femur bone. *Advanced Biomedical Research*.
306. Johnson, A.J.W. and Herschler, B.A., 2011. A review of the mechanical behavior of CaP and CaP/polymer composites for applications in bone replacement and repair. *Acta Biomaterialia*. 7(1): p. 16-30.
307. Mohamed, S. and Shamaz, B.H., 2015. Bone tissue engineering and bony scaffolds. *International Journal of Dentistry and Oral Health*. 1: p. 15-20.
308. Wang, H., Fang, Z.Z. and Sun, P., 2010. A critical review of mechanical properties of powder metallurgy titanium. *International Journal of Powder Metallurgy*. 46(5): p. 45-57.
309. Heaney, D.F. and German, R.M., 2004 . PM Lightweight and Porous Materials: Advances in the Sintering of Titanium Powders. In European Congress and Exhibition on Powder Metallurgy. *European PM Conference Proceedings*. Vol. 4, p. 1. The European Powder Metallurgy Association.
310. Luo, S., et al., 2020. High oxygen-content titanium and titanium alloys made from powder. *Journal of Alloys and Compounds*. 836: p. 155526.
311. Gardner, H., et al., 2021. Quantifying the effect of oxygen on micro-mechanical properties of a near-alpha titanium alloy. *Journal of Materials Research*. 36(12): p. 2529-2544.

312. Wu, H. 2013. *Oxygen diffusion through Titanium and other hcp metals.* Ph.D. thesis, University of Illinois at Urbana-Champaign.
313. Mi, Z.R., et al., 2007. Problem of stress shielding and improvement to the hip Implat designs: a review. *Journal of Medical Sciences*. 7(3): p. 460-467.
314. Behrens, B.-A., et al., 2008. Numerical investigations of stress shielding in total hip prostheses. Proceedings of the Institution of Mechanical Engineers, Part H: *Journal of Engineering in Medicine*. 222(5): p. 593-600.
315. Liu, D.M., 1997. Influence of Porosity and Pore Size on the Compressive Strength of Porous Hydroxyapatite Ceramic. *Ceramics International*. 23(2): p. 135-139.
316. Roohani-Esfahani, S.I., P. Newman , and H. Zreiqat, 2016. Design and Fabrication of 3D printed Scaffolds with a Mechanical Strength Comparable to Cortical Bone to Repair Large Bone Defects. *Scientific Reports*. 6(1), pp.1-8
317. Pioletti, D.P., 2010. Biomechanics in bone tissue engineering. *Computer Methods in Biomechanics and Biomedical Engineering*. 13(6): p. 837-846.
318. Zhu, G., et al., 2021. Bone physiological microenvironment and healing mechanism: Basis for future bone-tissue engineering scaffolds. *Bioactive Materials*. 6(11): p. 4110-4140.
319. Breuls, R.G., Jiya, T.U. and Smit, T.H., 2008. Scaffold stiffness influences cell behavior: opportunities for skeletal tissue engineering. *The Open Orthopaedics Journal*. 2: p. 103–109.
320. Kamiloglu, S., et al., 2020. Guidelines for cell viability assays. *Food Frontiers*. 1(3): p. 332-349.
321. Riss, T.L., Moravec, R.A., Niles, A.L., Duellman, S., Benink, H.A., Worzella, T.J. and Minor, L., 2016. *Cell viability assays. Assay Guidance Manual*. Eli Lilly & Company and the National Center for Advancing. [Accessed 17 September 2021]. Available from: https://www.ncbi.nlm.nih.gov/books/NBK144065/?report=reader#!po=96.6667
322. Kumar, P., Nagarajan, A. and Uchil, P.D., 2018. Analysis of cell viability by the alamarblue assay. *Cold Spring Harbor Protocols*. (6): p. pdb. prot095489.
323. Sumantran, V.N., 2011. Cellular chemosensitivity assays: an overview. *Cancer Cell Culture*. p. 219-236.
324. Ahmed, S.A., Gogal Jr, R.M. and Walsh, J.E., 1994. A new rapid and simple non-radioactive assay to monitor and determine the proliferation of lymphocytes: an alternative to [3H] thymidine incorporation assay. *Journal of Immunological Methods*. 170(2): p. 211-224.
325. Tang, L., et al., 2018. LAPONITE® nanorods regulating degradability, acidic-alkaline microenvironment, apatite mineralization and MC3T3-E1 cells responses to poly (butylene succinate) based bio-nanocomposite scaffolds. *RSC Advances*. 8(20): p. 10794-10805.
326. Bodhak, S., et al., 2012. Investigation of in vitro bone cell adhesion and proliferation on Ti using direct current stimulation. *Materials Science and Engineering: C*. 32(8): p. 2163-2168.
327. Lindwall, G., Wang, P., Kattner, U.R. and Campbell, C.E., 2018. The effect of oxygen on phase equilibria in the Ti-V system: impacts on the AM processing of Ti alloys. *The Journal of The Minerals*. 70(9): p. 1692-1705.
328. Rodríguez, A.P., et al., 2018. *In Vitro* Efficacy of $CaCO_3$ Content in $CaTiO_3$–$CaCO_3$ Composites for Bone Growth. *Journal of Hard Tissue Biology*. 27(3): p. 250-256.
329. Ohtsu, N., et al., 2007. $CaTiO_3$ coating on titanium for biomaterial application—optimum thickness and tissue response. *Journal of Biomedical Materials Research Part A*: An Official Journal of The Society for Biomaterials, The Japanese Society for

Biomaterials, and The Australian Society for Biomaterials and the Korean Society for Biomaterials. 82(2): p. 304-315.
330. Motola, M., et al., 2020. Thin TiO_2 coatings by ALD enhance the cell growth on TiO_2 nanotubular and flat substrates. *ACS Applied Bio Materials*. 3(9): p. 6447-6456.
331. Atiyah, A.G., Al-Falahi, N.H.R. and Zarraq, G.A., 2021. Synthesis and Characterization of Porous β-Calcium Pyrophosphate Bone Scaffold Derived from Avian Eggshell. *Pakistan Journal of Zoology*. p. 1-4.
332. Anastasiou, A., et al., 2019. Drug loading capacity of microporous β-pyrophosphate crystals. *Materials & Design*. 168: p. 107661.
333. Krieghoff, J., et al., 2019. Increased pore size of scaffolds improves coating efficiency with sulfated hyaluronan and mineralization capacity of osteoblasts. *Biomaterials Research*. 23(1): p. 1-13.
334. Bartoš, M., Suchý, T. and Foltán, R., 2018. Note on the use of different approaches to determine the pore sizes of tissue engineering scaffolds: what do we measure? *Biomedical Engineering Online*. 17(1): p. 1-15.
335. Nava, M.M., et al., 2016. The effect of scaffold pore size in cartilage tissue engineering. *Journal of Applied Biomaterials & Functional Materials*. 14(3): p. e223-e229.
336. Mercado-Pagán, Á.E., et al., 2015. Vascularization in bone tissue engineering constructs. *Annals of Biomedical Engineering*. 43(3): p. 718-729.
337. Santos, M.I. and Reis, R.L., 2010. Vascularization in bone tissue engineering: physiology, current strategies, major hurdles and future challenges. *Macromolecular Bioscience*. 10(1): p. 12-27.
338. Chiu, Y.-C., et al., 2011. The role of pore size on vascularization and tissue remodeling in PEG hydrogels. *Biomaterials*. 32(26): p. 6045-6051.
339. Feng, B., Jinkang, Z., Zhen, W., Jianxi, L., Jiang, C., Jian, L., Guolin, M. and Xin, D., 2011. The effect of pore size on tissue ingrowth and neovascularization in porous bioceramics of controlled architecture *in vivo*. *Biomedical Materials*. 6(1): p. 015007.
340. Moorhouse, B., 2013. *Controlling the interstitial element concentration in Ti-6Al-4V using calciothermic reduction*. Ph.D. thesis, Imperial College London.
341. Atesok, K., et al., 2016. Multilayer scaffolds in orthopaedic tissue engineering. *Knee Surg Sports Traumatol Arthrosc*. 24(7): p. 2365-2373.
342. O'Shea, T.M. and Miao, X., 2008. Bilayered scaffolds for osteochondral tissue engineering. *Tissue Engineering Part B: Reviews*. 14(4): p. 447-464.
343. Rodrigues, M.T., et al., 2012. Bilayered constructs aimed at osteochondral strategies: the influence of medium supplements in the osteogenic and chondrogenic differentiation of amniotic fluid-derived stem cells. *Acta Biomaterialia*. 8(7): p. 2795-2806.
344. Shimomura, K., et al., 2014. Osteochondral tissue engineering with biphasic scaffold: current strategies and techniques. *Tissue Eng Part B Rev*. 20(5): p. 468-76.
345. Iqbal, N. 2020. *Freeze dried chitosan scaffolds with calcium phosphate minerals and cerium oxide nanoparticles for enhanced osteoconductive and antibacterial properties*. Ph.D. thesis, University of Leeds.